

Development of thin film inorganic membranes for oxygen separation

Hyo Jeong Moon

Forschungszentrum Jülich GmbH
Institute of Energy and Climate Research (IEK)
Materials Synthesis and Processing (IEK-1)

Development of thin film inorganic membranes for oxygen separation

Hyo Jeong Moon

Schriften des Forschungszentrums Jülich
Reihe Energie & Umwelt / Energy & Environment

Band / Volume 136

ISSN 1866-1793

ISBN 978-3-89336-781-8

Bibliographic information published by the Deutsche Nationalbibliothek.
The Deutsche Nationalbibliothek lists this publication in the Deutsche
Nationalbibliografie; detailed bibliographic data are available in the
Internet at <http://dnb.d-nb.de>.

Publisher and
Distributor: Forschungszentrum Jülich GmbH
Zentralbibliothek
52425 Jülich
Phone +49 (0) 24 61 61-53 68 · Fax +49 (0) 24 61 61-61 03
e-mail: zb-publikation@fz-juelich.de
Internet: <http://www.fz-juelich.de/zb>

Cover Design: Grafische Medien, Forschungszentrum Jülich GmbH

Printer: Grafische Medien, Forschungszentrum Jülich GmbH

Copyright: Forschungszentrum Jülich 2012

Schriften des Forschungszentrums Jülich
Reihe Energie & Umwelt / Energy & Environment Band / Volume 136

D 294 (Diss., Bochum, Univ., 2012)

ISSN 1866-1793

ISBN 978-3-89336-781-8

The complete volume is freely available on the Internet on the Jülicher Open Access Server (JUWEL) at
<http://www.fz-juelich.de/zb/juwel>

Neither this book nor any part of it may be reproduced or transmitted in any form or by any
means, electronic or mechanical, including photocopying, microfilming, and recording, or by any
information storage and retrieval system, without permission in writing from the publisher.

Abstract

Membrane-based gas separation systems are noteworthy among technological options for carbon capture and storage (CCS), which is an important strategy to reduce CO₂ emitted from point sources, e.g. mainly fossil power plants. In Oxyfuel-Combustion and Pre-Combustion of CCS power plant concepts oxygen separation from air is required. To meet this requirement oxygen transport membranes (OTM) consisting of gastight mixed ionic electronic conductors (MIEC) are proposed, which are associated with significantly lower efficiency losses compared with conventional air separation technologies.

For cost effective application a maximum oxygen flux has to be achieved to reduce the membrane area. This can be met by reduction of membrane thickness. Therefore, the reduction of the membrane thickness to the micrometer range or even below is aimed in the present thesis.

Ce_{0.8}Gd_{0.2}O_{2-δ} (CGO) with fluorite crystal structure and La_{0.58}Sr_{0.4}Co_{0.2}Fe_{0.8}O_{3-δ} (LSCF) with perovskite crystal structure were developed as thin film membrane. CGO is expected to be more stable than other potential MIEC membranes in reducing atmospheres and to achieve sufficient oxygen permeation, e.g. in syngas production or petrol chemistry. LSCF is expected to be highly permeable with an acceptable chemical stability in Oxyfuel-combustion.

Various porous ceramic substrates were prepared by vacuum-slip-casting and warm-pressing, and then characterized for porosity, gas-permeability and surface roughness. Subsequently, two approaches to fabrication of thin film membranes were investigated, which are wet-chemical deposition (WCD) and physical vapor deposition (PVD).

For WCD, nano-dispersions and colloidal sols were prepared for membrane top-layer and/or interlayer. When CGO nano-dispersion (NDCGO) was spin-coated as thin film membrane, the gastightness of sintered membranes was increased with decrease in spinning time and increase in concentration of NDCGO. With decrease in cooling rate for sintering process and high molecular weight binder for higher concentration of NDCGO, crack-free layers were achieved. The leak rates of sintered and reduced membranes reached the range of 10⁻⁴ and 10⁻³ mbar·l·sec⁻¹·cm⁻², respectively.

For PVD, CGO membranes were deposited by reactive magnetron sputtering. According to the substrate properties and applied bias power, different deposition behavior was observed. Particularly for 8YSZ (8 mol% Y₂O₃ stabilized ZrO₂) substrate, four-zone-model of membrane was derived related to substrate strength and bias power. Without bias assist only porous films were deposited. Applying bias power enabled compact membrane but caused delamination at the same time. Adopting higher presintering temperature of substrate improved substrate strength and thus realized delamination-free compact membranes. LSCF membranes were deposited by magnetron sputtering without bias assist. LSCF membranes were porous on 8YSZ substrates, but gastight on CGO interlayers. Concentration of CGO nano-dispersion and presintering temperature of CGO interlayers rarely influenced the gastightness of deposited LSCF membrane. The leak rates of CGO and LSCF membranes reached the range of 10⁻⁴ and 10⁻³ mbar·l·sec⁻¹·cm⁻², respectively.

Kurzfassung

Membran-basierte Gastrennanlagen sind viel versprechende Kandidaten unter den technologischen Optionen für Carbon Capture and Storage (CCS), das eine wichtige Strategie zur Verringerung der CO₂-Emissionen aus Punktquellen, z.B. fossile Kraftwerke, ist. Für die CCS-Konzepte Oxyfuel sowie Pre-combustion ist reiner Sauerstoff erforderlich, der aus Luft abgetrennt werden muss. Hierzu können Sauerstoff-Transport-Membranen (OTM) aus einem gasdichten gemischt ionisch elektronisch leitenden Material (MIEC) eingesetzt werden, die mit deutlich geringeren Effizienzverlusten im Vergleich zur herkömmlichen Luftzerlegung verbunden sind.

Für eine kosteneffektive Anwendung muss ein maximaler Sauerstoff-Fluss erreicht werden, um die Membranfläche zu reduzieren. Dies kann durch Verringerung der Membrandicke erfolgen. Daher zielt die vorliegende Arbeit auf die Reduzierung der Membrandicke bis in den Mikrometerbereich oder sogar darunter.

Ce_{0,8}Gd_{0,2}O_{2-δ} (CGO) mit fluoritischer Kristallstruktur und La_{0,58}Sr_{0,4}Co_{0,2}Fe_{0,8}O_{3-δ} (LSCF) mit perowskitischer Kristallstruktur wurden als Dünnschichtmembran entwickelt. In reduzierenden Atmosphären, z.B. in der Synthesegas-Produktion oder in der Petrochemie, wird erwartet, dass CGO stabiler als andere potenzielle MIEC Membranen ist und eine ausreichende Sauerstoff-Permeation erreicht. LSCF dagegen ist hochpermeabel mit einer akzeptablen chemischen Stabilität für den Einsatz im Oxyfuel-Konzept.

Verschiedene poröse keramische Substrate wurden durch Vakuum-Schickerguss und Warm-Pressen hergestellt und dann auf Porosität, Gasdurchlässigkeit und Oberflächenrauheit untersucht. Anschließend wurden zwei unterschiedliche Verfahren zur Herstellung von Dünnschichtmembranen untersucht, die nass-chemische Abscheidung (WCD) und die physikalische Gasphasenabscheidung (PVD).

Für WCD, wurden Nano-Dispersionen und kolloidale Sole für die Applikation der Top- und/oder Zwischenschicht des Membranverbundes hergestellt. Bei der Präparation von CGO Dünnschichtmembranen mittels Schleuderbeschichtung (spin coating), wurde die Gasdichtigkeit der gesinterten Membranen mit Abnahme der Rotationszeit und mit Erhöhung CGO-Konzentration in der Nanodispersion erhöht. Durch Reduzierung der Abkühlrate nach dem Sinterprozess und die Nutzung langkettiger Binder bei hoher CGO-Konzentration wurden rissfreie Schichten erreicht. Für die gesinterten und nachträglich reduzierten Membranen konnten He-Leckraten im Bereich von 10⁻⁴ bis 10⁻³ mbar·l·sec⁻¹·cm⁻² erzielt werden.

Als Verfahren für die physikalische Gasphasenabscheidung von CGO wurde reaktives Magnetron Sputtern ausgewählt. Je nach Substrateigenschaften und angelegter Bias-Spannung wurde unterschiedliches Beschichtungsverhalten beobachtet. Für ein poröses 8YSZ (8 mol% Y₂O₃ stabilized ZrO₂)-Substrat wurde ein Vier-Zonen-Modell abgeleitet abhängig von Substratfestigkeit und Bias-Spannung. Ohne Bias wurden nur poröse Schichten abgeschieden. Das Anlegen einer Bias-Spannung ermöglichte die Herstellung kompakter Membranen, verursachte aber gleichzeitig Delamination. Die Verwendung höherer Vorsintertemperaturen

des Substrats verbesserte die Substratfestigkeit, so dass kompakte Membranen ohne Delamination realisiert werden konnten. LSCF-Membranen wurden durch Magnetron Sputtern ohne Bias-Spannung aufgebracht. Auf 8YSZ-Substraten wurden die Schichten porös, aber durch die Verwendung von CGO-Zwischenschichten konnten gasdichte Membranen erreicht werden. Die Konzentration der CGO-Nanodispersion sowie die Vorsintertemperatur der CGO-Zwischenschichten haben die Gasdichtheit der LSCF-Membran kaum beeinflusst. Die He-Leckraten von CGO- und LSCF-Membranen lagen jeweils im Bereich von 10^{-4} bis 10^{-3} mbar·l·sec⁻¹·cm⁻².

Table of Contents

List of figures	III
List of tables	IX
List of abbreviations	X
List of symbols	XII
1 Introduction	1
1.1 CO ₂ capture in fossil power plant.....	1
1.2 Gas separation membranes for CCS.....	2
1.3 Objective of this work	3
2 Fundamentals and background.....	4
2.1 Mixed ionic-electronic conducting membranes for O ₂ /N ₂ separation	4
2.1.1 Fluorite-structured CGO (Ce _{0.8} Gd _{0.2} O _{2-δ}) membrane	6
2.1.2 Perovskite-structured LSCF (La _{0.58} Sr _{0.4} Co _{0.2} Fe _{0.8} O _{3-δ}) membrane	7
2.2 Asymmetric thin film membrane.....	9
2.3 Wet chemical deposition	12
2.3.1 Stabilization of dispersion	12
2.3.2 Spin-/dip-coating	13
2.3.3 Heat treatment of coating layer	16
2.4 Physical vapour deposition.....	17
2.4.1 DC-Sputtering	17
2.4.2 Magnetron Sputtering.....	17
2.4.3 Reactive sputtering	18
2.4.4 Film Morphology	18
3 Experimental methods.....	20
3.1 Ceramic substrate preparation	20
3.2 Membrane manufacturing	22
3.2.1 Manufacture of inorganic membrane by wet chemical deposition.....	22
3.2.2 Manufacture of inorganic membrane by physical vapour deposition	26
3.3 Characterization methods.....	29
3.3.1 Mercury porosimetry	29
3.3.2 Zeta-potential.....	29
3.3.3 Particle size analysis.....	29
3.3.4 Thermal analysis (TG/DTA)	30

Table of contents

3.3.5 X-ray diffraction (XRD).....	30
3.3.6 Chemical analysis (ICP-OES).....	31
3.3.7 Microscopy.....	32
3.3.8 Gas-tightness measurement.....	33
4 Results and discussion.....	36
4.1 Substrates.....	36
4.2 Characterization of CGO membrane by wet-chemical deposition.....	43
4.2.1 Development of coating liquids.....	43
4.2.2 Development of CGO membrane on WP/VSC (NiO/8YSZ) substrate.....	50
4.3 Characterization of CGO and LSCF membrane by PVD.....	63
4.3.1 Development of interlayer.....	63
4.3.2 Development of CGO membrane on 8YSZ substrate.....	67
4.3.3 Development of CGO membrane on NDCGO-Z substrate.....	81
4.3.4 Development of CGO membrane on $\alpha\text{Al}_2\text{O}_3$ substrate.....	83
4.3.5 Development of CGO membrane on A30A substrate.....	90
4.3.6 Development of CGO membrane on WP/VSC (NiO/8YSZ) substrate.....	94
4.3.7 Development of LSCF membrane on 8YSZ and NDCGO-Z or -A substrates.....	99
5 Summary and outlook.....	103
References.....	109
Acknowledgements.....	117

List of figures

Figure 1 Schematic sketch of CCS processes: Pre-combustion (top), Post-combustion (middle) and Oxy-fuel combustion (bottom). ASU: Air separation unit.	1
Figure 2 Oxygen transport during oxygen permeation [10].....	4
Figure 3 The fluorite crystal structure (AO_2) adopted by CeO_2 . Large red spheres represent O^{2-} ions and small purple spheres Ce^{4+} ions [15].	6
Figure 4 Schematic illustration of perovskite structure.....	7
Figure 5 Schematic illustration of asymmetric structure of membrane	9
Figure 6 Ceramic manufacturing methods [45].	11
Figure 7 Schematic drawing of stabilizing particles [61].	12
Figure 8 Schematic illustration of vertical (a) and horizontal (b) dip-coating process.....	15
Figure 9 Two spherical particles model of neck growth by mass transport mechanisms for sintering (a) and stages of sintering (b) [73].	16
Figure 10 Schematic illustration of DC sputtering device [74].	17
Figure 11 Schematic illustration of the magnetron effect [74].	18
Figure 12 Thornton structure zone model:.....	19
Figure 13 Photograph of prepared substrates:.....	20
Figure 14 Ceramic substrate preparation via vacuum-slip-casting	21
Figure 15 Photographs of centrifuge device (a) and centrifuged CGO nano-dispersion (b). .	22
Figure 16 Horizontal dip-coating method for wet chemical deposition.....	25
Figure 17 Spin-coating method for wet chemical deposition	25
Figure 18 Principle design (a) and facility in IEK-1/FZJ (b) of cluster system CS400 ES	26
Figure 19 Schematic illustration of magnetron sputtering chamber.	27
Figure 20 Schematic illustration of principle of conventional and confocal laser optics when the laser in focus (a) and out of focus (b) [88].	32
Figure 21 Schematic set-up of single gas permeation tester (a) and photograph of testing module (b-outside look, c-inside look).	34

List of figures

Figure 22 Schematic set-up of He-leak tester (a) and photograph of testing module (b).	35
Figure 23 Particle size distribution of 8YSZ and $\alpha\text{Al}_2\text{O}_3$ powder by using Horiba LA-950V2.	36
Figure 24 FEG-SEM images: fracture surfaces of porous substrates which were pre-sintered at 1100 °C for 2h.	37
Figure 25 Surface roughness (mean R_a) of substrates evaluated using VK Analyzer (v. 2.4.0.0, KEYENCE Corporation).....	38
Figure 26 Substrate surface characterization by confocal laser microscope. ‘Laser+color’ and ‘height’ imeages were displayed for each substrate.	39
Figure 27 Gas permeability of 110-8YSZ and 110- $\alpha\text{Al}_2\text{O}_3$ substrates, both pre-sintered at 1100 °C for 2h in air (a), and gas permeability of 140-WP/VSC and reduced 140-WP/VSC substrates (b)..	41
Figure 28 Gas permeability of 8YSZ substrate depending on the presintering temperature (a) and depending on the substrate thickness (b).....	42
Figure 29 Zeta potential of CGO nano-dispersion as a function of pH (a) and CGO concentration (b).	43
Figure 30 Photograph of NDCGOs after centrifuging with the gravity acceleration of 6500xg for 4 min.	44
Figure 31 Particle size (d_{50}) of CGO nano-dispersion as a function of pH (a) and CGO concentration (b).	45
Figure 32 Final concentration (wt.%) of NDCGOs	46
Figure 33 X-ray diffraction patterns: Crystallization behaviour of NDCGO powders as function of temperature of heat treatment.	46
Figure 34 CGO colloidal sols prepared with addition of various amounts of ammonium hydroxide solution.....	47
Figure 35 Particle size of prepared CSCGOs as a function of pH (a) and time (b).	48
Figure 36 Photograph of CSCGO/PVA-Xerogel (a) and XRD patterns of colloidal sol-gel route derived CGO (CSCGO) powders calcined at 500°C for 2h in air (b).	48
Figure 37 TGA-DTA plots of 1.5NDCGO-PVA (1, 2 and 4)-Xerogels.	49
Figure 38 Coating thickness of double 1.0NDCGO and triple 1.5NDCGO layers that were spin-coated with rotation speed 800rpm for 60sec. r.	50

Figure 39 FEG-SEM images of NDCGO on 100-WP/VSC, calcined at 500°C for 2h in air: (a, b) double CGO coatings using 1.0NDCGO and PVA3, (c) double CGO coatings using 1.0NDCGO and PVA2, and (d) triple CGO coatings using 1.5NDCGO and PVA2.....	51
Figure 40 FEG-SEM images of NDCGO on 100-WP/VSC, sintered at 1400°C (+5/-1Kmin ⁻¹) for 5h in air: double CGO coatings using 1.5NDCGO and PVA4.	52
Figure 41 Process parameters for spin-coating with their corresponding symbols (a), and helium flow rate of double coated NDCGO membranes as a function of rotation time (20, 40 and 60 sec.) (b).....	53
Figure 42 Spin-coating parameters (a), their corresponding symbols for double and triple coatings (b), and helium flow rate of double (c) and triple (d) coated NDCGO membranes as a function of spin-coating RPM.....	54
Figure 43 CLM images of thermal cracking behavior of <i>triple</i> CGO coatings on 100-WP/VSC substrate.....	55
Figure 44 Sintering program with different cooling rates.....	55
Figure 45 Laser+color (up) and height (bottom) images by CLM. <i>Triple</i> NDCGO coatings on 100-WP/VSC substrate. '1.5NDCGO + PVA2' was used as a final sol and all layers were calcined at 500 °C at ±2Kmin ⁻¹ for 2h in air. Subsequently, the coated samples were fired at 1400 °C for 5h in air at +3/-5 (a), -1 (b) and -0.5 Kmin ⁻¹ (c). Unity of value in scale bar is μm.	56
Figure 46 SEM (HITACHI) images of the sample displayed in Figure 45 (b) after reducing.	56
Figure 47 FEG-SEM images of NDCGO membranes using various concentrations of NDCGO and PVA4. Double spin-coated layers were calcined at 500 °C at ±2kmin ⁻¹ for 2h in air and fired at 1400 °C at +3/-1Kmin ⁻¹ for 5h in air.....	58
Figure 48 CLM (upper) and FEG-SEM (bottom) images of NDCGO membranes using 2.5NDCGO and various MWs of PVA.....	59
Figure 49 Gastightness evaluation by He leak test. He leak rates were displayed for various concentrations of NDCGO and MWs of PVA.....	60
Figure 50 FEG-SEM images of NDCGO deposited on WPVSC (NiO/8YSZ), fired at 1400 °C at +3/-1Kmin ⁻¹ for 5h under air and further heat treated at 900 °C at +3/-1Kmin ⁻¹ for 3h under Ar/4%H ₂ . For the NDCGO layers a mixture of 1.0NDCGO and PVA2 was used as final coating liquid.....	61
Figure 51 FEG-SEM images of NDCGO topview when the floating bubbles on the sol was not removed (a) and completely cleaned (b). A mixture of 1.0NDCGO + PVA3 was used as final sol and all layers were calcined at 500 °C for 2h in air.....	62
Figure 52 FEG-SEM images of possible failures of sintered CGO film formation, e.g. (a) pinholes due to the sol instability and binder burst, (b) continuous CGO layer due to the substrate valley, and (c) sol infiltration into the very large pore of the substrate.	62

List of figures

Figure 53 XRD patterns of mixtures, “ <i>CGO + LSCF</i> ”, “ <i>8YSZ + LSCF</i> ” and “ <i>8YSZ + CGO</i> ”, which underwent solid state reaction at 1100 °C for 2h in air.	65
Figure 54 FEG-SEM images of surface morphology of NDCGO and CSCGO (500°C for 2h in air).	65
Figure 55 XRD patterns of aluminum oxide powders derived via AlOOH colloidal sol-gel route, sintered at 500°C and 1100°C for 2h in air.	66
Figure 56 FEG-SEM images of fracture surface of 8YSZ substrates, presintered at 1100 °C (a), 1120 °C (b), 1140 °C (c) and 1180 °C.	67
Figure 57 Photographs of RMS-CGO on 8YSZ substrates with various bias powers. Substrate temperature was kept at 800°C for all RMS runs onto 8YSZ substrates.	68
Figure 58 FEG-SEM images of RMS-CGO on 110-8YSZ with 300W bias, at the point of middle (a) and outside (b, c), i.e. blue circle areas of photograph in Figure 57.....	69
Figure 59 FEG-SEM images of RMS-CGO on 110-8YSZ with bias power 0, 100 and 300 W.	70
Figure 60 FEG-SEM images of RMS-CGO on 112-8YSZ with bias power 0 and 400 W.	71
Figure 61 Gastightness evaluation by single gas permeation test using helium (a) and nitrogen (b) gases for RMS-CGO membranes deposited on 8YSZ substrates.....	72
Figure 62 Gas-tightness evaluation of RMS-CGO membranes on 114- and 118-8YSZ substrate using helium leak test and displayed as a function of bias power applied to the substrates..	73
Figure 63 FEG-SEM images of RMS-CGO membranes on 114-8YSZ substrates with various bias powers.....	74
Figure 64 CGO membrane thickness as a function of bias power applied to substrate during RMS.	75
Figure 65 Derived four-zone-model for membranes in bias-applied RMS with substrate temperature 800 °C.....	76
Figure 66 XRD patterns of RMS-CGO membranes as a function of substrate bias, which were deposited on 110-8YSZ substrates at substrate temperature 800 °C. XRD patterns of sintered NDCGO powder was included in for comparison.	77
Figure 67 XRD patterns of RMS-CGO membranes as a function of substrate bias, which were deposited on 114-8YSZ substrates at substrate temperature 800 °C.	78
Figure 68 XRD patterns of RMS-CGO membranes as a function of substrate bias, which were deposited on 114-8YSZ substrates at substrate temperature 800 °C. Figure 67 was magnified for observation of peak shift when substrate bias was applied.	78

Figure 69 Laser+color image by confocal laser microscope. (a) 114-8YSZ substrate surface prior to RMS, and (b) sputtered CGO membrane with substrate bias 200W.....	79
Figure 70 Surface roughness (mean R_a) of the substrate prior to RMS (R_{a-s}) and sputtered CGO membrane (R_{a-m}). The three images of left side involving scratch (in Figure 69) were excluded for evaluating the roughness.	79
Figure 71 Surface roughness (mean R_a) of CGO membranes deposited on 110-, 112-, 114- and 118-8YSZ substrates as a function of applied bias power. R_{a-m} is the mean R_a of deposited membrane and the numbers correspond to the presintering temperature of the 8YSZ substrates supporting membranes.	80
Figure 72 Photographs of RMS-CGO on NDCGO (CGO interlayer supported by 110-8YSZ) with bias power 0, 100 and 300 W.....	81
Figure 73 FEG-SEM images of RMS-CGO membrane on 80-1.0NDCGO-Z when bias power 300W was applied.	82
Figure 74 Photographs of RMS-CGO on 110- $\alpha\text{Al}_2\text{O}_3$ substrate when bias power 0, 100, 300 and 400 W were applied.....	83
Figure 75 FEG-SEM images of RMS-CGO membranes on 110- $\alpha\text{Al}_2\text{O}_3$ substrates. Bias power 0, 100, 300 and 400W were applied to the substrate during sputtering process. (LY: light yellow part (outside) and DY: dark yellow part (middle) of sample in Figure 74 400W).....	84
Figure 76 FEG-SEM images of RMS-CGO membranes on 110- $\alpha\text{Al}_2\text{O}_3$ substrates with bias assist 100 and 300W. The broken fracture surface was mounted and polished.	85
Figure 77 Schematic illustration of suggested hypothesis on inhomogeneous CGO membrane formation.	85
Figure 78 Gastightness evaluation by single gas permeation test using helium (a) and nitrogen (b) gases for RMS-CGO membranes deposited on $\alpha\text{Al}_2\text{O}_3$ substrates.	86
Figure 79 XRD results measured in Bragg-Brentano-Geometry for 100W-CGO membrane on $\alpha\text{Al}_2\text{O}_3$	87
Figure 80 FEG-SEM images of 300W-CGO membrane deposited on 110- $\alpha\text{Al}_2\text{O}_3$ substrate after additional heat-treatment at 1000 °C and 1200 °C $\pm 2\text{Kmin}^{-1}$ for 5h in air.	88
Figure 81 Photographs of deposited CGO film on uncoated and platinum-coated $\alpha\text{Al}_2\text{O}_3$	88
Figure 82 FEG-SEM images of RMS-CGO membranes on platinum-coated $\alpha\text{Al}_2\text{O}_3$ substrates. Bias power 0 and 400W were applied to the substrate during sputtering process. Scale bar: 200nm, 1 μm and 200nm, from left image.....	89
Figure 83 Particle size distribution of ALOOH colloidal sol for interlayer ($d_{50} \sim 30\text{nm}$) (a) and FEG-SEM image of their asymmetric membrane structure (b).	90

List of figures

Figure 84 Gas permeability A30A substrates presintered at 1100 °C for 2h in air. Gas flow rate per measuring area is displayed as a function of pressure differential. Gas permeability of 110- α Al ₂ O ₃ shown in Figure 27 (a) was also displayed for comparison.	91
Figure 85 Photographs of RMS-CGO on A30A substrates with bias power 0, 100 and 400 W at 800°C and RT.	91
Figure 86 CLM image of outside area on RMS-CGO on A30A when bias power 400W was applied. Laser + color image (a) and height 3d-image (b).	92
Figure 87 FEG-SEM images of microcracks in RMS-CGO on A30A biased with 100W at substrate temperature of 800 °C (SE images of tilted sample: a, c and BSE image of fracture surface: b).	92
Figure 88 FEG-SEM images of RMS-CGO on A30A. Investigation in microcracks formation depending on bias power and substrate temperature during RMS, and their membrane fracture surface.	93
Figure 89 Photographs of RMS-CGO on 100- and 140-WP/VSC substrates without and with bias power 400W.	94
Figure 90 FEG-SEM images of sputtered CGO membrane on 100- and 140-WP-VSC substrates, when bias power 0 and 400 W were applied.	95
Figure 91 Gas-tightness estimation by He-leak test.	96
Figure 92 Images of sputtered CGO membrane after heat treatment at 900°C for 3h under reducing atmosphere using Ar/4%H ₂ . (a: photograph, c: image by SEM-HITACHI, and the others by FEG-SEM) – (a, b, d): Top-view, (e, f): fracture surface, (c): polished cross-section.	97
Figure 93 BSE image by FEG-SEM (a) and EDX result (b) at the point of spectrum 1 in BSE image for reduced CGO membrane on 140-WP/VSC substrate.	98
Figure 94 Photographs of dcMS-LSCF membrane deposited on 8YSZ (a), 1.0NDCGO/110-8YSZ 1000°C2h (b), CSCGO/1.0NDCGO/110-8YSZ 1000°C2h (c) and 1.0NDCGO/110- α Al ₂ O ₃ 1000°C2h (d).	99
Figure 95 FEG-SEM images of dcMS-LSCF membrane on 110-8YSZ (left) and on 100-1.0NDCGO-Z (right). Topview: a,b,c,d (all SE) and fracture surface: e,f (SE) and g,h(BSE).	100
Figure 96 XRD results measured in Bragg-Brentano-Geometry for dcMS-LSCF membrane deposited on 110-8YSZ without bias assist.	101
Figure 97 Gas-tightness estimation by He-leak test for MS-LSCF membranes on various substrates	102

List of tables

Table 1 Requirements of substrate, interlayer and membrane (top-layer).	10
Table 2 Overview of literatures for asymmetric membranes with $< 100\mu\text{m}$ thickness.	11
Table 3 Important parameters of two possible compaction modes during dip-coating	14
Table 4 Microstructure description of Thornton zone model.....	19
Table 5 Prepared CGO nano-dispersion (NDCGO) with 0.05M HNO_3 solvent	22
Table 6 Specification of purchased PVAs.....	23
Table 7 Preparation of PVA solutions with various molecular weights.	24
Table 8 Volume ratio of sol : PVA for final coating solution.....	24
Table 9 Acid digestion for the sample preparation of ICP-OES	31
Table 10 Results of mercury porosimetry measurement for pre-sintered substrates.	37
Table 11 Stoichiometry of prepared NDCGO powder (relative error $\pm 3\%$ of wt.%).	47
Table 12 Stoichiometry of prepared CSCGO powder (relative error $\pm 3\%$ of wt.%).	49
Table 13 Microcrack formation in double coated NDCGO membrane after calcination ($500^\circ\text{C}/2\text{h}/\text{air}$), depending on the concentration of NDCGO and on the molecular weight (MW) of PVA, observed by confocal laser microscope.	57
Table 14 Prepared interlayers for sputtering process	63
Table 15 Ultrasonication cleaning before introducing samples into the PVD chamber.	64
Table 16 Heat-treatment profile of prepared 8YSZ substrates.....	67
Table 17 Prepared WP-VSC substrates for RMS-CGO.....	94
Table 18 Calculated stoichiometry of LSCF powder and dcMS-LSCF films.	102
Table 19 Summary of all prepared membranes with gastightness and noticeable remarks...	107

List of abbreviations

ASU	Air separation unit
A30A	$\alpha\text{Al}_2\text{O}_3$ coating layer on $\alpha\text{Al}_2\text{O}_3$ substrate
BSCF	$\text{Ba}_{0.5}\text{Sr}_{0.5}\text{Co}_{0.8}\text{Fe}_{0.2}\text{O}_{3-\delta}$
CCS	Carbon capture and storage
CGO	Gd-doped ceria generally and $\text{Ce}_{0.8}\text{Gd}_{0.2}\text{O}_{2-\delta}$ in this work
CLM	Confocal Laser Microscopy
CRP	Constant drying rate period
CS	Colloidal sol
CVD	Chemical vapour deposition
DCCA	Drying chemical controlling additive
DLS	Dynamic light scattering
DLVO	Derjaguin & Landau and Verwey & Overbeek
EBP	Emslie, Bonner and Peck
EDL	Electric double layer
FCC	Face centered cubic
FEG-SEM	Field Emission Gun Scanning Electron Microscope
GDC	Gd-doped ceria
ICP-OES	Inductively Coupled Plasma with Optical Emission Spectroscopy
IEP	Isoelectric point
IEK-1	Institute of Energy and Climate in Forschungszentrum Jülich GmbH
IPCC	Intergovernmental Panel on Climate Change
IUPAC	International Union of Pure and Applied Chemistry
LSCF	$\text{La}_{0.58}\text{Sr}_{0.4}\text{Co}_{0.2}\text{Fe}_{0.8}\text{O}_{3-\delta}$
MIEC	Mixed ionic-electronic conductor
MS	Magnetron sputtering
MW	Molecular weight
ND	Nano-dispersion

OTM	Oxygen transport membrane
PSD	Particle size distribution
PVA	Polyvinyl alcohol
PVD	Physical vapour deposition
RG	Reactive gas
RMS	Reactive magnetron sputtering
RPM	Rotation per minute
SEM	Scanning Electron Microscope
SOFC	Solid oxide fuel cell
TG/DTA	Thermo-gravimetry/ differential thermal analysis
WCD	Wet chemical deposition
WP/VSC	Warm-pressed NiO/8YSZ substrate with vacuum-slip-cast NiO/8YSZ interlayer
XRD	X-ray diffraction
8YSZ	8 mol% Y_2O_3 stabilized ZrO_2

List of symbols

α	Thermal expansion coefficient
δ	Substoichiometric
θ	Diffraction angle of X-ray diffraction (XRD)
σ_{el}	Electronic conductivity
σ_{ion}	Ionic conductivity
e'	Lattice electron in Kröger-Vink-Notation
$h\cdot$	Electron hole in Kröger-Vink-Notation
\varnothing	Diameter
A	Measuring area
Ds	Self-diffusion coefficient of oxygen anions
D*	Tracer diffusion coefficient
j	Permeation rate
F	Faraday constant
ks	Surface-exchange coefficient
L	Thickness of membrane
Lc	Characteristic thickness of membrane
mbar-l/sec	Helium flow rate under constant pressure (p) at room temperature
ml/min	Flow rate under atmospheric conditions (room temperature, p=1,013 bar)
p	Pressure
P' _{O₂}	Oxygen partial pressure on feed side
P'' _{O₂}	Oxygen partial pressure on permeate side
R	Gas constant
T	Temperature
t	Time
v	Volume
vol. %	Volume percent in %
wt. %	Weight percent in %

1 Introduction

1.1 CO₂ capture in fossil power plant

All scenarios for the future global energy requirements anticipate that fossil fuels such as oil, coal and natural gas remain the dominant energy sources in 2035 to meet increasing demand for electricity [1]. However, fossil fuel power plants are by far the biggest point sources of CO₂ and contribute more than 40% to the world-wide anthropogenic CO₂ emissions [2]. Carbon capture and storage (CCS) is an effort to capture CO₂ from fossil fuel power plants and store it in appropriate geologic formations instead of releasing it into the atmosphere. IPCC (Intergovernmental Panel on Climate Change) estimates that the economic potential of CCS could be between 10% and 55% of the total carbon mitigation effort until year 2100 [3]. The capture step is by far the most costly component of CCS and research is underway to find more efficient and cost effective capture processes.

Three CCS power plant concepts are under development, i.e. Pre-combustion, Post-combustion and Oxy-fuel combustion. **Figure 1** shows the schematic sketch of these processes. The gas separation systems are required for N₂/O₂, H₂/CO₂ and N₂/CO₂ separation in CCS processes.

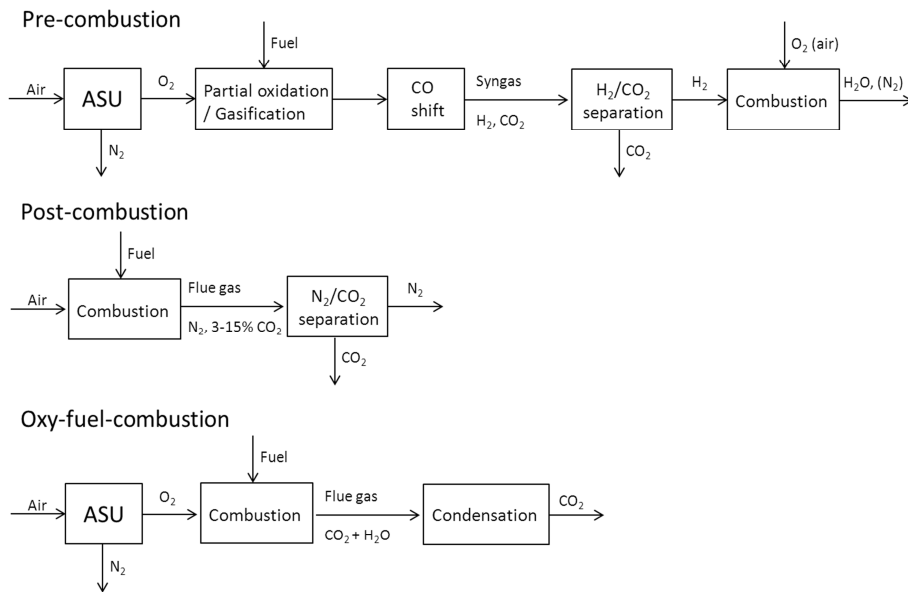
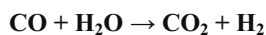


Figure 1 Schematic sketch of CCS processes: Pre-combustion (top), Post-combustion (middle) and Oxy-fuel combustion (bottom). ASU: Air separation unit.

1. Introduction

Pre-combustion

In pre-combustion process the CO₂ gas is captured from energy source before combustion step. First of all, the oxygen is separated from air via air separation unit (ASU). The fuel (Methane, natural gas or coal) is partially oxidized with the separated oxygen forming hydrogen-rich syngas, a mixture of mainly H₂ and CO (partial oxidation of gaseous and liquid fuels or gasification of solid fuel). With further addition of steam in water gas shift reactor, the syngas is subsequently converted to CO₂ from CO in which additional H₂ is generated.



Equation 1

This reaction is slightly exothermic, yielding 41 kJ/mol [4]. Ultimately the CO₂ is separated from the mixture of 15-40% CO₂ with H₂ at high pressure (15-40 bar), and condensed with the residual steam to be transported [5]. The obtained H₂ can be combusted in the gas turbine of the power plant and therefore electricity is produced with minimal CO₂ emissions.

Post-combustion

In post-combustion process the CO₂ gas is captured from flue gas which is produced by combustion of a fossil fuel. The fuel is usually burned with air (approx. 80% nitrogen) in current power plants and generates a flue gas at atmospheric pressure with a CO₂ concentration <15% [6, 7], followed by a CO₂ separation process. Due to the low thermodynamic driving force (CO₂ partial pressure) for CO₂ separation from flue gas, typically <0.15 atm, the development of cost-effective capture processes for the low partial pressure is a significant technical challenge [6, 7]. The leading option is an absorption process using amine based solvents [5].

Oxy-fuel-combustion

In oxy-fuel-combustion process the O₂ is first separated from air via air separation unit (ASU) (O₂ purity >95% [6]) and used instead of air with recycled flue gas in the energy conversion process. The resulting flue gas is then a high purity CO₂ stream (CO₂ purity >80% [8]), which can be captured more easily.

Membrane based gas separation systems are noteworthy among technological options for CCS due to the significantly lower efficiency losses compared with conventional separation technologies. The membranes, particularly, for oxygen separation are used also in other field such as chemical industry, e.g. oxygen transport membranes (OTM) for oxidative coupling of methane (OCM), $2\text{CH}_4 + \text{O}_2 \rightarrow \text{C}_2\text{H}_4 + 2\text{H}_2\text{O}$, and syngas production, $\text{CH}_4 + \frac{1}{2} \text{O}_2 \rightarrow \text{CO} + 2\text{H}_2$.

1.2 Gas separation membranes for CCS

For each CCS concept different kinds of membranes are proposed. Microporous ceramic membranes that operate at temperatures up to 400°C can be used for pre-combustion and

possibly for post-combustion. Polymeric membranes which have operating temperature up to 200°C are candidates for post-combustion and possibly pre-combustion processes. Dense ceramic membranes (MIEC membranes) operating at temperature up to 800-900 °C are necessary for oxyfuel combustion and are possible candidates for pre-combustion for operating at approx. 600°C [9].

In recent years, inorganic membranes referring to the gas separation technology have received increasing attention due to their better chemical, mechanical, thermal and pressure stability than organic membrane. The inorganic membrane can be further categorized according to their structure into porous or dense membrane. The porous membranes offer relatively high permeability but low selectivity compared with the dense membranes. Application of dense inorganic membranes is primarily for highly selective separation of gases such as H₂ and O₂. Particularly, oxygen transport membrane (OTM) consisting of gastight mixed ionic and electronic conductor (MIEC membrane) exhibit great potential for oxygen separation, realizing in a more efficient way compared with conventional methods such as cryogenic air separation and pressure swing adsorption. However, the dense membranes possess relatively low permeability, a limit for industrial application. Therefore, there are many efforts to improve the permeation rate of dense membrane, e.g. by controlling thickness of the membrane layers (thickness reduction) to minimize diffusion barriers, by applying catalytic surface activation to overcome slow surface exchange reaction kinetics, and by thin film nano-structuring, generating new diffusion paths through the grain boundaries in a nanocrystalline matrix.

1.3 Objective of this work

The main objective of this work is the development of MIEC membranes with the reduction of membrane thickness to approx. 1 µm or less. A multi-layered asymmetric membrane structure was proposed to develop the thin film membrane with a sufficient mechanical stability, i.e. high permeable porous substrate was used. Two approaches were proposed to deposit thin film membrane layers on porous substrates, such as wet chemical deposition and physical vapor deposition. CGO (Ce_{0.8}Gd_{0.2}O_{2-δ}) and LSCF (La_{0.58}Sr_{0.4}Co_{0.2}Fe_{0.8}O_{3-δ}) were selected as membrane materials in this work. The specific tasks are listed as follows.

1. Preparation and characterization of substrates
2. Preparation and characterization of coating liquids.
3. Manufacture of CGO membrane by spin-coating.
4. Manufacture of CGO membrane by reactive magnetron sputtering.
5. Manufacture of LSCF membrane by magnetron sputtering.
6. Evaluation of gastightness of developed membranes.

2 Fundamentals and background

2.1 Mixed ionic-electronic conducting membranes for O₂/N₂ separation

The pre-combustion and oxyfuel-combustion require oxygen separation from air that can be met with oxygen transport membranes (OTM). They are associated with significantly lower efficiency losses compared with conventional separation technologies, e.g. cryogenic air separation. OTM consist of gas-tight mixed ionic electronic conductors (MIEC), which allow oxygen ion diffusion through vacancies in the crystal lattice without an external electrical short circuit. The driving force for oxygen to permeate through this MIEC membrane is the chemical potential gradient, i.e. oxygen partial pressure gradient across the membrane. The flux of oxygen ions is charge compensated by a simultaneous flux of electrons or electron holes. In addition to the solid-state diffusion, the surface-exchange reactions on two interfaces (1 and 2) influence the transport kinetics. Thus, oxygen transport is limited by solid-state diffusion and by surface oxygen exchange, as shown in **Figure 2**. If neither cracks nor connected-through pores exist, the selectivity of membrane is infinite.

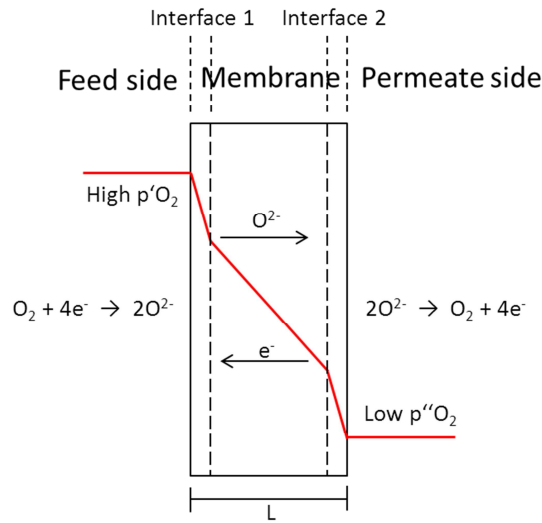


Figure 2 Oxygen transport during oxygen permeation [10].

As mentioned, the rate of oxygen permeation in general, is decided by bulk diffusion of membrane and by surface oxygen-exchange reactions. For thick membranes, e.g. $L \geq 1\mu\text{m}$,

bulk diffusion (lattice diffusion) is determining the rates, the oxygen permeation is given by Wagner equation [11, 12].

$$J_{O_2} = - \frac{RT}{4^2 F^2 L} \cdot \int_{\ln p'_{O_2}}^{\ln p''_{O_2}} \frac{\sigma_{el} \sigma_{ion}}{\sigma_{el} + \sigma_{ion}} d \ln P_{O_2} \quad \text{Equation 2}$$

where L is the membrane thickness, F is the Faraday constant, R is the gas constant, T is the operating temperature, σ_{el} is the electronic conductivity, σ_{ion} is the ionic conductivity and P'_{O_2} and P''_{O_2} are the oxygen partial pressure on feed side and permeate side, respectively. Assuming that the conductivities remain constant over the cross section, the Wagner equation can be simplified as follows:

$$J_{O_2} = \frac{RT}{4^2 F^2 L} \cdot \frac{\sigma_{el} \sigma_{ion}}{\sigma_{el} + \sigma_{ion}} \cdot \ln \frac{p'_{O_2}}{p''_{O_2}} \quad \text{Equation 3}$$

From **Equation 3**, it is understood that increasing oxygen permeation is possible with optimization of four factors, i.e. ambipolar conductivity as intrinsic material property, temperature and oxygen partial pressures as operating condition, and membrane thickness as geometric factor. The conductivities of selected material should be very high. The surrounding conditions such as the oxygen partial pressures on both sides of the membrane and the operating temperature are also crucial but given by the application, and thus very limited. In addition, the membrane thickness is inversely proportional to the oxygen permeation. Thus the membrane thickness should be reduced for higher oxygen permeation but there is a limit due to the surface oxygen-exchange reactions involving reaction steps for the reduction of oxygen on the feed side that include adsorption on the membrane surface, dissociation, charge transfer, surface diffusion of intermediate species, e.g. O_{ads} , O_{ads}^- and O_{ads}^{2-} , and incorporation into the lattice in the near-surface layer. It is generally assumed that the reverse direction of the reaction steps leads to the re-oxidation of oxygen anions on the permeate side. Beneath a characteristic thickness L_c the surface oxygen-exchange reactions become rate limiting. In this case, the oxygen permeation can be modified as follow [12]:

$$J_{O_2} = \frac{RT}{4^2 F^2} \cdot \frac{1}{L + 2L_c} \cdot \frac{\sigma_{el} \sigma_{ion}}{\sigma_{el} + \sigma_{ion}} \cdot \ln \frac{p'_{O_2}}{p''_{O_2}} \quad \text{Equation 4}$$

The L_c can be derived from ^{18}O - ^{16}O isotope exchange experiments and is defined as follows [12]:

$$L_c = \frac{D_s}{k_s} = \frac{D^*}{k_s} \quad \text{Equation 5}$$

where k_s is the surface-exchange coefficient, D_s is the self-diffusion coefficient of oxygen anions and D^* is the tracer diffusion coefficient. If correlation effects can be neglected, $D_s = D^*$. For mixed conducting oxides with perovskite-related structures, L_c has been reported to vary in the range between 20 and 3000 μm depending on composition, temperature and oxygen partial pressure [13].

2.1 1 Fluorite-structured CGO ($\text{Ce}_{0.8}\text{Gd}_{0.2}\text{O}_{2-\delta}$) membrane

Fluorite structure is the classic crystal structures for solid oxide fuel cell electrolytes [14], exhibiting the fast oxygen ion conductivity when doped with aliovalent cations. The fluorite-structured materials have general formula AO_2 , where A is a large tetravalent cation (i.e. Ce^{4+} for ceria). In fluorite unit cell the cations occupy the face centered cubic (FCC) lattice sites, while anions (i.e. O^{2-}) are located at eight tetrahedral sites. The four remaining octahedral sites remain vacant. **Figure 3** shows the ideal fluorite structure of ceria material (CeO_2), which is the most important material for fluorite structured mixed conductors.

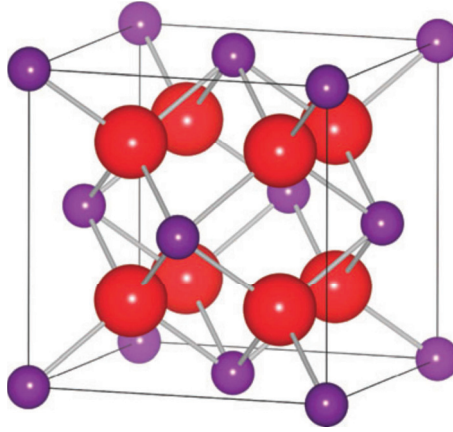


Figure 3 The fluorite crystal structure (AO_2) adopted by CeO_2 . Large red spheres represent O^{2-} ions and small purple spheres Ce^{4+} ions [15].

If tri- or divalent dopant is added to the host material, oxygen vacancies are introduced to maintain overall charge neutrality as charge compensating defects. Gd^{3+} or Sm^{3+} -doped ceria exhibits the highest conductivity among all extensively investigated doped ceria (e.g. Ca^{2+} , Sr^{2+} , Y^{3+} , La^{3+} , Gd^{3+} and Sm^{3+}) because of the smallest association enthalpy between the dopant cation and oxygen vacancy in the fluorite lattice [16, 17]. The lattice parameter of doped ceria expands with increasing radius of the dopant cation [18] and concentration of dopant cation [19]. Gd-doped ceria (GDC or CGO) shows highly undisturbed crystal lattice when the vacancies are introduced, since the host and dopant ion are very close in size [20], which seems to be the most ideal dopant. The radii of Ce^{4+} , Gd^{3+} and Sm^{3+} are 0.096, 0.105 and 0.108 nm, respectively [18].

The defect reaction for gadolinia doping in ceria can be presented in Kröger-Vink notation [21]:



The main advantage of CGO membranes include a higher ionic conductivity than that of stabilized ZrO_2 (YSZ) particularly at lower temperatures (500-700°C) [14, 15, 22]. CGO produces the electronic conductivity at low oxygen partial pressure ($P_{\text{O}_2} < 10^{-12}$ atm at 1173K) due to the partial reduction of Ce^{4+} to Ce^{3+} [23], which realize the desirable mixed ionic-electronic conducting property. The optimal Gd-dopant concentrations is 10-20% for the best conductivity of Gd-doped ceria [14]. According to Steele [24], 10 mol% Gd-doped ceria has the highest lattice conductivity but 20 mol% Gd-doped ceria often has higher total conductivity because its grain boundary contribution seems to be more tolerant of unavoidable impurities (particularly SiO_2) that cause a decrease of the ionic conductivity in the grain boundaries.

2.1.2 Perovskite-structured LSCF ($\text{La}_{0.58}\text{Sr}_{0.4}\text{Co}_{0.2}\text{Fe}_{0.8}\text{O}_{3-\delta}$) membrane

Perovskite is one of the most frequently encountered structures in mixed conducting inorganic compounds. Cubic perovskite structure is an ideal perovskite structure, which has ABO_3 stoichiometry, as seen in **Figure 4**, where the A is a bigger cation, such as a rare earth, existing between BO_6 octahedra and B is a smaller cation, frequently a transition metal, 6-coordinated by the anions in the lattice. CaTiO_3 compound is the representative material having perovskite structure. The general compositional formula of perovskite is $\text{A}^{2+}\text{B}^{4+}\text{O}_3$ ($\text{A}^{1+}\text{B}^{5+}\text{O}_3$ or $\text{A}^{3+}\text{B}^{3+}\text{O}_3$ are also possible) [25]. In many cases the BO_6 octahedra are distorted, due to the presence of the A cation.

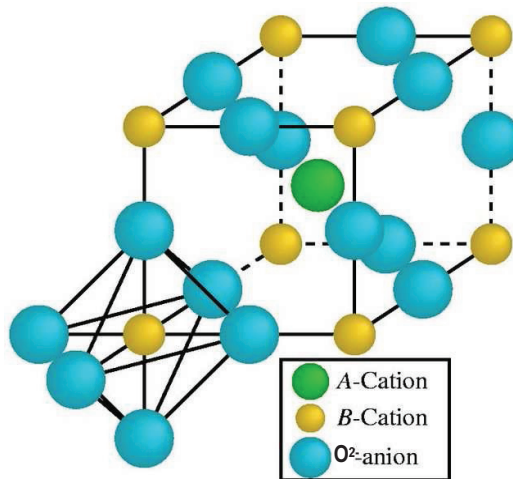


Figure 4 Schematic illustration of perovskite structure.

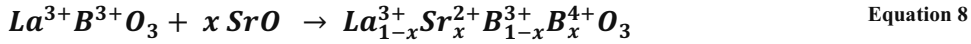
The tolerance limits of the cationic radii in the A and B sites are defined by the Goldschmidt factor [26], which is based on geometric considerations, as followed:

2. Fundamentals and background

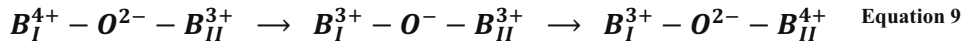
$$t = \frac{R_A + R_O}{\sqrt{2} (R_B + R_O)} \quad \text{Equation 7}$$

where R_A , R_B and R_O are the radii of the respective ions. Although for an ideal perovskite t is unity, this structure is also found for lower t -values between $0.75 < t < 1$. The desired cubic perovskite structure appears for tolerance factors t very close to one [27]. The cubic structure exist at $0.91 < t < 1.0$, and when A-cations are too small to fit into their interstices there are several possible structures, e.g. orthorhombic or rhombohedral structures, for $0.75 < t < 0.91$.

According to the combination of chemical composition in perovskite structures, various properties were discovered such as superconductivity, ferroelectricity, piezoelectricity, giant magnetoresistance, or mixed ionic- and electronic conductivity [28]. The mixed ionic and electronic conducting (MIEC) perovskite materials have been extensively investigated for oxygen separation membranes, besides partial oxidation of methane to syngas and electrodes of solid oxide fuel cells (SOFC) [10, 12]. The ionic conductivities can be enhanced greatly by substituting lower valence cations for both A and B sites (such as partial substitution of La^{3+} by Sr^{2+} in LaCoO_3), because the deficiency from the substitution brings an increase of oxide ion vacancies. The electronic conductivity can be also increased by the addition of aliovalent cations. The B-cation is oxidized and thus formed an electron hole h' as following mechanism:



The electronic charge transfer occurs in many perovskites via the “*polaron hopping*” process in which an electron hole h' of a B-ion *jumps* to the next [29]. According to Zener [30], the process also involves a charge change of the oxygen ion as follows:



Temperature and oxygen partial pressure determine whether charge compensation occurs by an increased valence of the transition metal ion at the B site or by the formation of ionized oxygen vacancies [12].

Much of the research efforts are focused on doped perovskite oxides $\text{A}_{1-x}\text{A}'_x\text{B}_{1-y}\text{B}'_y\text{O}_{3-\delta}$ (A = lanthanide and Y, A' = Ca, Sr, Ba, B or B' = Mg, Al, Ti, Cr, Mn, Fe, Co, Ni, Cu, Ga, Zr, $0 \leq x \leq 1$, $0 \leq y \leq 1$). Among the various combination of chemical compounds, $\text{Ba}_{0.5}\text{Sr}_{0.5}\text{Co}_{0.8}\text{Fe}_{0.2}\text{O}_{3-\delta}$ (BSCF) membrane appears to be the material with very high oxygen flux (1.4 ml/cm².min at 950°C with 1.8 mm thickness), but they degrade very quickly under operating conditions [31].

Teraoka et al. [32-35] have firstly reported high oxygen flux through $\text{La}_{1-x}\text{Sr}_x\text{Co}_{1-y}\text{Fe}_y\text{O}_{3-\delta}$ perovskite membranes, which ionic conductivity exhibited one to two orders of magnitude higher than that of the stabilized zirconia at the same temperatures (e.g. 700-1000 °C) in air [34]. Since then, increasing attentions have been attracted on the research of this composition

[36-39]. Especially, $\text{La}_{0.58}\text{Sr}_{0.4}\text{Co}_{0.2}\text{Fe}_{0.8}\text{O}_{3-\delta}$ (LSCF) membrane keeps receiving attention due to its significant levels of both ionic and electronic conductivity.

LSCF membrane shows lower oxygen permeation rate than BSCF. However, LSCF membrane has good chemical stability which was observed at least in the related material $\text{La}_{0.60}\text{Sr}_{0.4}\text{Co}_{0.2}\text{Fe}_{0.8}\text{O}_{3-\delta}$ [40]. Among membranes using in power plants, where the membrane can come into contact with aggressive gases like CO_2 , SO_2 , H_2O and others, LSCF is a good compromise due to its high permeation rate and a good degree of chemical stability [41].

2.2 Asymmetric thin film membrane

Design and requirements

For large-scale application of oxygen separation membrane technology, a maximum oxygen flux has to be achieved. One of the logical approach to increase the oxygen flux at a given temperature and oxygen partial pressure gradient is the reduction of the membrane thickness to the micrometer range or even below, since the permeate path of the membrane and thus flow resistance is reduced. For the thin film membrane, the substrate is essential to assist mechanical stability of the membrane. Usually, an inorganic gas separation membrane has an asymmetric structure consisting of three different parts as shown in **Figure 5**.

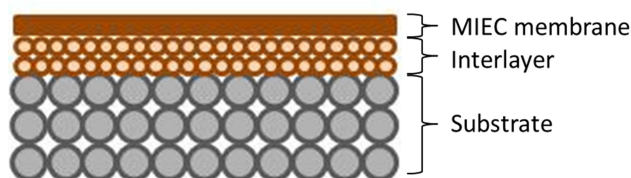


Figure 5 Schematic illustration of asymmetric structure of membrane

Usually macroporous (pore size $> 50\text{nm}$, IUPAC definition [42]) substrate is used with a thickness of a few millimeters, giving the necessary mechanical stability in the entire system. The substrate should have sufficiently high permeability. The roughness and pore size of substrate surface are important factors for membrane coating. When selecting the substrate material, good match in the expansion coefficient with membrane layer is the significant requirement to be specially considered. There are two different types of substrate, i.e. tubular and planar substrate, which are produced e.g. by extrusion, and by tape casting or vacuum-slip-casting, respectively [43, 44].

If the substrate has defect, large pores or rough surface, thin films cannot be coated defect-free. In these cases, interlayer has to be developed that improve the substrate surface quality, e.g. defect-covering, reduction in pore size and surface roughness. In the case of chemical

2. Fundamentals and background

incompatibility between substrate and membrane, the interlayer can additionally act as buffer layer.

The oxygen separation membrane should be gas-tight and very thin for high oxygen flux according to **Equation 2**. For proper performance, i.e. infinite selectivity, no defect or inhomogeneity is allowed to exist in the membrane layer.

The substrate, interlayer and membrane (top-layer) have to fulfil the following requirements as summarized in **Table 1**.

Table 1 Requirements of substrate, interlayer and membrane (top-layer).

Substrate	Interlayer	Membrane (Top-layer)
Chemical, thermal and mechanical stability	Chemical, thermal and mechanical stability	Chemical, thermal and mechanical stability
Gas permeability	Gas permeability	Gas-tightness
Suitable pore size, surface roughness	Improvement of substrate surface quality (pore size and roughness)	Minimum thickness
Small mismatch with interlayer and membrane materials	Buffer layer in case of chemical incompatibility between membrane and substrate	

Manufacturing

The thin film is manufactured on the selected substrates by depositing atoms, molecules or ions that exist in gas, solid or liquid form. **Figure 6** shows the ceramic film manufacturing methods which are available in Forschungszentrum Jülich IEK-1. The film manufacturing using gas or solid form can be mainly divided to physical vapor deposition (PVD) and chemical vapor deposition (CVD). In PVD method, the evaporation and sputtering coating methods are frequently used and they can be distinguished depending on how to produce the plasma. The evaporation coating is the deposition method that heats the materials under vacuum and the sublimed (solid to vapor) or evaporated (liquid to vapor) particles deposit on the substrate. The sputtering coating method uses the collision of ions to the solid target and the ejected atoms or molecules are condensed on the substrate. In CVD method, the vaporized materials undergo the chemical reaction such as pyrolysis, oxidation, reduction, etc. and are deposited as desired film. The film manufacturing using liquid form includes the spin coating, dip coating and spray coating, which are usually used if smooth coating on flat circular substrate is required, if a relatively small planar structure is coated, and if a structure with a lot of irregularities is coated, respectively. This work focuses on the sputtering coating and spin-/dip-coating methods for asymmetric membrane or interlayer manufacturing and more theoretical details are described in following sections. Furthermore, the overview of literatures for asymmetric membrane with $< 100\mu\text{m}$ thickness, i.e. dense membrane on porous substrate, were summarized in **Table 2**.

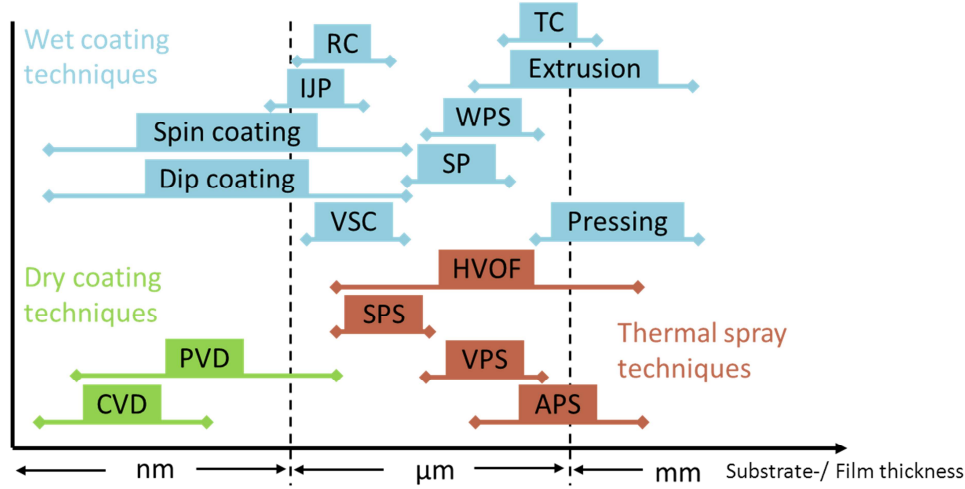


Figure 6 Ceramic manufacturing methods [45].

(CVD-chemical vapour deposition, PVD-physical vapour deposition, APS- atmospheric plasma spraying, VPS- vacuum plasma spraying, SPS- suspension plasma spraying, HVOF- high velocity oxyfuel spraying, VSC- vacuum slip casting, SP- screen printing, WPS- wet powder spraying, IJP- ink jet printing, RC- roll coating, TC- tape casting)

Table 2 Overview of literatures for asymmetric membranes with $< 100\mu\text{m}$ thickness.

Material	Membrane Th.	Method	Material	Substrate P./D.	Method	Ref.
CeO_2	$0.5\mu\text{m}$	SG Spin coating	CeO_2 coated with interlayer 'sputtered CeO_2 ($\sim 1\mu\text{m}$)'	30 % / $\sim 3\mu\text{m}$	Uni-axial Pressing	[46]
CeO_2	$2\text{--}25\mu\text{m}$	SG Dip coating	$\alpha\text{-Al}_2\text{O}_3$	$\sim 50\%$ / $\sim 0.2\mu\text{m}$	Pressing	[47]
$\text{Ce}_{0.8}\text{Gd}_{0.2}\text{O}_{1.90}$	$1\text{--}2\mu\text{m}$	UVSG Spin coating	$\text{Ce}_{0.8}\text{Gd}_{0.2}\text{O}_{1.90}$			[48]
$\text{Ce}_{0.9}\text{Gd}_{0.1}\text{O}_{1.95}$	$25\mu\text{m}$	ESD	$\text{NiO- Ce}_{0.9}\text{Gd}_{0.1}\text{O}_{1.95}$		Solid state sintering	[49]
$\text{Ce}_{0.9}\text{Gd}_{0.1}\text{O}_{1.95}$ - 2mol% Co	$27\mu\text{m}$	TCL and co-firing	$\text{Ce}_{0.9}\text{Gd}_{0.1}\text{O}_{1.95}$	25% / $\sim 4\mu\text{m}$	Tape-casting	[50]
Various perovskites	$0.5\text{--}3\mu\text{m}$	ASP	Al_2O_3 coated with YSZ	300kDa / $0.2, 0.6\mu\text{m}$	Purchased	[51]
$\text{La}_{0.58}\text{Sr}_{0.4}\text{Co}_{0.2}\text{Fe}_{0.8}\text{O}_3$	10- $20\mu\text{m}$	VSC, SP	Co-promoted CGO, LSCF or composite	36-57% / $0.7\mu\text{m}$	Warm-pressing	[52]
$\text{La}_{0.2}\text{Sr}_{0.8}\text{Fe}_{0.8}\text{Ta}_{0.2}\text{O}_3$	15- $60\mu\text{m}$	CS Dip coating	$\text{La}_{0.2}\text{Sr}_{0.8}\text{Fe}_{0.8}\text{Ta}_{0.2}\text{O}_3$		Uni-axial Pressing	[53]
$\text{La}_{0.8}\text{Sr}_{0.2}\text{Fe}_{0.7}\text{Ga}_{0.3}\text{O}_3$	$80\mu\text{m}$	TCL and co-firing	$\text{La}_{0.8}\text{Sr}_{0.2}\text{FeO}_3$ or $\text{La}_{0.8}\text{Ba}_{0.2}\text{FeO}_3$		Tape-casting	[54]
$\text{Ba}_{0.5}\text{Sr}_{0.5}\text{Co}_{0.8}\text{Fe}_{0.2}\text{O}_3$	$70\mu\text{m}$	TCL and co-firing	$\text{Ba}_{0.5}\text{Sr}_{0.5}\text{Co}_{0.8}\text{Fe}_{0.2}\text{O}_3$		Tape-casting	[55]

Th.: Thickness, P.: Porosity, D.: pore diameter, SG: Sol-gel, UVSG: UV assisted sol-gel, ESD: Electrostatic spray deposition, TCL: Tape-casting lamination, ASP: atmospheric spray pyrolysis, VSC: vacuum-slip-casting, SP: screen-printing, CS: colloidal suspension

2.3 Wet chemical deposition

2.3.1 Stabilization of dispersion

There are two fundamental mechanisms that control the dispersion stability, e.g. electrostatic stabilization and steric stabilization as shown in **Figure 7**.

1. *Electrostatic stabilization*: Based on DLVO theory (Derjaguin & Landau [56] and Verwey & Overbeek [57]), the important factor determining the stability of colloidal system is the summation of van der Waals (attractive energy) and electric double layer (repulsion energy) interactions. When particles are submerged in an electrolyte, a second layer of charges with opposite sign (counter ions) forms on the first layer possessing the same sign as the wall charges (co-ions), which was called the electric double layer (EDL) by Stern [58]. The EDL creates a potential known as surface potential and it decrease with moving away from the surface. The surface potential can be estimated by zeta-potential at a plane where the shear starts (shear plane). The zeta-potential is strongly dependent on pH value. There is a pH value for “zeta-potential=zero”, i.e. isoelectric point (IEP) and thus the particles aggregate intensely. The dispersion becomes usually more stable when absolute value of zeta-potential increases.
2. *Steric stabilization*: organic macromolecules or polymers, which adsorb on the particle surface and have good solubility in the solvent, are added to the dispersion. When the particle surfaces with polymer coating come together, the polymer layers are forced to penetrate into each other. Due to the increase in segment density, the freedom of movement of the polymer chains are removed (sudden drop in entropy). This is not a physically favourable process, so the particles cannot come closer than roughly twice the layer thickness. If the layer thickness is larger than the range of the van der Waals interaction, then it will act as an effective barrier, by preventing the coagulation, called steric stabilization [59, 60].

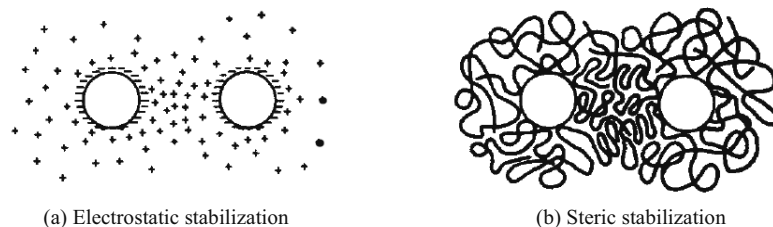


Figure 7 Schematic drawing of stabilizing particles [61].

2.3.2 Spin-/dip-coating

The coating behaviour and final film thickness depend on the nature of the coating solution, e.g. density, viscosity, drying rate, solids concentration in the coating solution, surface tension etc. The ratio of particle size of solids in coating solution (d_{particle}) and pore size of porous substrate (d_{pore}) plays an important role, when the porous substrate is used. Particularly if the d_{particle} is much smaller than d_{pore} , the coating solution is infiltrated into the substrate pores and cannot form any films on the porous substrate successfully. Moreover, the support parameters such as porosity, surface roughness, wetting behaviour determine the properties of coating layer.

Spin-coating

Spin coating is one of the standard methods for depositing sol onto flat substrates, forming thin films rapidly. The substrate is held by rotatable vacuum chuck and the coating solution is dispensed onto the substrate surface. The vacuum chuck is spun up and centripetal force causes the coating solution to spread out and leave a relatively uniform coating layer on the substrate surface. After spin-off the remaining coating layer undergoes evaporation (drying). The process parameter of spin-coating such as spinning acceleration, final spin speed, and spin time can contribute to the properties of coating layers.

In 1958 Emslie, Bonner and Peck (EBP) [62] proposed a simple model of the spin-coating process predicting film thickness as shown in **Equation 10**, where h_o is the initial film thickness, ω is the rotation speed and η is the viscosity. It was assumed that flow has reached a stable condition where the centrifugal and viscous forces are just in balance.

$$h = h_o \left(1 + \frac{4\omega^2 h_o^2 t}{3\eta} \right)^{-\frac{1}{2}} \quad \text{Equation 10}$$

Based on the EBP model, Meyerhofer [63] has described a model with the addition of the evaporation of the solvent. At longer times, solvent evaporation becomes an important contribution. He split the spin-coating run into two stages, i.e. one controlled by viscous flow and the other controlled only by evaporation, predicting the final coating thickness, h_f , as a function of a number of physical parameters as follows:

$$h_f = x \left[\frac{e}{2(1-x)K} \right]^{1/3} \quad \text{Equation 11}$$

where x is the solids concentration in the solution, and e and K are the evaporation and flow constants, respectively, defined as follows:

$$e = C\sqrt{\omega} \quad \text{and} \quad K = \frac{\rho\omega^2}{3\eta} \quad \text{Equation 12}$$

2. Fundamentals and background

where ω is the rotation rate, ρ is the density of solution, η is the viscosity of solution, and C is a proportionality constant that must be determined for the specific experimental conditions.

The equations were derived for spin-coating on dense substrate. For using porous substrates, additional factors such as porosity and pore size of substrate should be further considered.

Dip-coating

Dip-coating is one of the most fundamentally important coating processes for membrane manufacturing. Thin films manufactured by dip-coating represent the oldest commercial application of sol-gel technology. Dip-coating process involves 4 steps, i.e. dip-in of the substrate into the coating solution, immersion (dipping) for certain time, dip-out of the substrate from the coating solution, and evaporation (drying). There are two possible compaction modes of coating layer during dip-coating when a porous substrate is used, i.e. capillary filtration and film-coating [44]. The important parameters of both modes were summarized in **Table 3**.

Capillary filtration mode: when the dry substrate comes into contact with the coating solution, the solvent is absorbed into the substrate by capillary action of substrate pores and the particles are concentrated on the substrate surface, forming compact layer which thickness increases with contact time until stationary state.

Film-coating mode: During dip-out the thin film can form from the dragging effect of the substrate and the adhesion of the coating solution on the substrate. In this mode, the contact time of substrate is not considerable. The coating thickness increases with increasing dip-out speed and increasing viscosity of coating solution.

Table 3 Important parameters of two possible compaction modes during dip-coating when a porous substrate is used [44].

Capillary colloidal filtration	Film-coating
Suspension	Suspension
- Volume fraction of solids	- Viscosity
- Agglomerate size distribution	- Yield value
- Viscosity	- Density
	- Surface tension
Support	Support
- Porosity	- Porosity
- Pore size distribution	- Surface roughness
- Capillary action	- Radius
	- Wetting
Immersion time (Dipping time)	Dip-out speed
Particle size/pore size ratio	

The dip-coating process can be divided into horizontal and vertical coating processes, enabling both side and one side of substrate to be coated, respectively (See Figure 8).

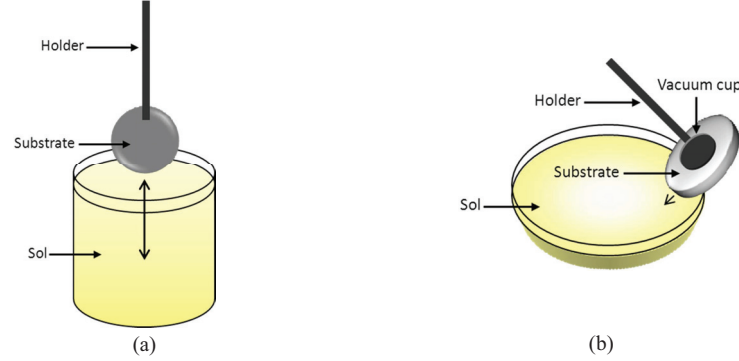


Figure 8 Schematic illustration of vertical (a) and horizontal (b) dip-coating process.

In the case of *vertical* dip-coating, the coating thickness (h_0) is mainly defined by coating process parameter (i.e. dip-out speed) and by coating solution parameters (i.e. density, viscosity and liquid-vapour surface tension) and can be calculated according to the relationship derived by Landau and Levich [64] as follows:

$$h_0 = 0.94 \frac{(\eta \cdot v)^{2/3}}{\gamma_{LV}^{1/6} (\rho \cdot g)^{1/2}}$$

Equation 13

where 0.94 is a constant for Newtonian liquids, η is the viscosity of solution, v is the dip-out speed (withdrawal speed), γ_{LV} is the liquid-vapor surface tension, ρ is the density of solution and g is the acceleration of gravity. This equation is valid when dip-out speed and viscosity are low and indicate that coating thickness increases with the dip-out speed.

In the case of *horizontal* dip-coating, capillary filtration dominates. The coating thickness (L_0) increase linearly as a function of the square root of dipping time (t) [65, 66] and defined as follow:

$$L_0 = \frac{2\gamma \cos \beta}{\eta} C(t)^{1/2} + L_a$$

Equation 14

where γ is the surface tension (N/m), β is the contact angle between the coating solution and the substrate surface, C is a constant, η is the viscosity of the coating solution, and L_a is the adhering layer thickness.

Drying of coating layer

Drying of the coating layer on the substrate can be divided to two steps. The first step is so-called constant drying rate period (CRP) and following second step is falling rate period [67]. During drying period, the coating layer shrinks in volume. When the coating layer is attached to the substrate surface, shrinkage does not occur in the parallel direction of the substrate surface but rather the volume of the coating layer is reduced by decreasing thickness of coating layer. With the gradual solidification of the coating layer tensile stress develop in the plane of the coating layer, which can cause crack propagation. This stress (σ) is estimated by Croll [68] as follow:

$$\sigma = [E/(1-\nu)][(f_s - f_t)/3]$$

Equation 15

2. Fundamentals and background

where E is the Yong's modulus, ν is the Poisons's ratio, f_s is the volume fraction of the solvent at the solidification point, and f_r is the volume fraction of the residual solvent in dried coating layer. This stress in the coating layer is nearly equal to the tension in the liquid that is the capillary pressure P_c (possibly exceed 1000 bar) created by the curvature of the menisci in the pores of the substrate. Below a critical layer thickness (h_c) cracks do not occur, commonly $h_c \approx 0.5 \sim 1 \mu\text{m}$ [67]. The critical layer thickness for crack propagation for the coating layer exhibiting the good adhesion to the substrate is given as follws [69]:

$$h_c = (K_{Ic}/\sigma\Omega)^2 \quad \text{Equation 16}$$

where K_{Ic} is the fracture toughness, σ is the stress in film, and Ω is a function that depends on the ratio of the elastic modulus of the coating layer and the substrate (for gel-like layer $\Omega \approx 1$).

2.3.3 Heat treatment of coating layer

The heat treatment of coating layer including calcination and sintering steps is normally necessary to obtain the desired final ceramic layer, e.g. microstructural, mechanical and chemical stable ceramic membrane layer. The calcination step corresponds to the combustion of the organic additives and the transformation of strongly hydrated amorphous gel particles to more crystalline, mainly dehydrated particles. The sintering step allows the densification and grain growth of ceramic, corresponding to a reduction of surface free energy. Depending on the temperature and the time of sintering, the density (or porosity), pore diameter and mechanical resistance can be controlled. Moreover, with the smaller particles the densification becomes more rapidly [70, 71]. The sintering of particles was described as a diffusion of vacancies including grain-boundary diffusion, volume diffusion and viscous flow, which lead neck growth by mass transport mechanisms and permit shrinkage by pore removal [72, 73].

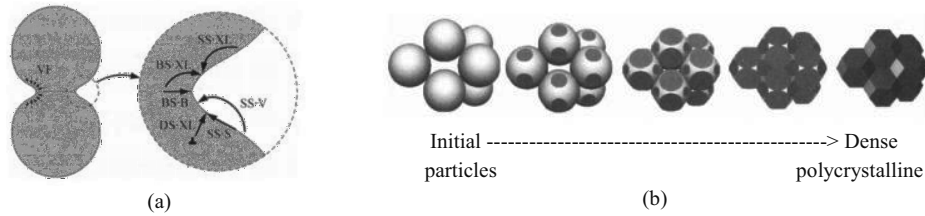


Figure 9 Two spherical particles model of neck growth by mass transport mechanisms for sintering (a) and stages of sintering (b) [73].

For supported membrane layer, the most considered factor of heat treatment is the thermal expansion behaviour between coating layer and substrate, and then the factors such as interaction and chemical compatibility between coating layer and substrate follow it. The difference in thermal expansion coefficient of substrate (α_s) and coating layer (α_L) generates stress (σ) which can cause the cracks. The stress can be defined as $\sigma = (\alpha_s - \alpha_L)E_L\Delta T$, where E_L is young modulus of coating layer and ΔT is temperature variation. The multilayer structure can be obtained by repeating the coating procedure, usually including the heat treatment step.

2.4 Physical vapour deposition

2.4.1 DC-Sputtering

DC-sputtering device essentially consists of the power supply that is simply a high-voltage DC source (supplying several kilovolts), sputtering target that is the cathode of the discharge and the anode that may be the substrate and/or the vacuum chamber walls [74].

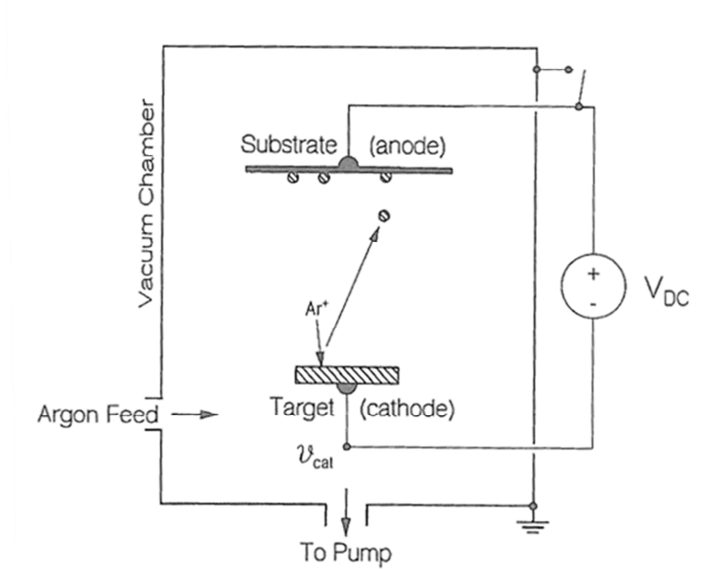


Figure 10 Schematic illustration of DC sputtering device [74].

Argon is commonly used as sputtering gas forming plasma. Plasma is a partially ionized gas including singly charged positive ions (Ar^+), electrons (e^-) and neutral gas particles. The Ar^+ particles are accelerated in the electric field and collide with the surface of the target, leading to the ejection of target atoms when the kinetic energy of argon ions is greater than the atomic binding energy of target material. This phenomenon is called “Sputtering” in physics. Subsequently, the sputtered particles were delivered toward the substrate and form the thin film on it.

2.4.2 Magnetron Sputtering

In the sputtering process, the electrons (e^-) were ejected by collisions of Ar ions to the target material. There is a perpendicular electric field (E) to the target surface. If a permanent

2. Fundamentals and background

magnet is added, lines of magnetic flux (B) are created which are perpendicular to the electric field, i.e. parallel to the target surface (**Figure 11 a**). The magnetic field leads to a longer pathway of the electrons near the target surface and thus the probability to collisions with Ar ions is increased. The ion density near the target becomes higher, causing higher ion bombardment and higher sputtering rate, and the voltage can be normally reduced in magnetron sputtering. **Figure 11 b** and **c** shows an annular design which is often employed in magnetron sputtering process and the electrons drift in the $-E \times B$ direction, actually executing a cycloidal path [74, 75].

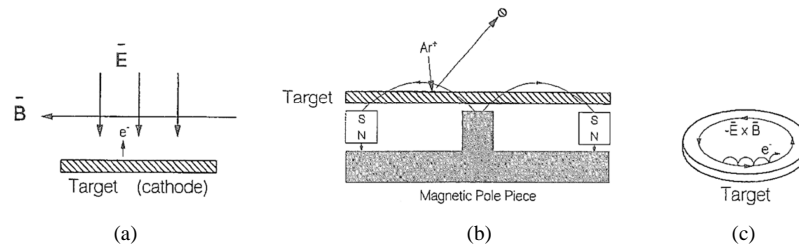


Figure 11 Schematic illustration of the magnetron effect [74].

2.4.3 Reactive sputtering

Reactive sputtering is called the sputtering process when the reactive gas (RG) is applied with inert gas (usually argon). During sputtering process in atmosphere of a mixture of argon and RG, the sputtered atoms form the compounds with the atoms of RG, such as oxides, nitrides, carbides, etc. The RG can poison the target if chemical reactions are faster than sputter rate because the target is oxidized in case of oxygen used as RG and will have much lower sputter rate (change from metallic mode to reactive mode). There is a critical point of sudden decrease in the sputter rate of target when RG flow rate entering into the deposition chamber increases [76]. It is possible to avoid this problem with a high sputtering rate, e.g. applying magnetron sputtering, and with adjusting the availability of the reactive gas that can react sufficiently to deposit the desired compound but not so much to poison the target surface [75]. In this work, the oxygen is supplied as RG near the substrate and thus the oxidation will not occur near the target. Therefore, few oxygen atoms can reach the target surface and form oxide monolayer that is subsequently removed by the sputtering process.

2.4.4 Film Morphology

The properties of deposited thin films, such as permeability, depend on their microstructure. Therefore, in order to obtain the desired properties of deposited thin films it is very important to adjust the deposition parameters which lead to the desired microstructure. According to Thornton structure zone model [77], the microstructure is strongly influenced by substrate temperature and argon pressure in the sputtering chamber (Figure 12), which was extended

from the three structure zone concept of Movchan and Demchishin [78]. According to the ratio of substrate temperature (T) and melting point of target material (T_m), the zone can be divided individually as described in **Table 4**.

Table 4 Microstructure description of Thornton zone model.

Zone nr.	Microstructure description
Zone 1:	Porous structure due to the poor surface mobility at low temperature.
Zone T: (Transition zone)	Densely packed fibrous grains with smooth surface resulted from higher surface mobility at higher temperature.
Zone 2:	Dense columnar grains with rough surface from increase in surface mobility.
Zone 3:	Larger non-columnar grains from further increase in surface mobility, which can be good for diffusion barriers, i.e. less grain boundary diffusion due to fewer grains.

When the substrate temperature increases, the sputtered atoms on the substrate surface have sufficient kinetic energy and thus the surface mobility of the atoms (movement of atoms on the surface) also increase to reach positions of a lower potential energy. The deposition rate has similar effect. If proper deposition rates are applied (i.e. not too high deposition rates), the sputtered atoms have enough time to move to the positions of a lower potential energy before being covered by other atoms. The zone boundaries can be shifted to the higher substrate temperature range at higher argon pressures.

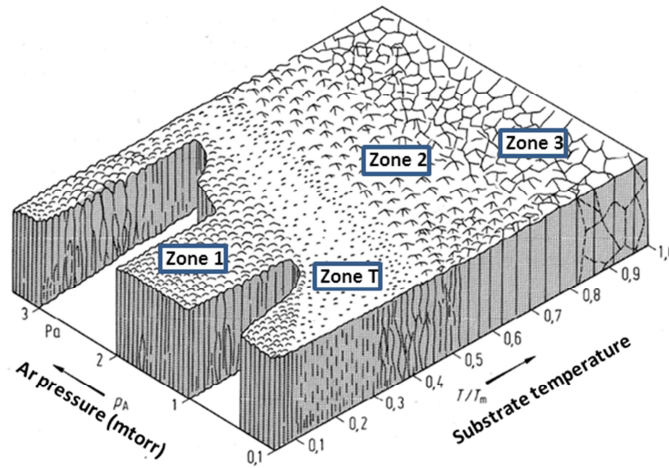


Figure 12 Thornton structure zone model: dependence of coating structure on substrate temperature and argon pressure [77].

3 Experimental methods

3.1 Ceramic substrate preparation

To ensure mechanical stability thin membranes are usually supported by substrates in this work. Various ceramic substrates were manufactured via vacuum-slip-casting and warm-pressing, producing disk- and square-shaped substrates, respectively. The representative substrates are displayed in **Figure 13**. The roughness of substrates was controlled by polishing for vacuum-slip-cast substrates, and by interlayer coating for warm-pressed substrates.

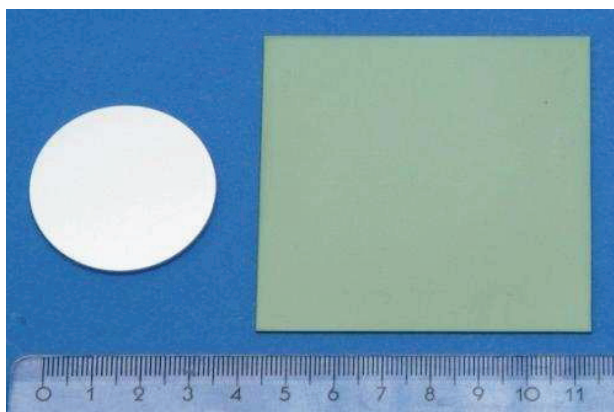


Figure 13 Photograph of prepared substrates:
via vacuum-slip-casting (left, 8YSZ) and warm-pressing (right, Coat-Mix)

Vacuum-slip-casting (8YSZ and $\alpha\text{Al}_2\text{O}_3$)

The ceramic substrates were prepared via vacuum-slip-casting using ceramic suspension, as shown in **Figure 14**. The commercial high purity powders, i.e. 8 mol% Y-ZrO₂ powder (Tosoh Corporation/ Yamaguchi Japan, TZ-8Y grade) and $\alpha\text{Al}_2\text{O}_3$ powder (Sumitomo chemical Co., Ltd./ Tokyo Japan, Type AKP-30), were mixed with 0.02M HNO₃ at weight ratio of 1:1. The mixtures were dispersed homogeneously using ultrasonic disintegrator (Branson, Sonifier 450) for 15min, and sieved to eliminate remaining agglomerates in mixtures. Subsequently, the dispersed mixtures were poured on membrane filters (Pall Corporation/ Michigan, Supor®-800, pore size 0.8 μm , Ø 47mm) laid in funnels which were connected to vacuum system. The solvent was sucked off through the filters and green bodies remained on the filters as disks.

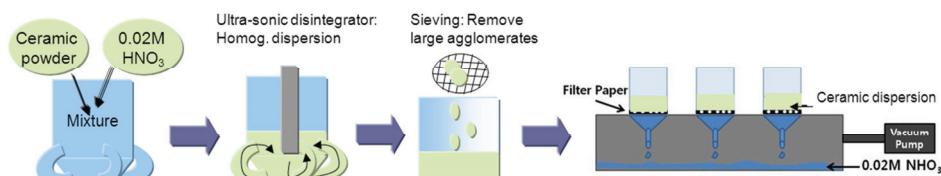


Figure 14 Ceramic substrate preparation via vacuum-slip-casting

The disks were dried over night without further evacuation and pre-sintered as following.

RT ——— 100 °C for 30 min ——— 1100 °C for 2 h ——— RT

Grinding and lapping processes were carried out for the sintered disks to obtain desired external dimensions (\varnothing 39 mm, thickness of 2.6 mm). One surface of every disk was polished very carefully with diamond pastes (6 μ m and then 3 μ m). The roughness of substrate surface is controlled in this process. Afterwards, the disks were cleaned in ultrasonic bath, which was filled with ethanol, to remove residual particles arisen during polishing process. The disks were fired for organic burnout, which was used as lubricant, as following.

RT ——— 100 °C for 30 min ——— 700 °C for 1 h ——— RT

Final thickness of the disks reached approximately 2.5 mm.

Warm-pressing with vacuum-slip-cast interlayer (WP/VSC using Coat-Mix®)

The ceramic substrates and interlayers (so-called *anode substrate* in SOFC application) were manufactured in Forschungszentrum Jülich (IEK-1) via warm-pressing and vacuum-slip-casting, respectively, using Coat-Mix® powder [79]. The powder mixture was composed of 56 wt.% Nickel(II)-oxide powder (Baker, USA) and 44 wt.% 8YSZ powder (Unitec ceramics Ltd./ Stafford UK for substrate and Tosoh Corporation/ Yamaguchi Japan, TZ-8Y grade, for interlayer). The warm-pressed substrate was pre-sintered at 1230 °C for 3h in air and vacuum-slip-cast interlayer, at 1000 °C for 1h in air, producing thickness 1500 μ m for the substrate and 5-15 μ m for the interlayer [80]. The roughness and the pore size of substrate surface were reduced with interlayer. These substrates that underwent final-sintering (1400°C 5h in air) and following reducing (900°C 3-5h in Ar/4%H₂) process yield 44 ± 1 vol. % porosity [81]. The pre-sintered substrates were cut to external dimension 40 x 40 mm for membrane coating in this work.

3.2 Membrane manufacturing

3.2.1 Manufacture of inorganic membrane by wet chemical deposition

3.2.1.1 CGO coating liquids and PVA preparation

CGO nano-dispersion

The commercially available CGO (20 mol% gadolinium doped cerium (IV) oxide) nano-powder (Aldrich) was mixed with various molarity of HNO_3 that was diluted from 1M HNO_3 (Merck Schuchardt OHG), and dispersed using ultrasonic disintegrator (Branson, Sonifier 450) for 15min. The dispersion was centrifuged with the gravity acceleration of 3500 or 6500 $\times g$ for 4 min, using high performance centrifuge (Heraeus® Biofuge® primo). The segregated particles on the bottom were removed and homogeneously dispersed solution was obtained. **Figure 15** shows the centrifuge device (a) and centrifuged CGO nano-dispersion (b). The optimum stability of nano-dispersion using initial solid concentration 4.0 wt.% was found when 0.05M HNO_3 was used in this work. Various solid concentrations of CGO nano-dispersion were prepared using 0.05M HNO_3 resulting in 1.0, 1.5, 2.5 and 4.5 wt.% after centrifugation. This CGO nano-dispersion will be simply called XNDCGO (X is the concentration of CGO in wt.%) hereafter (See **Table 5**).

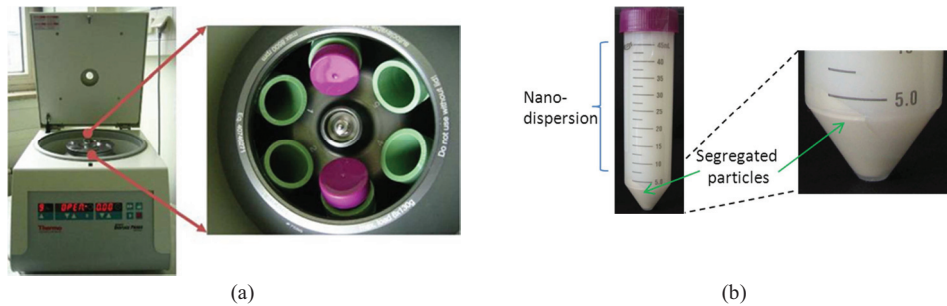


Figure 15 Photographs of centrifuge device (a) and centrifuged CGO nano-dispersion (b).

Table 5 Prepared CGO nano-dispersion (NDCGO) with 0.05M HNO_3 solvent

Sol name	1.0NDCGO	1.5NDCGO	2.5NDCGO	4.5NDCGO
wt. %	1.0 ± 0.06	1.5 ± 0.23	2.6 ± 0.13	4.4 ± 0.16

CGO colloidal sol

CS_CGO: 1.5g presursors, cerium nitrate hexahydrate ($\text{Ce}(\text{NO}_3)_3 \cdot 6\text{H}_2\text{O}$, Aldrich) and gadolinium nitrate hexahydrate ($\text{Gd}(\text{NO}_3)_3 \cdot 6\text{H}_2\text{O}$, Aldrich) at a molar ratio 4:1, were dissolved in 70 ml deionized water (Solution 1). Various amount of ammonium hydroxide solution (NH_4OH , ACS reagent, 28-30% NH_3 basis, Aldrich), i.e. 0.1, 0.2, 0.3, 0.5, 0.7 and 1.2g, was diluted with 200ml deionized water (Solution 2). The solution 2 was added to the solution 1 rapidly with strong mechanical stirring under room temperature. The use of ammonium hydroxide solution resulted in a voluminous yellowish or orange sol (or precipitation at higher concentration of $\text{NH}_3 \cdot \text{H}_2\text{O}$).

CS_AIOOH: $\text{AlO}(\text{OH})$ sol was prepared based on publications of Leenaars [82] and Benes [83]. 70 mol of deionized water was heated up to 90 °C and then 0.5 mol of Aluminium-tri-sec-butoxide (ATSB) was added with vigorous stirring. The reaction temperature was maintained at over 80 °C to avoid the formation of Bayerit ($\text{Al}(\text{OH})_3$). This mixture was further stirred at 90°C for 3 hours to evaporate the resulting butanol. Subsequently, the mixture was peptized with a 65 % HNO_3 , so that the pH value was adjusted to 2.5 at a temperature of 60 °C. The resulting sol was further stirred at 90 °C during overnight for homogenization and stabilization. Finally, the sol had a pH of about 3.5 and a concentration of 0.5 M.

PVA solution as DCCA

PVA (Polyvinyl alcohol) additive has great benefit when added into the sol, e.g. enhancing the reproducibility of the membrane formation process, reducing the defect level of the membranes and controlling the drying and calcination rates [84]. PVA solution was prepared as binder and also as DCCA (drying chemical controlling additive) for wet chemical deposition. 3g (dry weight) of PVA (Merck Schuchardt OHG, specification in **Table 6**) was added into 100ml of 0.05M nitric acid (HNO_3) in an Erlenmeyer flask and heated up to 90°C under reflux with mechanical stirring to form a ~3 % PVA solution. Heating time was selected depending on molecular weight of PVA, as shown in **Table 7**.

Table 6 Specification of purchased PVAs.

PVA no.	PVA1	PVA2	PVA3	PVA4
Molecular weight (g/mol)	approx. 22000	approx. 60000	approx. 72000	approx. 145000
Molecular fomular	$(-\text{C}_2\text{H}_4\text{O})_n$	$(\text{C}_2\text{H}_4\text{O})_n$	$(-\text{C}_2\text{H}_4\text{O})_n$	$(\text{C}_4\text{H}_6\text{O}_2 \cdot \text{C}_2\text{H}_4\text{O})_n$
Degree of hydrolysis	Calc. on anhydrous substance $\geq 98\%$	Calc. on dried substance $\geq 98\%$	Calc. on anhydrous substance $\geq 98\%$	Calc. on dried substance $\geq 98\%$
Loss on drying	(105 °C) $\leq 5\%$	(110 °C2h) $\leq 5\%$	(110 °C4h) $\sim 3\%$	(110 °C2h) $\leq 5\%$
Ash	-	$\leq 1\%$	-	$\leq 1\%$
Ester value	-	15-25	-	3-13

3. Experimental methods

Table 7 Preparation of PVA solutions with various molecular weights.

PVA no.	PVA1	PVA2	PVA3	PVA4
Molecular weight (g/mol)	approx. 22000	approx. 60000	approx. 72000	approx. 145000
Heating temperature (°C)	97	97	97	97
Heating time (h)	3	3	3	18

Final coating solution

The sols and PVAs were purified by using a 0.8 μm -syringe filters (Whatman, FP 30/0.8 CA) to remove agglomerates or potential dirt. Subsequently they were mixed together at a desired volume ratio as shown in **Table 8**.

Table 8 Volume ratio of sol : PVA for final coating solution.

Used sol	ND_CGO	CS_CGO	CS_AlOOH
Sol: PVA	3:1	3:1	3:2

3.2.1.2 Coating methods (dip- and spin-coating)

The thin film, which is interlayer or functional membrane layer as the case may be, was coated on the substrate using horizontal dip-coating or spin-coating method. To avoid potential sources creating defects, such as dust or undesired particles, the coatings were conducted in a clean room (ISO class 3). The prepared sol was poured into the clean petri dish through syringe filter (0.8 μm , Whatman, FP 30/0.8 CA) and floating matters on the sol, e.g. dust and air bubbles, were removed carefully. Directly prior to dip- or spin-coating, the substrates were blown using nitrogen gun.

Dip-coating

Dip-coater (Fa. Nima, **Figure 16a**) used in this work is constructed with a small motor equipped with gearbox and coupled holder, which rotation speed is controlled by potentiometer. During dip-coating procedure (**Figure 16b**) the substrate is fixed by vacuum cup. The constant rotation speed (8.2 deg/s) was applied for dip-in and dip-out. The dwell time during immersion in the sol was fixed as 15 seconds.

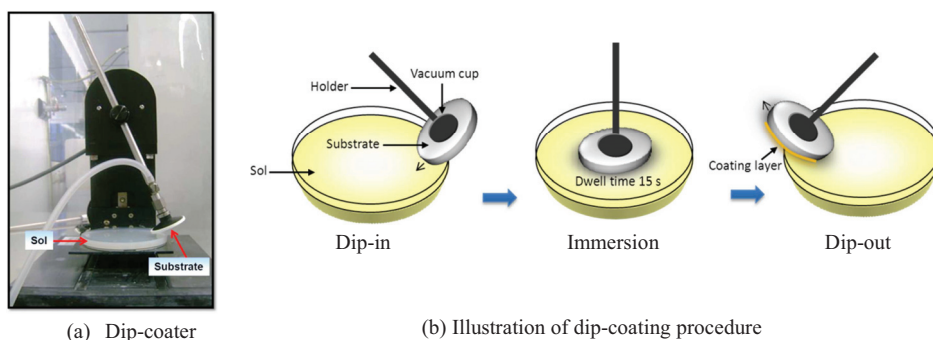


Figure 16 Horizontal dip-coating method for wet chemical deposition

Spin-coating

Membrane coating was carried out using a Spin-coater (Delta 80T2, Süss MicroTec AG, **Figure 17a**) as well, which is convenient to operate with fully programmable process parameters. Spin-coating process (**Figure 17b**) can be divided into four stages: Sol dispensation, spin-up, spinoff, and drying. Porous substrate was held on a vacuum chuck of spin-coater. Subsequently, sufficient amount of sol was dispensed on the substrate until the substrate surface is totally covered with the sol to avoid inhomogeneous coating. The parameters of spin-coating were set using a program connected with spin-coater. Spin acceleration and deceleration were fixed as 60rpm/s for all coating runs. The final rotation speed, i.e. rotation per minute (RPM or r/min), and the dwell time (sec.) at given final RPM were varied, e.g. 400, 800 and 1200 RPM for rotation speed, and 20, 40 and 60 seconds for dwell time.

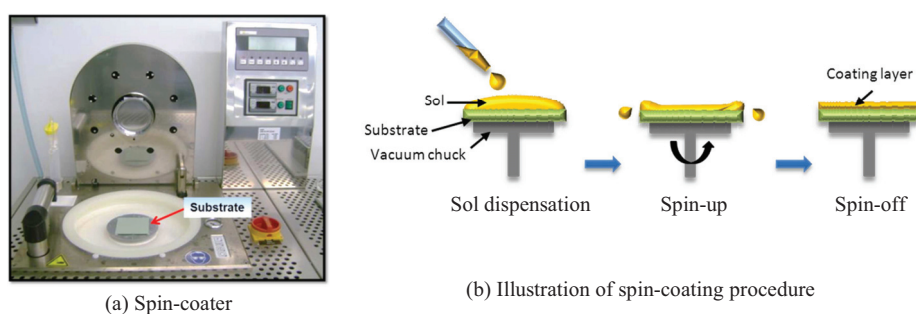


Figure 17 Spin-coating method for wet chemical deposition

3. Experimental methods

3.2.2 Manufacture of inorganic membrane by physical vapour deposition

The inorganic membrane (CGO and LSCF) coatings were carried out in a physical vapour deposition (PVD) system using a CS 400ES (Von Ardenne Anlagentechnik, Germany, **Figure 18**). This system has substrate face-down mode and consists of four vacuum chambers, i.e. transfer chamber, sputter etch chamber, evaporator chamber and sputter chamber. Sample holder can be introduced into the central transfer chamber that is connected with sputter etch chamber (ISE 200), electron beam evaporator chamber and sputter chamber with the magnetron sputtering (PPS-A 250). Each chamber is separated by chamber valves and equipped with its own booster pump and turbo pump. All processes were performed using computer-controlled software WICON 32. The samples are pretreated by an inverse sputter etching and subsequently the membrane coatings are conducted. The magnetron sputtering can be operated using DC or RF mode having a maximum power 3kW. This work focuses on the DC magnetron sputtering of CGO and LSCF membranes.

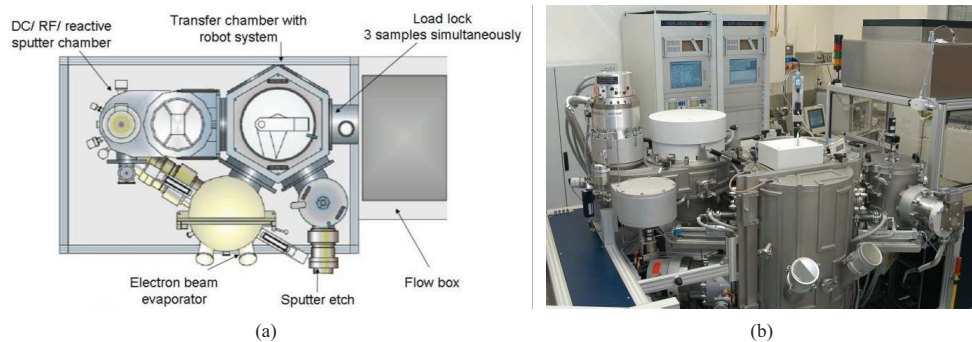


Figure 18 Principle design (a) and facility in IEK-1/FZJ (b) of cluster system CS400 ES (Von Ardenne Anlagentechnik GmbH)

Sample cleaning

Sample cleaning is very important process for good adhesive layer formation as investigated by Jordán Escalona [85]. Impurities on the substrate surface would have hindered the necessary contact and adhesion between substrate and depositing layer. Two cleaning processes were done in this work. In the first cleaning, the samples were ultrasonically cleaned in a container filled with ethanol. This step removed the dirt of samples such as fat and dust. After drying, the second cleaning was carried out in the PVD facility. The samples were placed on the sample holder and moved into the transfer chamber. After evacuation, the samples further moved into the sputter etch chamber and underwent sputter etching, so-called plasma cleaning, with 200W for 10 minutes. The sample surface was physically cleaned by ion bombardment, i.e. particles on the sample surface were removed. The plasma is stimulated by the high-frequency alternating current (AC) voltage (13.56 MHz and 1 kW) using a RF

Generator PFG 100 RF (Hüttinger Elektronik GmbH). Argon gas was used as process gas for plasma cleaning. To achieve a uniform cleaning, the substrate was rotated along the axis perpendicular to the surface plane of the sample by a motor at a constant speed.

DC magnetron sputtering

Figure 19 shows a schematic drawing of the magnetron sputter chamber where the CGO and LSCF membrane deposition processes are performed. The sputter chamber was evacuated by a booster pump and a turbo pump to below 5×10^{-7} mbar. An electric field is generated using a DC generator (PFG 3000 DC, max 3 kW, Hüttinger Elektronik GmbH), which ionizes the argon atoms and thus creates the plasma. The positively charged argon ions (Ar^+) are accelerated in the electric field and collided with the target surface. The magnetron was applied to the target in sputtering process which enhances the sputter rate (See section 2.4.2). The sputtered atoms are deposited on the substrate. The oxygen was additionally introduced to the sputter chamber as reactive gas for CGO deposition due to the use of metallic target (reactive mode). For LSCF deposition, oxygen gas was applied as a background oxygen partial pressure to compensate oxygen losses from designed ceramic target during sputtering process. During the deposition, the process pressure on the chamber was kept at 6×10^{-3} mbar and DC-power was set to 500 W. The circle-shaped target has a diameter of 250 mm, which is located 55 mm far from the sample holder. 200 x 200 mm² zone on the sample holder is proposed to be a homogeneous deposited zone. The heater lying above the substrate enabled an increase of substrate temperature up to 800 °C.

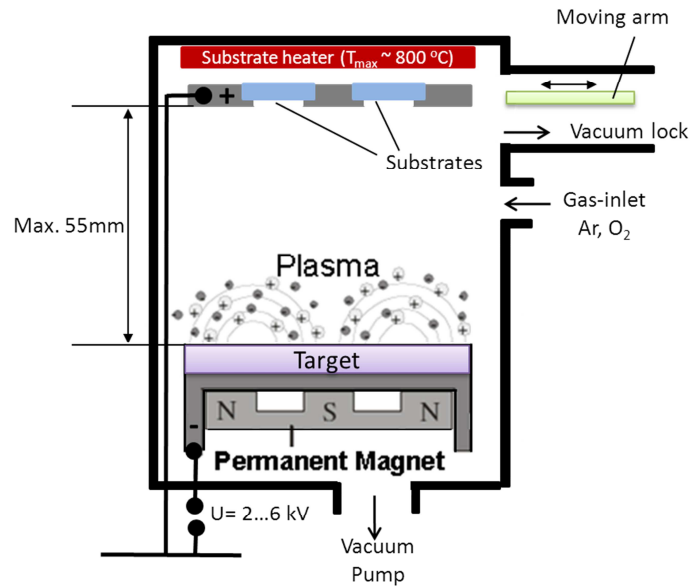


Figure 19 Schematic illustration of magnetron sputtering chamber.

3. Experimental methods

3.2.2.1 CGO deposition

Thin CGO membranes were grown by DC-reactive magnetron sputtering using 20 at.% Gd-Ce metallic alloy target (99.7% purity, MaTeck GmbH Germany) in reactive O₂/Ar gas mixtures (8 sccm oxygen and 30 sccm argon flow). The sputtered metallic alloy reacts with oxygen gas to produce their oxide layer. The substrates were used at room temperature or heated up to the substrate temperature of 800 °C at a heating and cooling rate of ± 5 Kmin⁻¹. High-frequency bias voltage was applied to the metallic (Inconel) sample holder by controlling a fixed bias power of 0, 100, 200, 300 and 400 W.

3.2.2.2 LSCF deposition

Thin LSCF membranes were grown by DC-magnetron sputtering using LSCF ceramic target that was prepared via spray pyrolysis in IEK-1/FZJ. The oxygen contained in target material is more volatile than the metallic components, which can cause an oxygen shortage in the deposition layer. Therefore, oxygen gas was additionally introduced into the sputter chamber although the LSCF target consists of oxide material. A gas mixture used for LSCF deposition was actually equivalent to that for CGO deposition, i.e. 8 sccm oxygen and 30 sccm argon flow. The substrate temperature was kept at 800 °C. The heating and cooling rate were ± 5 Kmin⁻¹. LSCF deposition was performed without applying bias voltage.

3.3 Characterization methods

3.3.1 Mercury porosimetry

Mercury porosimetry is based on the physical principle that the mercury, a non-wetting liquid for almost all materials, will not penetrate pores until sufficient pressure is applied to force the mercury into the pores of dry materials. During measurement, the applied pressure and penetrated volume of mercury are analysed. The relationship between the applied pressure (P) and the pore radius (r_p) is given by Washburn equation, the modified Laplace equation, as follows [86].

$$r_p = - \frac{2\gamma \cos\theta}{P} \quad \text{Equation 17}$$

where γ is the surface tension of mercury (usually $\gamma_{\text{Hg/air}} = 0.48 \text{ N/m}$) and θ is the contact angle between mercury and the pore wall (usually $\theta_{\text{Hg/oxide}} \approx 140^\circ$).

In this work, various quantifiable aspects of support's porous nature, such as pore diameter, total pore volume, specific surface area and bulk and apparent densities, were determined using a Pascal 440 (Fisons Instruments, Italy).

3.3.2 Zeta-potential

The degree of aggregation of metal oxide particles in a sol, based on DLVO theory (see **section 2.3.1**), is determined by the height of the potential barrier (*zeta-potential*) which results from an electrical double layer around the individual particles (see the section 2.3.1). The prepared nano-dispersions were constantly stirred with magnetic bar and the *zeta potential* of prepared nano-dispersions was measured as a function of pH using an Acoustic spectrometer DT-1200 (Dispersion Technology, Inc., USA). This setup is suitable for moderately concentrated systems. 100ml of the nano-dispersions was used for each measurement.

3.3.3 Particle size analysis

Dynamic Light Scattering (DLS) technique is one of the most popular methods used to determine the particle size distribution (PSD) of dispersed particles. Due to the Brownian motion of dispersed particles, Doppler Effect occurs in the incident light frequency. That is, when a monochromatic light beam, such as a laser, hits the moving particles, the wavelength of the incoming light is changed. This change is related to the size of particles. With

3. Experimental methods

assumption that the particles are spherical and non-interacting, the hydrodynamic particle diameter (r) is obtained by Einstein-Stokes equation as follows:

$$r = \frac{k_B \cdot T}{6 \cdot \pi \cdot \eta \cdot D} \quad \text{Equation 18}$$

where k_B is the Boltzmann's constant, T is the absolute temperature, η is the viscosity of the solvent and D is the diffusion coefficient [87].

The PSD determination of prepared sols was performed by HORIBA LB-550 (Retsch Technology GmbH, Germany) and evaluated by device-specific software (LB-550 software package). The LB-550 measures particle size from 1nm to 6 μ m and a concentration range from 1 ppm up to 40 wt. %, depending on the sample. Measurement temperature was kept at 25 °C via temperature control system.

3.3.4 Thermal analysis (TG/DTA)

Thermo-gravimetry (TG) is a thermal analysis technique which measures the weight change in a material as a function of temperature and time, investigating the decomposition behaviour in terms of timing and mass loss of total burnout of the organic in xerogel. Differential thermal analysis (DTA) is a calorimetric technique based on the comparison of the sample temperature with that of an inert reference material (α -Al₂O₃) for the proposed temperature program. The heat flow is associated with thermal transitions in a material such as melting point, glass transition temperature, crystallization etc. The temperature change is recorded depending on an endothermic or exothermic process, i.e. the sample temperature decreases when absorbing energy or increases when releasing energy. The thermal analysis of the xerogels was carried out using a STA 409 (Netsch-Gerätebau GmbH) in this work and the samples were heated from room temperature to 1000°C or 1400°C in air with heating and cooling rate ± 1 K/min.

3.3.5 X-ray diffraction (XRD)

X-ray diffraction (XRD) provides information about the crystal structure, crystalline defects, texture orientation or mechanical stresses in microscopic field. In crystals the atoms have a regular periodic arrangement of atomic distances, which is approximately equal to the wavelength of the incident X-rays. Therefore, interference occurs with the radiation emitted by neighboring atoms. In certain directions strengthening or weakening of the emitted wave fronts generates, which is so-called constructive interference (diffraction peaks) or destructive interference (diffraction minima), respectively. The relationship describing the angle at which a beam of X-rays with particular wavelength diffracts from a crystalline surface is defined by Bragg's law,

$$2d\sin\theta = n\lambda$$

Equation 19

where d is the inter-plan distance of atoms, ions or molecules, θ is the scattering angle, n is the integer representing the order of the diffraction peak, and λ is the wavelength of the X-ray. From the measured pattern, the crystal structure of the investigated sample region can be determined using JCPDS (Joint Committee on Powder Diffraction Standards) comparison.

X-ray diffraction measurements were performed using a Siemens D5000 diffractometer (Siemens AG, Karlsruhe, Germany) with $\text{CuK}\alpha$ ($\lambda=1.54\text{\AA}$) radiation with a diffraction angle (θ) range of 20° to 80° to examine the crystal structure of sintered sols and deposited membrane layers.

3.3.6 Chemical analysis (ICP-OES)

ICP-OES (Inductively Coupled Plasma with Optical Emission Spectroscopy) is one of the most useful analytical tools for qualitative and quantitative multi-element analysis. The ICP source produces plasma (temperature to 10,000 K), which is a stream of high-energy ionised gas by inductively coupling an inert gas such as argon with a high-frequency field. When the sample in solution is transported into the plasma by carrier gas, the atoms of the sample are thereby excited and fall back into their ground state again emitting a characteristic radiation. The spectrum emitted is transferred into a spectrometer (OES) where it is decomposed into the individual wavelengths and evaluated. The results in emission of light with unique frequencies make the qualitative analysis of materials possible. The light intensities are proportional to the concentration of the elements in sample, yielding quantitative analysis. The intensities were identified by detector and evaluated (TJA-IRIS-INTREPID: Spectrometer with Echelle optics and CID semiconductor detector).

In this work, the acid digestion was employed for the sample preparation of powder and film material, as following **Table 9**. Materials were dissolved in acid solution and the solution was further filled up for ICP-OES measurement.

Table 9 Acid digestion for the sample preparation of ICP-OES

Material	CGO	CGO	LSCF	LSCF	LSCF
Form	Powder	Powder	Powder	Film/ Si wafer	Film/ 8YSZ
Fabrication	Nano-dispersion, calcined	Colloidal sol, calcined	Spray Pyrolysis	Magnetron sputtering	Magnetron sputtering
Measured amount	50 mg	50 mg	100 mg	-	-
Acid solution	3ml HNO_3 / 1 ml H_2O_2	3ml HNO_3 / 1 ml H_2O_2	3ml HCl / 2ml H_2O_2	6ml HCl / 4ml H_2O_2	3ml HCl / 1ml H_2O_2
Acid filled up to	25 ml	25 ml	50 ml	25 ml	25 ml

3.3.7 Microscopy

Confocal Laser Microscope (CLM)

Confocal Laser Microscope (CLM) performs non-contact surface characterization and sub-micron roughness measurement. Conventional optics allows all of the reflected light into the photoreceptor. However, confocal laser optics uses a pinhole placed in front of the photoreceptor to ensure that no light other than that which passes through the focal point of the objective lens reaches the photoreceptor (See **Figure 20**). Thus, CLM creates significantly better contrast than a conventional optical microscope. Changes in the focal point can be measured and used as height information. In this work, sample surface was characterized using a VK-9700K (KEYENCE Corporation) that combines the confocal laser optics with a high-speed X-Y scanner to create a high resolution focal image and gather height information from the sample surface.

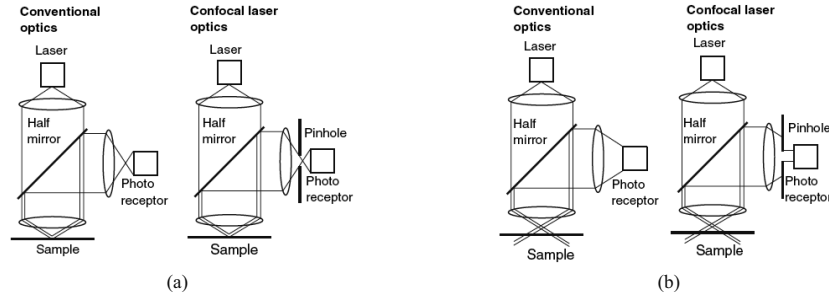


Figure 20 Schematic illustration of principle of conventional and confocal laser optics when the laser is in focus (a) and out of focus (b) [88].

Scanning Electron Microscope (SEM)

The principle of scanning electron microscope (SEM) is based on the line-by-line scanning of the sample surface using a focused electron beam. The electrons emitted from a thermionic, Schottky or field-emission cathode are accelerated down the evacuated column. There are three separate electrical parts of the gun, e.g. the tungsten filament that emits electrons, the Wehnelt cylinder that controls the number of electrons leaving the gun, and the anode that accelerates the electrons to a voltage selectable from 0.1 keV to 50 keV. The electron beam is demagnified by a two- or three-stage electron lens system to a small spot size of 1-10 nm (diameter of final beam), carrying a current of $10^{-9} - 10^{-12}$ A, at the sample surface [89].

If the high-energy electron beam strikes the sample surface, secondary electrons and backscattered electrons are generated within the primary beam-sample interactive volume, which are the two principal signals used to form images. The secondary electrons are emitted from the sample surface by the primary electrons of incident beam due to the interaction with the atoms of the sample. Due to their low energy, only those electrons that originate within a few nanometers of the surface are able to escape and thus represent the sample topography.

The backscattered electrons are the primary electrons of incident beam being deflected through an angle greater than 90° and emerged from the sample surface. The fraction of the backscattered electrons is known as the backscattering coefficient (η) that increases with increasing atomic number (Z) of the sample material because of the increasing probability of high-angle deflection with increasing Z . Consequently, heavy elements (high Z) lead to a strong backscatter and appear as light areas on the image, while light elements (low Z) produce darker areas on the image. Therefore, the backscattered electron image also known as material contrast image and allows conclusions with respect to different chemical phases on the sample surface [89, 90].

In this work, surface morphologies as well as the fracture surface of supported membranes were obtained from both FEG-SEM (field emission gun scanning electron microscope, Zeiss Ultra55) and SEM (Hitachi TM-3000) using both secondary and backscattered electrons. For sample preparation, the supported membranes were broken with pliers and reduced to a size of about $10 \times 10 \text{ mm}^2$. As occasion demands, platinum was coated on the sample with coating thickness approx. 2 nm to prevent electron charging during SEM investigation.

3.3.8 Gas-tightness measurement

Single gas (N_2 or He) permeation test

The gas permeability of various substrates and supported coating layers was examined by single gas permeation test. The gas flow rate was measured depending on pressure differentials at room temperature. The gas permeability was calculated using obtained value of gas flow rate (ml/min). In this work He (Helium 5.6, Praxair) and N_2 (Nitrogen 5.0, Praxair) gases were employed. **Figure 21** shows the schematic set-up of single gas permeation tester and photograph of testing module. The feed pressure is regulated from 0 to 5 bar by pressure controller (Brooks, 5866 series). The trans-membrane pressure differential results from the difference in pressure between the feed side and the permeate side. The permeate gas was released at atmospheric pressure (1 bar), i.e. *Pressure differential = Pressure on the feed side – 1*. The gas flow was monitored by three Flow meters (Smart Mass Flow Meter, Brooks, maximum flow: 40 ml/min for *Flow meter 1 and 2*, and 8 ml/min for *Flow meter 3*) and recorded and evaluated in computer connected with Flow meters. The gas line on the feed side was cleaned by purging prior to the test using measuring gas. The sample was located between two round steel plates of module and supported coating layer faces the feed side. Both sides of sample were packed tightly with the plates of module using O-rings (FKM 80, dimension $\varnothing 20.29 \text{ mm} \times 2.62 \text{ mm}$). Bypass line can monitor the abnormal permeate gas flow that may be usually caused by a broken sample or faulty sealing rings, and is closed during measurement. The accuracy of flow meter is $\pm 0.5 \%$ of the actual measured value with $\pm 0.1 \%$ of upper range value (40ml/min).

3. Experimental methods

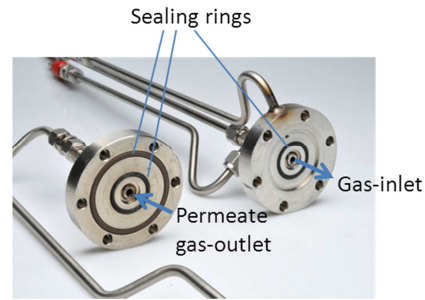
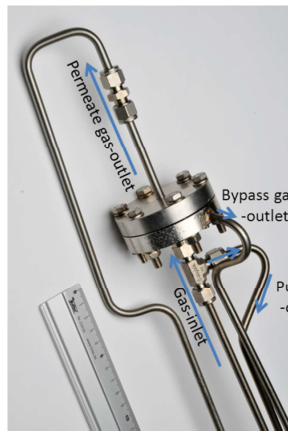
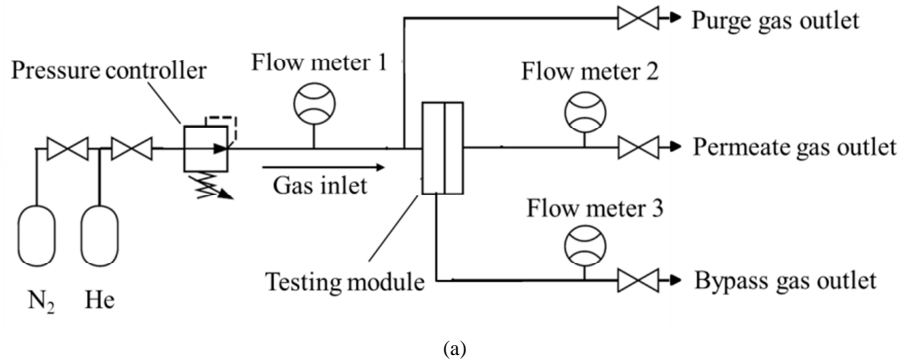


Figure 21 Schematic set-up of single gas permeation tester (a) and photograph of testing module (b-outside look, c-inside look).

He leak test

The gas-tightness of membranes can be evaluated by He-leak test. He leak rate is the amount of helium gas passing through a leak in a period of time and depends on the pressure differential as well as the size and geometry of the leak path. He leak rate are given in units of “pressure (p) · volume (v) / time (t)” such as mbar·l/sec. Helium is added to one side of sample, and a vacuum is drawn to the other side of the sample (see **Figure 22**). The container is pumped as long as a constant pressure p is set using two vacuum pumps. In this equilibrium, He-flow was measured by using a He-leak detector (Qualytest HTL 260, Pfeiffer Vacuum GmbH, Asslar, Germany). He-leak rate (R) is calculated from the measuring area of the sample (A). He-leak rate nominated by A is given as follows:

$$R = \frac{1}{A} \cdot \frac{p \cdot \Delta v}{\Delta t} \quad \left[\frac{\text{mbar} \cdot \text{l}}{\text{cm}^2 \cdot \text{s}} \right]$$

Equation 20

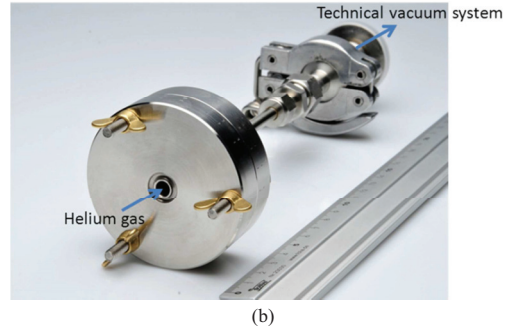
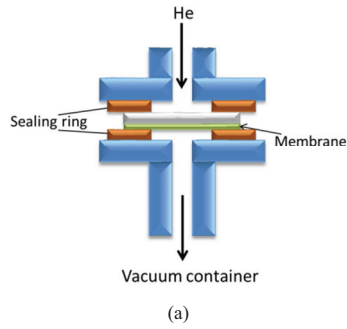


Figure 22 Schematic set-up of He-leak tester (a) and photograph of testing module (b).

4 Results and discussion

4.1 Substrates

Particle size distribution of 8YSZ and $\alpha\text{Al}_2\text{O}_3$ powders

PSD measurement was carried out in IEK-1/FZJ for commercially available 8YSZ (Tosoh) and $\alpha\text{Al}_2\text{O}_3$ (Sumitomo) powders, which were used as substrate materials of this work. The particle size and distribution measured is shown in **Figure 23**. The particle size d_{50} was 630 nm and 710 nm for 8YSZ and $\alpha\text{Al}_2\text{O}_3$ powders, respectively. In fact, this particle size represents the effective particle size of aggregates. The primary particles based on FEG-SEM images are much smaller, e.g. 100 ~ 200nm in diameter of 8YSZ and 200 ~ 300nm in diameter of $\alpha\text{Al}_2\text{O}_3$ when both were sintered at 1100 °C for 2h in air (see **Figure 24**).

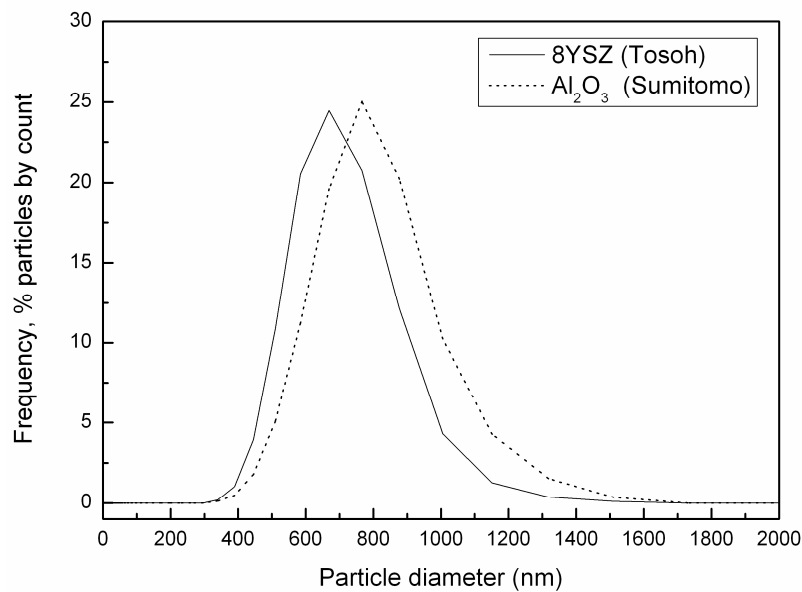


Figure 23 Particle size distribution of 8YSZ and $\alpha\text{Al}_2\text{O}_3$ powder by using Horiba LA-950V2. 0.5~1.0g of powders were dispersed in 290 ml ethanol for the measurement.

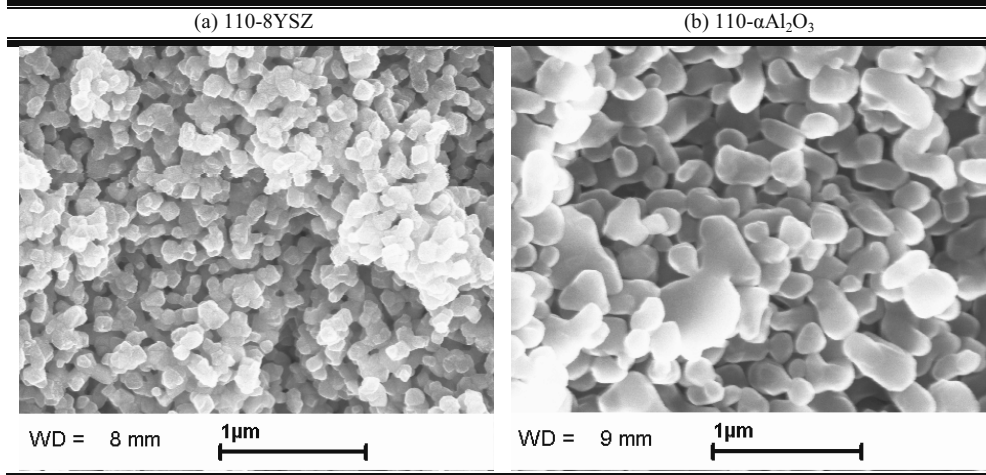


Figure 24 FEG-SEM images: fracture surfaces of porous substrates which were pre-sintered at 1100 °C for 2h.

Hg-porosimetry for sintered 8YSZ and $\alpha\text{Al}_2\text{O}_3$ substrates

8YSZ and $\alpha\text{Al}_2\text{O}_3$ substrates were prepared via vacuum-slip-casting (see the details in [section 3.1](#)). They were presintered at 1100 °C for 2h in air and these substrates were simply labelled as 110-8YSZ and 110- $\alpha\text{Al}_2\text{O}_3$. In addition, with increasing the presintering temperature 8YSZ substrates were called 114-8YSZ, 118-8YSZ and 122-8YSZ for the temperatures 1140, 1180 and 1220 °C, respectively.

Table 10 shows the results of mercury porosimetry measurement. In case of the substrates pre-sintered at 1100 °C, 110-8YSZ substrate has much higher porosity (55.6 %) than 110- $\alpha\text{Al}_2\text{O}_3$ substrate (30.09%). This higher porosity allows higher gas flow through the substrate and it agrees to the results of the gas permeation test for the substrates which is reported later in this section (**Figure 27**). When the pre-sintering temperature was elevated, the porosity was decreased gradually. Consequently, the densities (*bulk density*: mass per unit of volume, whereby closed pores and open pores are included in the volume, and *apparent density*: mass per unit of volume, whereby closed pores are included and open pores are excluded in the volume) were steadily increased.

Table 10 Results of mercury porosimetry measurement for pre-sintered substrates.

	Total cumulative volume (mm ³ /g)	Total specific surface area (m ² /g)	Total porosity (%)	Bulk density (g/cm ³)	Apparent density (g/cm ³)
110- $\alpha\text{Al}_2\text{O}_3$	101.5	4.9	30.1	2.96	4.24
110-8YSZ	146.3	5.9	55.6	3.12	5.72
114-8YSZ	129.3	4.6	49.1	3.80	7.46
118-8YSZ	99.9	3.8	46.4	4.64	8.66
122-8YSZ	68.5	2.3	39.7	5.79	9.60

Surface roughness of sintered substrates

The surface roughness of the substrate plays a significant role because it influences on many factors, e.g. coating behavior and microstructure of coating layer. Surface roughness of all prepared substrates was mapped by a confocal laser microscope. The surface roughness of images was evaluated and summarized R_a data is depicted graphically in **Figure 25**. The roughness of WP/VSC (Coatmix) substrates (R_a 0.5 – 1.1 μm) is much higher than that of 8YSZ and $\alpha\text{Al}_2\text{O}_3$ substrates. 8YSZ and $\alpha\text{Al}_2\text{O}_3$ substrates have R_a range 0.2 – 0.27 μm and R_a 0.3 μm , respectively. The surface images were displayed in **Figure 26**. As expected, 8YSZ and $\alpha\text{Al}_2\text{O}_3$ substrates show very flat surface mainly due to the surface polish, and many valleys were observed in the WP/VSC substrates.

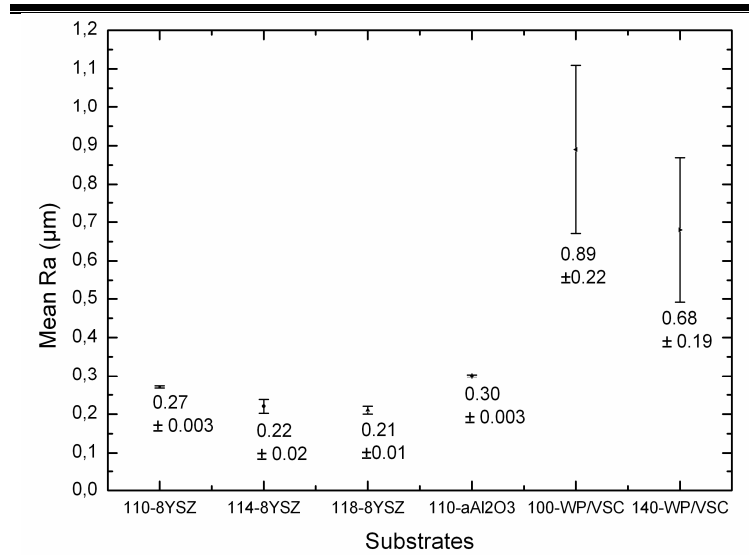


Figure 25 Surface roughness (mean R_a) of substrates evaluated using VK Analyzer (v. 2.4.0.0, KEYENCE Corporation).

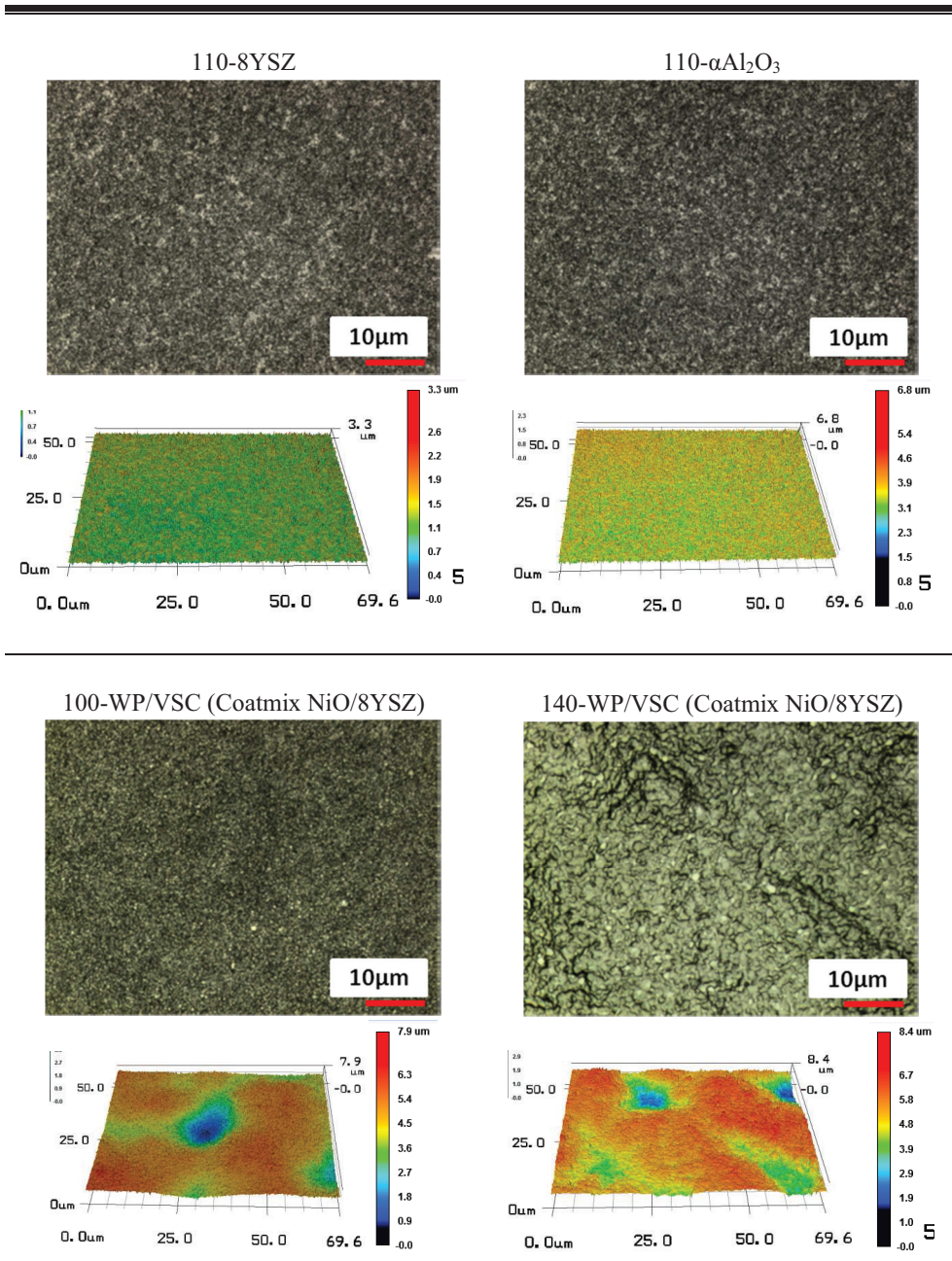


Figure 26 Substrate surface characterization by confocal laser microscope. 'Laser+color' and 'height' imeages were displayed for each substrate.

4. Results and discussion

Gas permeability of substrates

The substrate is essential for thin membranes to give the necessary mechanical stability in the entire system. However, the delivering feed gas to the membrane should not be hindered by substrate. It means that not only mechanical stability but also the sufficiently high permeability should be fulfilled for the substrate at the same time.

Gas permeability depending on the substrate material

Figure 27 shows the gas permeability of 110-8YSZ and 110- $\alpha\text{Al}_2\text{O}_3$ substrates (a) and the gas permeability of 140-WP/VSC and reduced 140-WP/VSC substrates (b). One side of 110-8YSZ and 110- $\alpha\text{Al}_2\text{O}_3$ substrate was well-polished to supply comparable surface roughness to that of the substrate with membrane coating. The gas permeation test was carried out using nitrogen and helium, respectively. The amount of gas flowing through substrates was measured as a function of pressure differential between applying pressure and atmosphere (1 bar). Four 110-8YSZ substrates and three 110- $\alpha\text{Al}_2\text{O}_3$ substrates were used for measurement. The 110-8YSZ substrates exhibited the gas permeability 2.2 ~ 2.7-fold higher than that of 110- $\alpha\text{Al}_2\text{O}_3$ substrates for both nitrogen and helium. 100-WP/VSC substrate consists of NiO/8YSZ composite, as described in **section 3.1**, which vacuum-slip-cast interlayer was pre-sintered at 1000°C for 1h in air. After sintering at 1400 °C for 5h in air, the WP/VSC substrate became dense (namely 140-WP/VSC), so it was difficult for both helium and nitrogen to flow through the 140-WP/VSC substrate. When the 140-WP/VSC substrate underwent heat-treatment at 900 °C for 3h under reducing atmosphere using Ar/4%H₂, the gas permeability increased considerably owing to the reduction of NiO to Ni. The reduced 140-WP/VSC substrates possess much higher gas permeability than 110-8YSZ and 110- $\alpha\text{Al}_2\text{O}_3$ substrates.

Gas permeability depending on presintering temperature and on substrate thickness

The four 110-8YSZ substrates were further heat-treated at higher temperatures > 1100 °C for 2h in air to enhance the substrate strength. Prior to each heat-treatment step, the gas permeability was examined. According to the pre-sintering temperature, the substrates were labelled as 110-8YSZ, 114-8YSZ, 118-8YSZ and 122-8YSZ for 1100 °C, 1140 °C, 1180 °C and 1220 °C, respectively. The pre-sintering temperature did not influence the gas permeability of substrates significantly until 1180 °C, but at 1220 °C the gas permeability of 8YSZ substrate became much lower, as shown in **Figure 28 (a)**. Furthermore, the 8YSZ substrate became fully dense at 1250°C, exhibiting He-leak rate of 1.4×10^{-05} mbar.l/sec.cm². In addition, gas permeability of substrate was investigated depending on the substrate thickness. The well-polished three 114-8YSZ substrates were used for the measurement. The 114-8YSZ substrates had 2.5 ± 0.07 mm in thickness after surface polish. After their gas permeation test, their thicknesses were reduced to 1.4 ± 0.08 mm. **Figure 28 (b)** shows the relation between the gas permeability and substrate thickness. It is very clear to see that both helium and nitrogen permeability is inversely proportional to the substrate thickness, i.e. 1.9-fold increase in gas permeability with 1.8-fold decrease in substrate thickness.

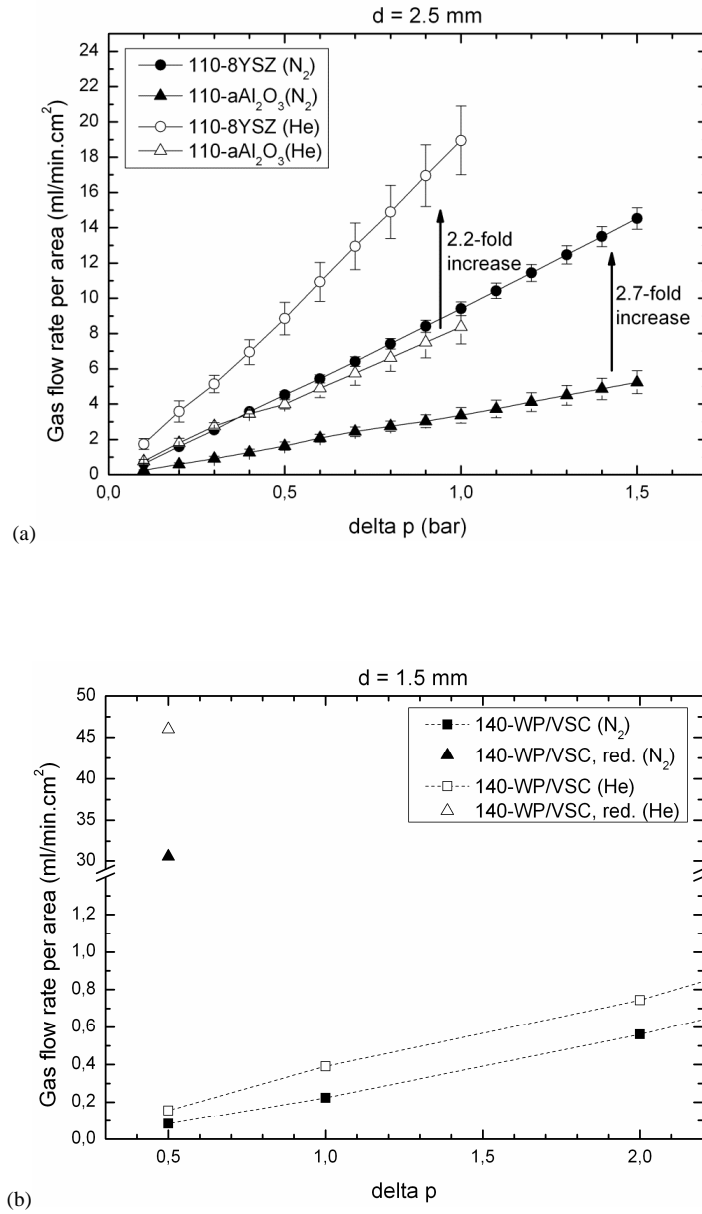


Figure 27 Gas permeability of 110-8YSZ and 110- $\alpha\text{Al}_2\text{O}_3$ substrates, both pre-sintered at 1100 °C for 2h in air (a), and gas permeability of 140-WP/VSC and reduced 140-WP/VSC substrates (b). Gas flow rate per measuring area is displayed as a function of pressure differential.

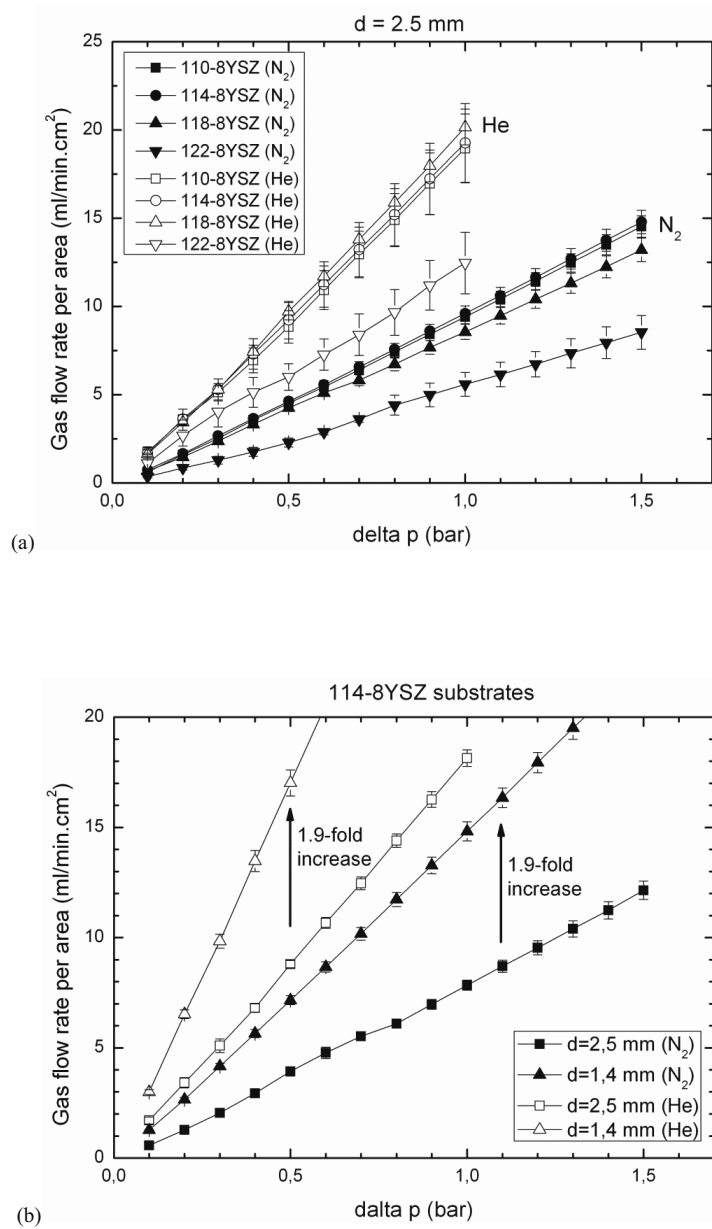


Figure 28 Gas permeability of 8YSZ substrate depending on the presintering temperature (a) and depending on the substrate thickness (b). Gas flow rate per measuring area is displayed as a function of pressure differential.

4.2 Characterization of CGO membrane by wet-chemical deposition

4.2.1 Development of coating liquids

CGO nano-dispersion (NDCGO)

The zeta potential of CGO nano-dispersion was measured as a function of pH and CGO concentration. The stability of NDCGOs were investigated depending on molarities (mol/l) of nitric acids as charge stabilizer (**Figure 29 a**). CGO nano powder was dispersed in various molarities of nitric acid (0, 0.01, 0.05, 0.1 and 0.5 M) yielding 4 wt% NDCGOs. The zeta potential was first increased with increasing molarity of nitric acid and came to the top at 0.05 M nitric acid that is the optimum point regarding the stability of NDCGOs in this work. At 0.10 M nitric acid there was a sudden fall in zeta potential from 20 to 8 mV and the zeta potential was further reduced down to -2 mV with increasing molarity of nitric acid. At the condition between 0.1 M and 0.5 M nitric acid, iso-electric point (IEP) of 4 wt.% NDCGO can be reached. The pH value of NDCGO at 0 M nitric acid (i.e. deionized water) showed 5.3 and it was gradually lowered when increasing the molarity of nitric acid. The stability of NDCGOs regarding the concentration of NDCGOs was also examined (**Figure 29 b**). In this case, the molarity of nitric acid was kept at 0.05 M. The change of pH value was observed relating to the change of concentration of NDCGO. When the concentration of NDCGO increased from 4 wt.% via 8 wt. % to 12 wt.%, the pH value was also increased from 2.8 via 3.1 to 4.6, resulting in decrease of zeta potential from 20 mV via 16 mV to 15 mV.

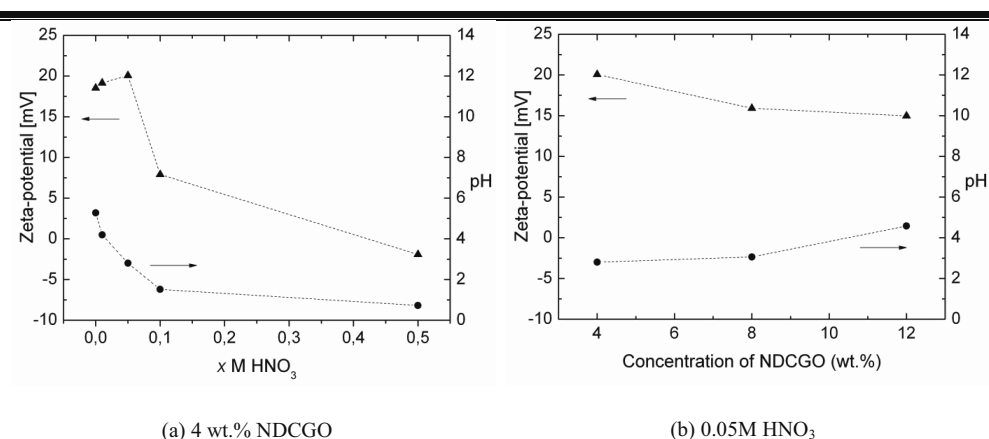


Figure 29 Zeta potential of CGO nano-dispersion as a function of pH (a) and CGO concentration (b).

4. Results and discussion

All prepared NDCGOs were ultrasonicated for 15 min to break the agglomerated larger clusters. In order to remove the remaining large agglomeration and to obtain homogeneously dispersed nano-particles in the solution, the NDCGOs were centrifuged. **Figure 30** shows the NDCGOs after centrifugation with the gravity acceleration of 6500xg for 4 min. It is clear to see in all NDCGOs that the large agglomeration was separated from the solution and sank to the bottom of the centrifuging tube. In addition, the unstable NDCGO such as NDCGO in 0.5 M nitric acid showed up transparent solution, indicating that the CGO nano particles were quickly re-agglomerated after ultrasonication due to the instability of NDCGO (close to iso-electric point) and thus segregated all clearly from the solution. The NDCGO in the deionized water exhibited slightly lighter yellow than both NDCGOs in 0.05M and 0.01 M nitric acids, which means lower final concentration of NDCGO (verified in **Figure 32**).

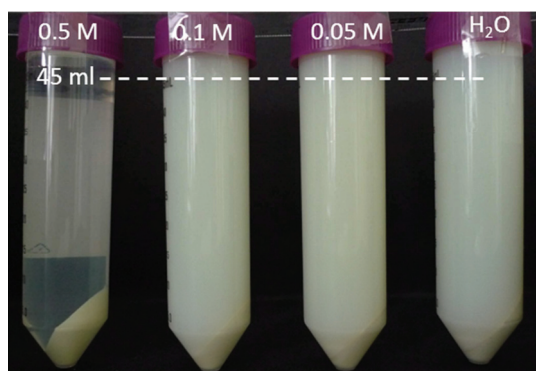


Figure 30 Photograph of NDCGOs after centrifuging with the gravity acceleration of 6500xg for 4 min.

The particle size of prepared NDCGOs was investigated using HORIBA LB-550 as a function of the time (day) as shown in **Figure 31**. **(a):** 4 wt% of NDCGOs were dispersed in various molarities of nitric acid and centrifuged with the gravity acceleration of 3500 and 6500xg. The centrifugation time was always kept at 4 min over the whole work. The segregated particles were removed and only homogeneously dispersed NDCGOs were used for particle size measurement. The NDCGO-0.1M HNO₃ looks similar to the NDCGO-0.05M HNO₃ in **Figure 30**, but it had larger effective particles (d_{50} at 3500xg: ~150 nm and d_{50} at 6500xg: ~125 nm) and very fast agglomeration rate. While the particle size of NDCGO-0.05M HNO₃ involving initial particle size d_{50} at 3500xg of ~ 100 nm and d_{50} at 6500xg of ~ 90 nm was increase to 120 nm at 3500xg and 110 nm at 6500xg after 1 day and kept this particle size until 4th day, the particles in the NDCGO-0.1M HNO₃ were rapidly growing and reached ~ 270 nm on 4th day for both gravity accelerations. **(b):** In case of concentration influence on particle evolution, only 0.05M HNO₃ was used as a dispersant and various solid concentrations of NDCGO were prepared, e.g. 4, 8 and 12 wt% of NDCGO. Like (a), the NDCGOs were centrifuged with the gravity acceleration of 3500 and 6500xg. After removing the segregated particles, the particle size was measured. When the solid concentration was increased, larger initial and also final particle sizes exhibited which were 1.5 ~2.0 and 3.0 ~ 5.0-fold larger than the initial and final particle size of 4wt.% NDCGO, respectively.

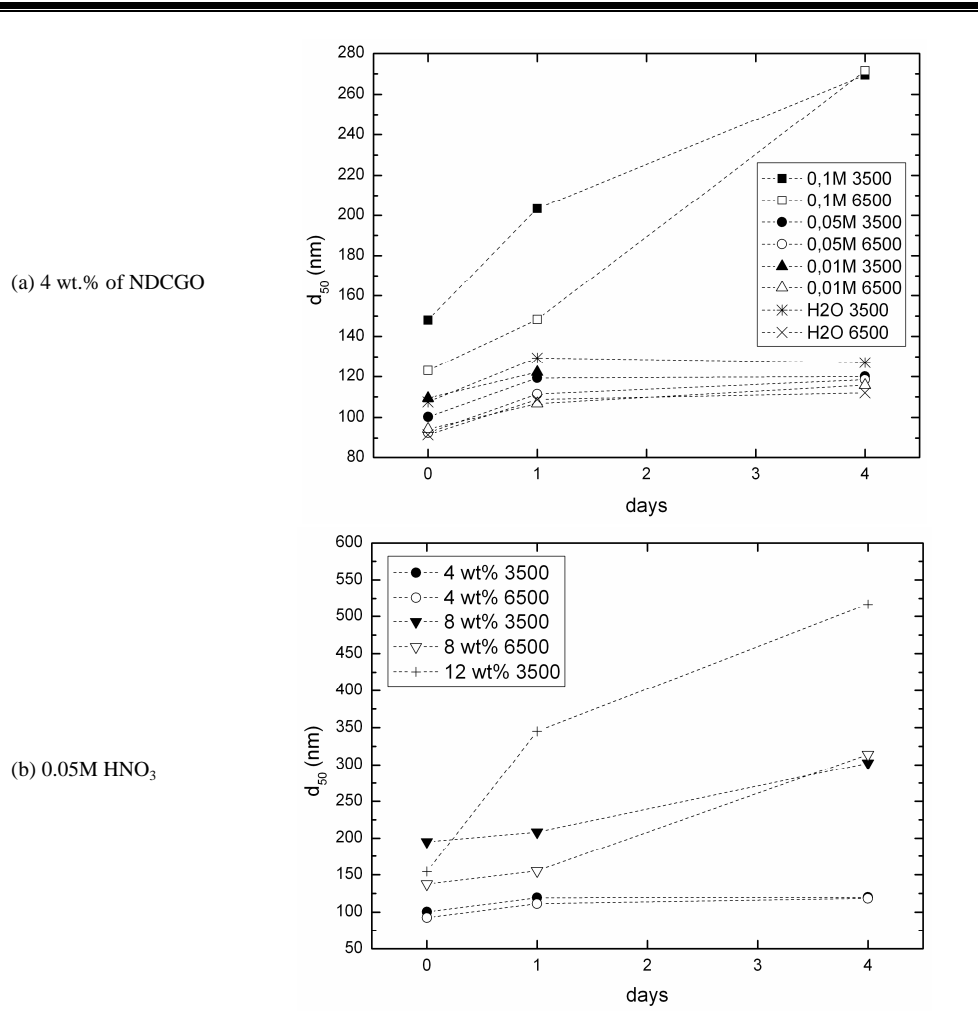


Figure 31 Particle size (d_{50}) of CGO nano-dispersion as a function of pH (a) and CGO concentration (b).

After centrifugation, the NDCGOs were dried overnight at 60 °C to confirm the final concentration of nano powders. The measured final concentrations were displayed in **Figure 32**. As expected above, the NDCGO-H₂O had lower final concentration than the other NDCGOs. The final concentration of NDCGO-0.05M HNO₃ was lower than that of NDCGO-0.01M HNO₃ when centrifuged with 3500 xg, but they showed opposite results when centrifuged with 6500 xg. With increasing initial concentration (4 → 8 → 12 wt.%), the final concentration was also increased (1.5 → 2.5 → 4.5 wt.% for 3500xg-centrifuged NDCGOs).

4. Results and discussion

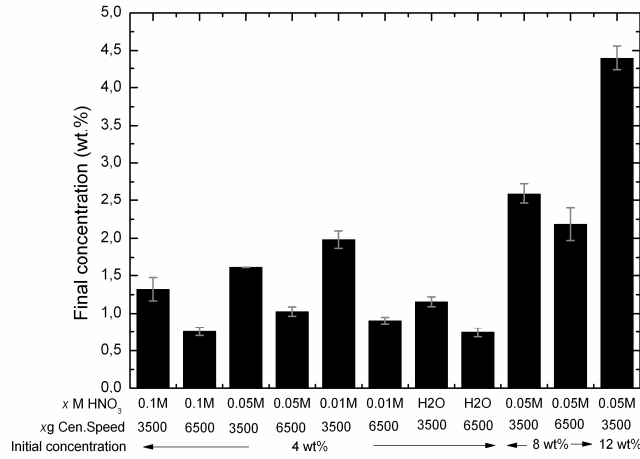


Figure 32 Final concentration (wt.%) of NDCGOs

Figure 33 shows XRD patterns of sintered NDCGO-0.05 M HNO_3 powders as a function of heat-treatment temperatures, 500, 800 and 1100 °C for 2h and at 1400 °C for 5h in air. The 5 hours for temperature 1400 °C was chosen because the NDCGO-coated samples were finally fired at 1400 °C for 5 h. All CGO powders exhibit no impurity phase and only single phase like CeO_2 (fluorite structure, JCPDS 01-075-0162). The development of C-type structure of Gd_2O_3 in CeO_2 cannot clearly be identified from the XRD patterns since the reflections overlap heavily due to the close relationship between the C-type and fluorite structures. The crystallinity of NDCGO powder was gradually improved as the temperature of heat-treatment increased and showed a (111) preferred orientation. The lattice parameters 5.425 Å was detected independent of temperature. This lattice parameter is an agreement with the equation given in Zha's work [19], $a(x)=5.4121+0.0525x$ for $\text{Ce}_{1-x}\text{Gd}_x\text{O}_{2-x/2}$, because x of prepared NDCGO is turned out to be 0.24 as following result of chemical analysis (see below).

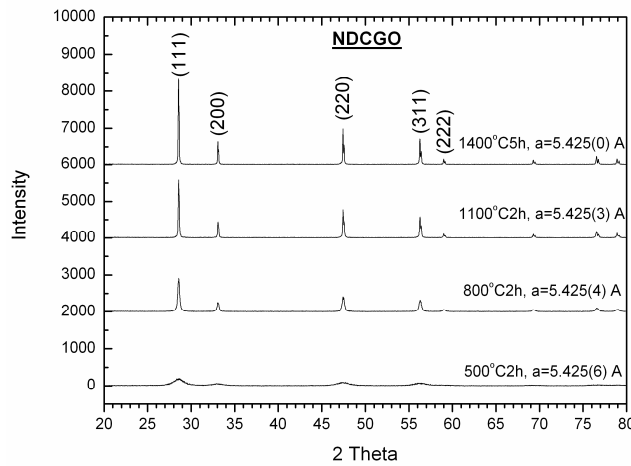


Figure 33 X-ray diffraction patterns: Crystallization behaviour of NDCGO powders as function of temperature of heat treatment.

The chemical analysis of prepared NDCGO powder was carried out using ICP-OES at ZCH in FZJ. NDCGO powder was obtained from the 1.0NDCGO(0.05M HNO₃)/PVA2 after calcination at 500 °C for 2h in air. **Table 11** shows the stoichiometry of NDCGO powder that was calculated from the detected weight ratio of Ce and Gd elements and their relative errors are $\pm 3\%$. The result indicates that more gadolinium is doped to the ceria than the expected stoichiometry Ce_{0.8}Gd_{0.2}O₂, which has positive potential for increasing ionic conductivity due to the formation of more oxygen vacancies in the lattice by introducing more gadolinium.

Table 11 Stoichiometry of prepared NDCGO powder (relative error $\pm 3\%$ of wt.%).

Desired stoichiometry	NDCGO-0.05M HNO ₃ , 500 °C 2h
Ce _{0.8} Gd _{0.2} O ₂	Ce _{0.76} Gd _{0.24} O ₂

CGO colloidal sol (CSCGO)

The use of ammonium hydroxide solution resulted in a voluminous yellowish or orange sol (or precipitation at higher concentration NH₃.H₂O) from Ce(III) and Gd(III) nitrate solution (**Figure 34**). The more amount of ammonium hydroxide solution was added, the higher the pH value was detected and the larger particles had formed. Particularly, the precipitation had rapidly formed directly after addition of 0.7g or 1.2g ammonium hydroxide and sunk on the bottom. Godinho [91] proposed the following reactions for gadolinium-doped ceria:

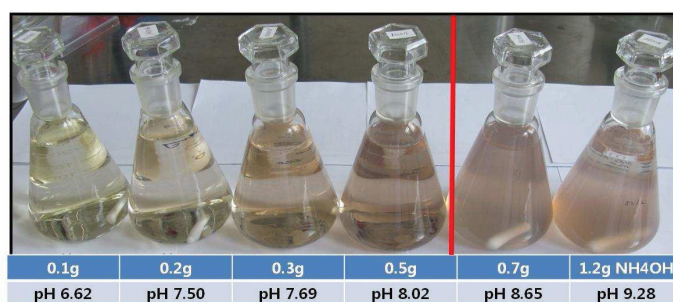
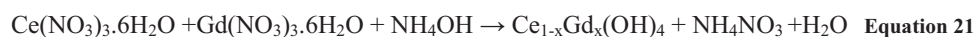


Figure 34 CGO colloidal sols prepared with addition of various amounts of ammonium hydroxide solution.

Figure 35 shows the particle size (d_{50}) change depending on pH (a) and on aging time (b). The particle size grew up progressively with increasing pH from $d_{50} = 6$ nm at pH 6.62 via $d_{50} = 18$ and 40 nm at pH 7.50 and 7.69, respectively, to $d_{50} = 122$ nm at pH 8.02. At higher than pH 8.02, the particle size measurement was not carried out due to fast precipitation sinking down to the bottom. The particle size became also larger with the aging time. The prepared CSCGO with 0.2g NH₄OH exhibit relatively constant particle size ($d_{50}=21$ nm) for 100 min

4. Results and discussion

but rapid grow of the particle size was observed after 200 min yielding $d_{50} = 88\text{nm}$. Therefore, the CSCGO sol was used as coating solution within 100 min after preparation.

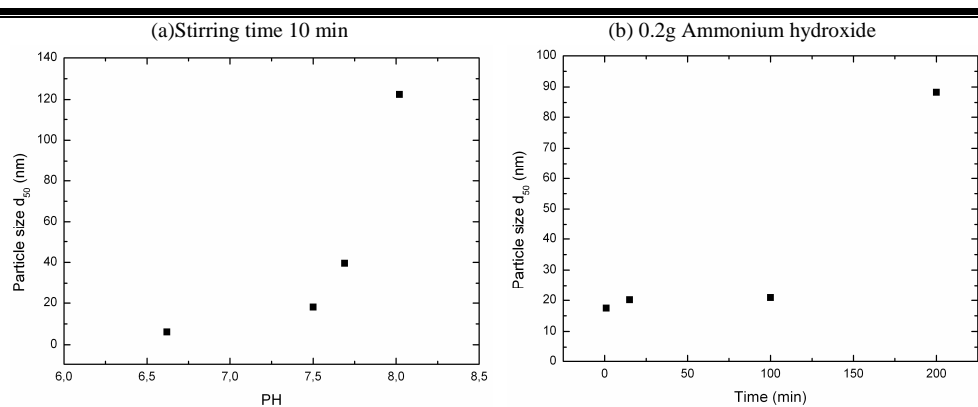


Figure 35 Particle size of prepared CSCGOs as a function of pH (a) and time (b).

Figure 36 shows a dried CSCGO/PVA-Xerogel (a) and XRD patterns of CSCGO route derived CGO powder (b). The peaks of the calcined CSCGO powder corresponds to the fluorite structure of CeO_2 (PDF card number: 01-075-0162) and exhibits no impurity phase. As discussed in XRD results of NDCGO, the development of C-type structure of Gd_2O_3 in CeO_2 cannot clearly be identified from the XRD patterns due to the heavy overlap of the reflections.

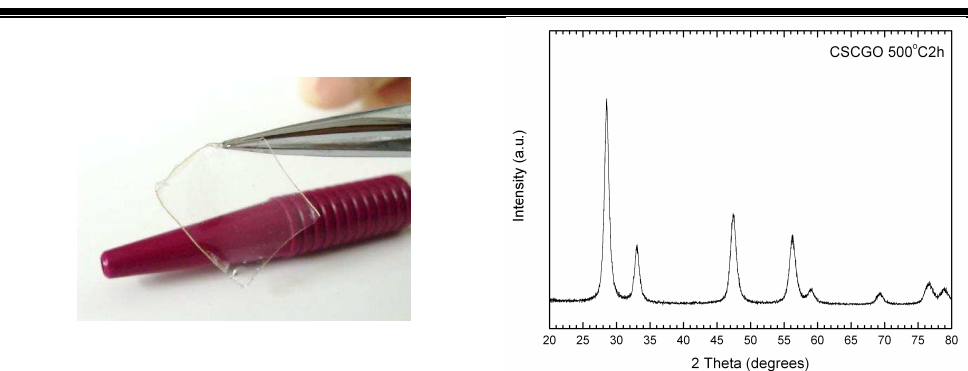


Figure 36 Photograph of CSCGO/PVA-Xerogel (a) and XRD patterns of colloidal sol-gel route derived CGO (CSCGO) powders calcined at 500°C for 2h in air (b).

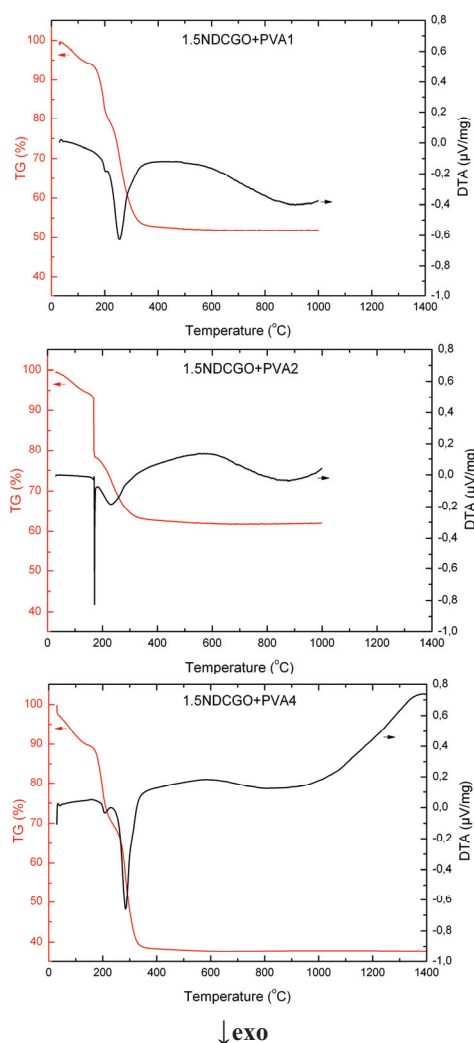
The chemical analysis of prepared CSCGO powder was carried out using ICP-OES at ZCH in FZJ. CSCGO/PVA2 was calcined at 500°C for 2h in air and the resulting powder was measured. **Table 12** shows the stoichiometry of CSCGO powder that was calculated from the detected weight ratio of Ce and Gd elements with relative errors $\pm 3\%$. As a result, the desired stoichiometry was obtained.

Table 12 Stoichiometry of prepared CSCGO powder (relative error $\pm 3\%$ of wt.%).

Desired stoichiometry	CSCGO, 500 °C 2h
$\text{Ce}_{0.8}\text{Gd}_{0.2}\text{O}_2$	$\text{Ce}_{0.79}\text{Gd}_{0.21}\text{O}_2$

Thermal analysis (TGA-DTA of NDCGO/PVA-Xerogel)

The knowledge of the decomposition behavior of organic components is of great importance for the residue-free burnout from the inorganic materials. Particularly with regard to the use of organic binders such as PVA, the implementation of a thermal analysis is necessary. The prepared final NDCGO/PVA mixtures were dried at room temperature and the decomposition behavior of Xerogels is shown in **Figure 37** using TG-DTA (Thermogravimetry - Differential Thermal Analysis) at the temperature range of 30~1000 °C or 30~1400 °C with heating rate $+1\text{Kmin}^{-1}$. Weight loss in the sample was observed due to the loss of adsorbed moist at below 100 °C. The sample exhibits two exothermic peaks in the DTA indicating temperatures, 204°C and 255°C for PVA1, 171°C and 232°C for PVA2 and 207°C and 285°C for PVA4. In the thermogram, the major weight loss is observed in the range 150-400 °C. The comparison of the total weight loss between Xerogels was not taken into consideration, because only some parts of dried Xerogels were used for the measurement. The burnout of the organic components is completed at approx. 400 °C. Therefore, a residue-free combustion can be expected at the temperature of 500 °C that is adopted as a calcination temperature in this whole work.

**Figure 37** TGA-DTA plots of 1.5NDCGO-PVA (1, 2 and 4)-Xerogels.

4.2.2 Development of CGO membrane on WP/VSC (NiO/8YSZ) substrate

Coating layers after heat-treatment.

CGO membranes deposited on 100-WP/VSC substrates using 1.0 and 1.5 wt.% CGO nano-dispersions (so-called 1.0NDCGO and 1.5NDCGO) was investigated by SEM. After calcination, the coating thickness was measured using 5 different positions based on the SEM images and depicted in **Figure 38**. For both samples, the first coating layer was thinner than second coating layer due to the different film formation rate. The film formation rate of first coating layer became lower due to the smaller capillary pressure derived by larger pore size of the substrate, while the film formation rate of second coating layer is higher due to the larger capillary pressure derived by smaller pore size of the first coating layer, resulting in different coating layer thickness. In addition, some NDCGO particles could be infiltrated into the large pores existing on the substrate surface. The coating layer thickness after calcination correlated with the concentration of NDCGO. When the concentration increased from 1.0 wt.% to 1.5 wt.%, the coating layer thickness also exhibited 1.5-fold increase.

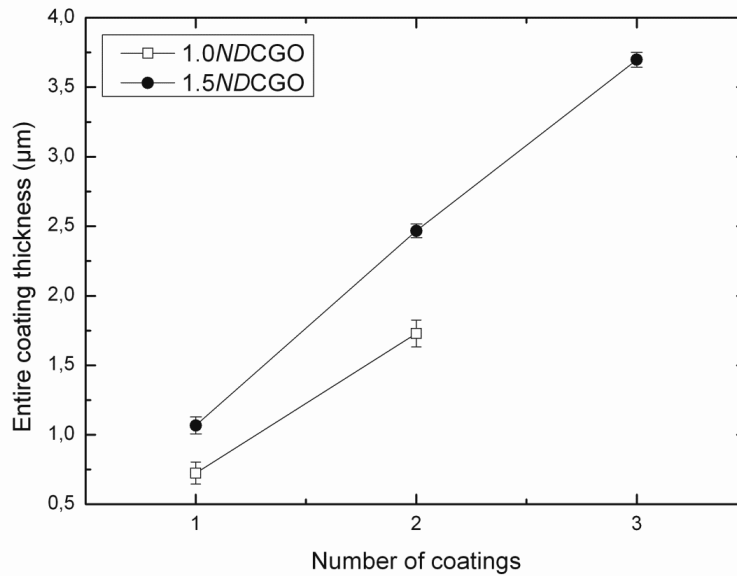


Figure 38 Coating thickness of double 1.0NDCGO and triple 1.5NDCGO layers that were spin-coated with rotation speed 800rpm for 60sec. PVA2 was used as binder for both. Each coating layer was calcined at 500°C ± 2 Kmin⁻¹ for 2h in air.

Figure 39 shows SEM images of NDCGO coatings after calcinations. It is clear to see that very small CGO particles agglomerated and exhibits clusters with diameter < 100 nm. With fracture surface images using BSE, spin-coated CGO layers can be clearly distinguished. **Figure 40** shows SEM images of sintered NDCGO coatings. At 1400°C the CGO layer became fully dense with grain size $0.5 - 2\ \mu\text{m}$. The VSC interlayer of WP/VSC became also relatively dense but WP base substrate of WP/VSC remained as porous structure.

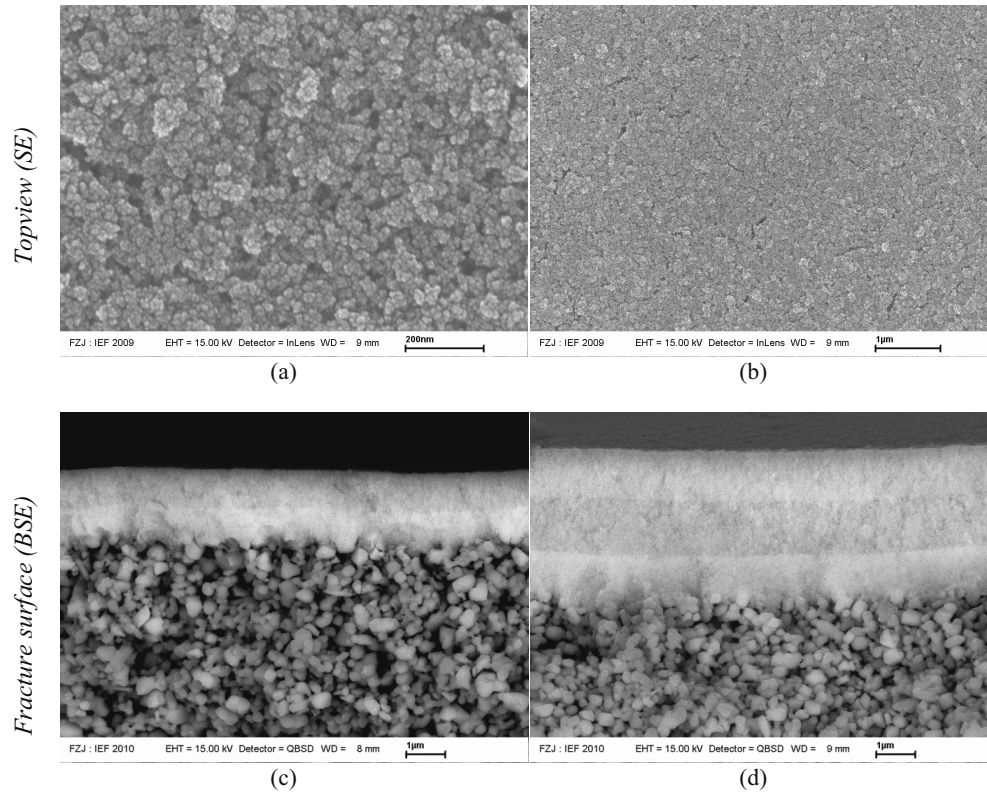


Figure 39 FEG-SEM images of NDCGO on 100-WP/VSC, calcined at 500°C for 2h in air: (a, b) double CGO coatings using 1.0NDCGO and PVA3, (c) double CGO coatings using 1.0NDCGO and PVA2, and (d) triple CGO coatings using 1.5NDCGO and PVA2.

4. Results and discussion

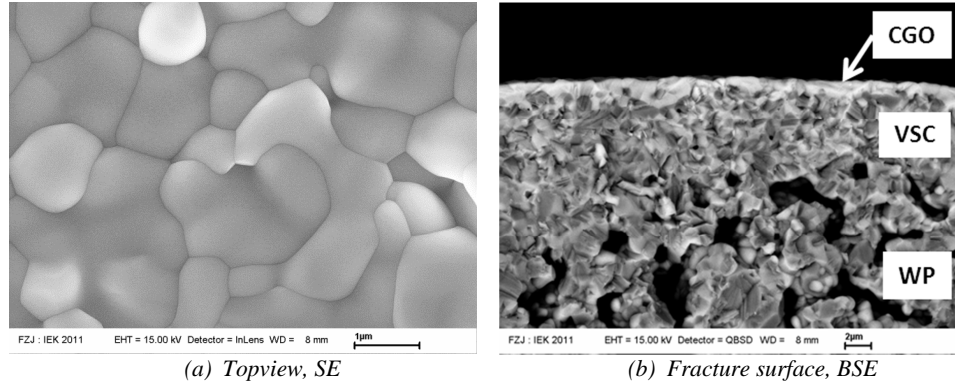


Figure 40 FEG-SEM images of NDCGO on 100-WP/VSC, sintered at 1400°C (± 5 -1Kmin⁻¹) for 5h in air: double CGO coatings using 1.5NDCGO and PVA4.

NDCGO membrane depending on spin-coating parameter

The influence of the process parameters for spin-coating on the gas-tightness of sintered CGO membranes was investigated in this work. The rotation time or rotation speed was varied. Besides coating process parameter, the influence of coating numbers, e.g. from double to triple coatings, was also considered.

Gastightness evaluation as a function of rotation time

As shown in **Figure 41 (a)**, the rotation speed was kept at 800 rpm and various rotation times were applied. A mixture of 1.5NDCGO + PVA2 was used as a final coating sol. Every coating layer was calcined at 500 °C at ± 2 Kmin⁻¹ for 2h in air and final double coatings supported by 100-WP/VSC were fired at 1400 °C for at ± 3 -5Kmin⁻¹ for 5h in air. Subsequently, their gas-tightness was evaluated by single gas permeation test. **Figure 41 (b)** shows helium flow rate of double coated NDCGO membranes as a function of rotation time. The helium flow rate was decreased when the rotation time was shortened (60 → 40 → 20 sec.). It might be caused by the increase of coating thickness or coating homogeneity. Nitrogen gas permeation test yielded same gas-tightness behavior and thus was excluded.

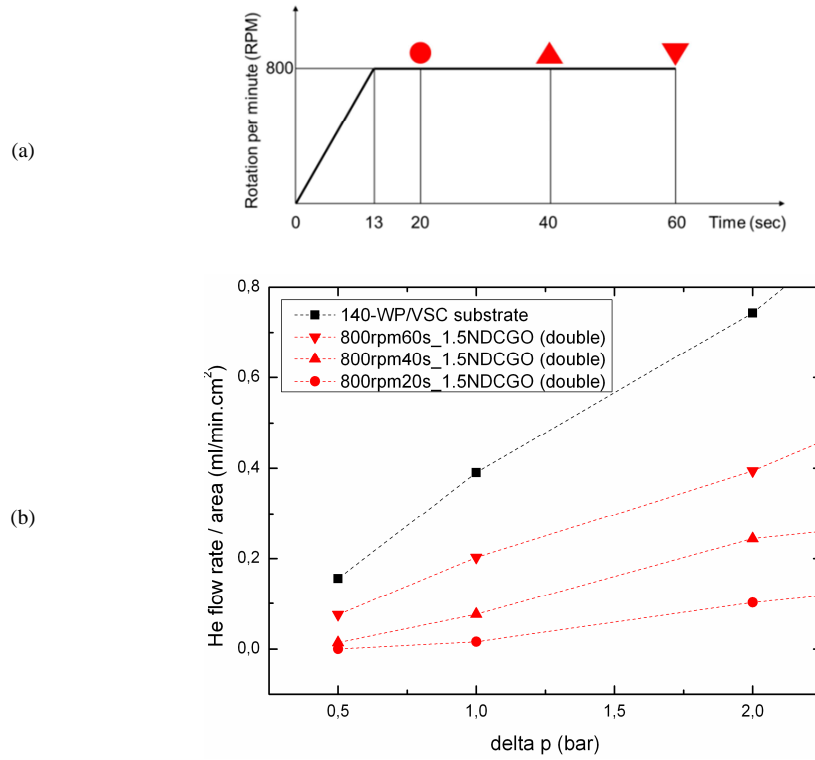


Figure 41 Process parameters for spin-coating with their corresponding symbols (a), and helium flow rate of double coated NDCGO membranes as a function of rotation time (20, 40 and 60 sec.) (b). 1.5NDCGO + PVA2 was used as a final sol and all layers were calcined at $500\text{ }^{\circ}\text{C}$ at $\pm 2\text{Kmin}^{-1}$ for 2h in air. Subsequently, all coated samples were fired at $1400\text{ }^{\circ}\text{C}$ for 5h in air at $+3/-5\text{Kmin}^{-1}$.

Gastightness evaluation as a function of rotation speed and coating numbers

The rotation time was kept at 20 sec and the rotation speed was varied in this work (**Figure 42 (a)**). Additionally, triple-coating-layer was carried out to help covering potential open pores. **Figure 42 (b)** shows corresponding symbols for double and triple coating layers. The used final sol and heat-treatment profile were identical as described in ‘gastightness evaluation as a function of rotation time’. In case of double coating layers, the decrease in rotation speed exhibits no significant influence between 600 rpm and 800 rpm, but at 400 rpm the helium flow rate was increased considerably. In case of triple coating layers, no matter how high the speed all triple coating layers exhibit higher helium flow rate than double coating layers because of microcrack formation as following.

4. Results and discussion

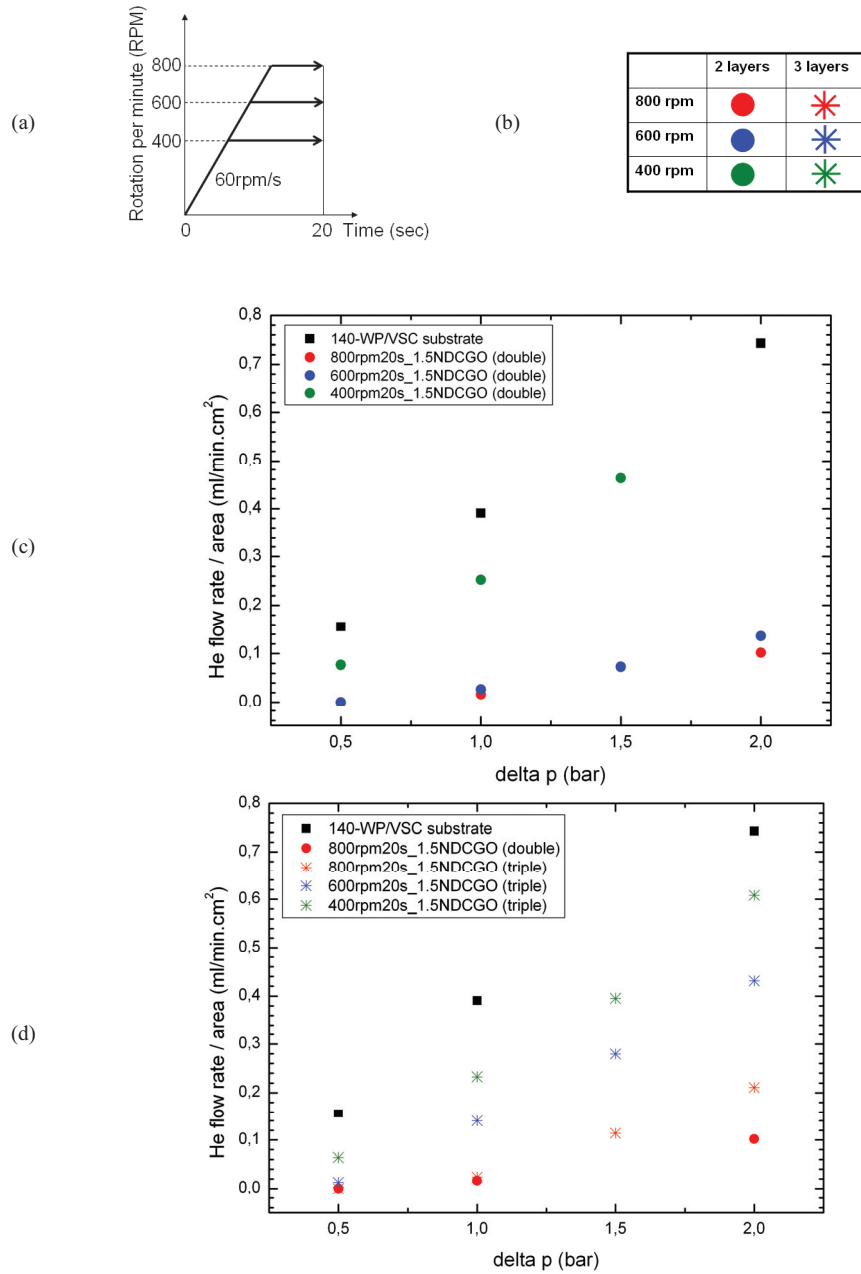


Figure 42 Spin-coating parameters (a), their corresponding symbols for double and triple coatings (b), and helium flow rate of double (c) and triple (d) coated NDCGO membranes as a function of spin-coating RPM. 1.5NDCGO + PVA2 was used as a final sol and all layers were calcined at 500 °C at $\pm 2\text{Kmin}^{-1}$ for 2h in air. Subsequently, all coated samples were fired at 1400 °C for 5h in air at $\pm 3/-5\text{Kmin}^{-1}$.

Thermal cracking behavior of triple CGO coatings by CLM

Figure 43 shows CLM images of cracking pattern on the surface of triple CGO coatings. The cracks for 400 and 600 rpm were observed after calcination which might occur due to the excess of critical film thickness led by the reduction in rotation speed. In contrast to them, there was no prior crack after calcination in the CGO coatings with 800 rpm. The cracks were generated during sintering process. It is further investigated as follows.

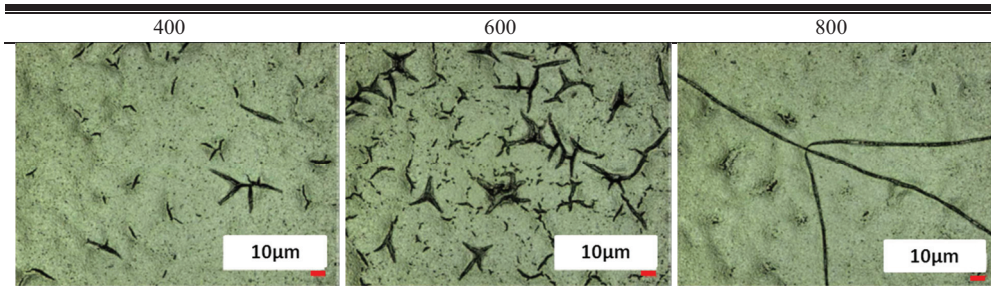


Figure 43 CLM images of thermal cracking behavior of *triple* CGO coatings on 100-WP/VSC substrate. 1.5NDCGO + PVA2 was used as a final sol and all layers were calcined at 500 °C at $\pm 2\text{Kmin}^{-1}$ for 2h in air. Subsequently, all coated samples were fired at 1400 °C for 5h in air at $+3/-5\text{Kmin}^{-1}$.

Effect of cooling rate on crack formation in CGO coating layers

Sintering process involves crystallization of the coating layer and thus requires shrinkage of the coating layer. Due to the constraint of the substrate, tensile stress is generated in the coating layer and some of the stress can be released by diffusive mechanisms at the temperature of crystallization. After heat process, cracks can be generated in the coating layer during cooling of sintering process, which are related to the residual stress caused by thermal mismatch between coating layer and substrate. To minimize influence of this stress the cooling rate was decreased from -5 to -1 and -0.5 Kmin^{-1} as programmed in **Figure 44**.

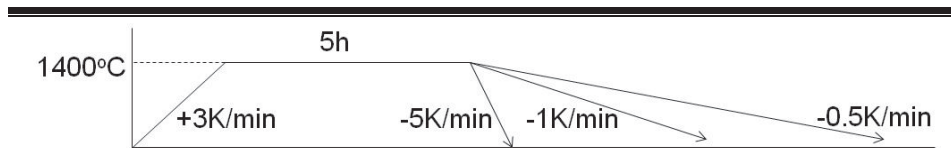


Figure 44 Sintering program with different cooling rates.

Figure 45 shows the sintered CGO coating layers with different cooling rates. As clearly shown in CLM images, the cracks were weakened with the decrease in cooling rate. Using the height profile analysis the depth of the cracks was evaluated. At cooling rate -5 Kmin^{-1} , the cracks were propagated with approx. 1.7 μm in depth that is nearly close to the thickness of the triple-CGO coating layer after sintering (approx. 2 μm). At -1.0 Kmin^{-1} , the propagation

4. Results and discussion

depth of the cracks was shortened to approx. $0.7\ \mu\text{m}$ and finally did not appear at $-0.5\ \text{Kmin}^{-1}$. The sample surface displayed in **Figure 45** (b) was further investigated by SEM (HITACHI) as shown in **Figure 46**. The crack did not appear at all and in some area the valley of layer has formed, indicating tensile stress to the coating layer was suppressed with the decrease in cooling rate.

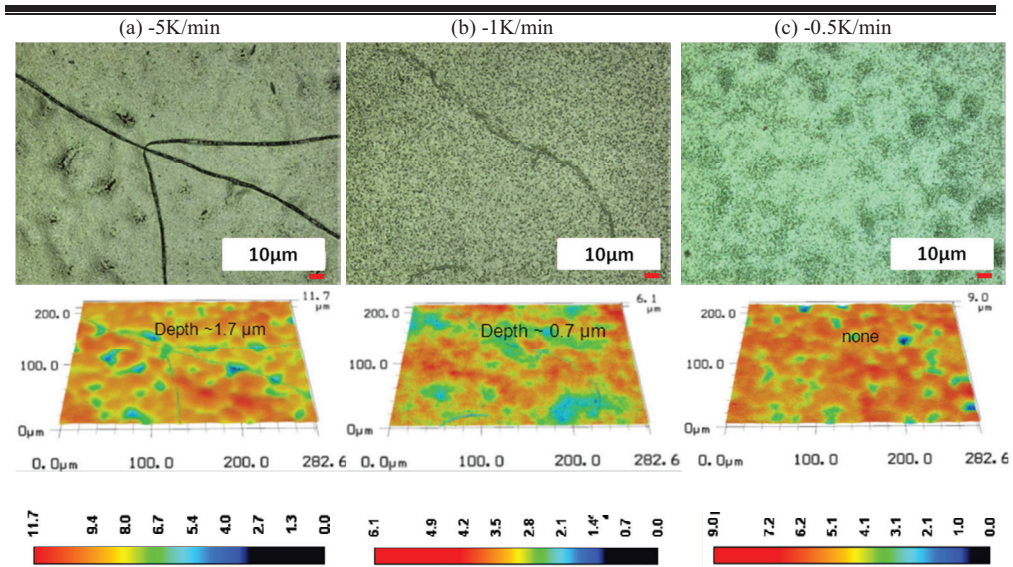


Figure 45 Laser+color (up) and height (bottom) images by CLM. *Triple* NDCGO coatings on 100-WP/VSC substrate. '1.5NDCGO + PVA2' was used as a final sol and all layers were calcined at $500\ ^\circ\text{C}$ at $\pm 2\ \text{Kmin}^{-1}$ for 2h in air. Subsequently, the coated samples were fired at $1400\ ^\circ\text{C}$ for 5h in air at $+3/-5$ (a), -1 (b) and $-0.5\ \text{Kmin}^{-1}$ (c). Unity of value in scale bar is μm .

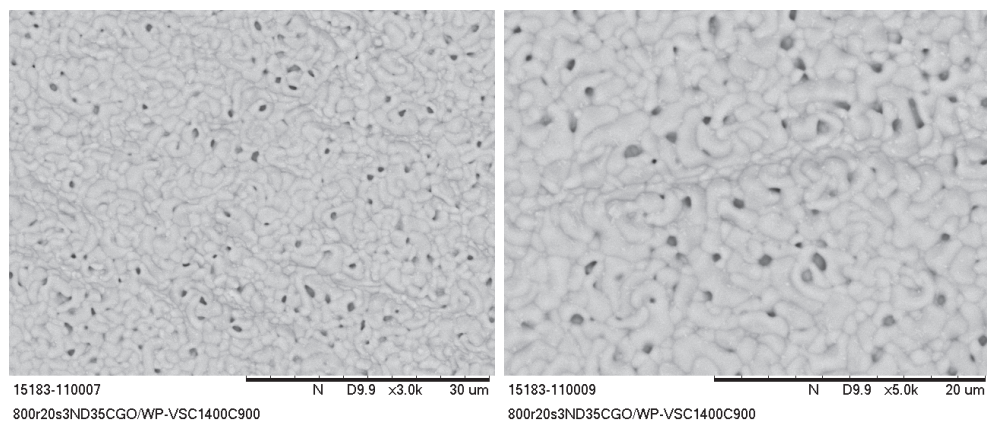


Figure 46 SEM (HITACHI) images of the sample displayed in **Figure 45** (b) after reducing.

Effect of MW of PVA on crack-free coating layer

The influence of molecular weight (MW) of PVA on the critical coating layer thickness (or microcrack formation) was investigated in this work. Four different solid concentrations of NDCGO (1.0, 1.5, 2.5 and 3.5 wt.%) that were directly related to the coating layer thickness were mixed with three different MWs of PVA (PVA1, PVA2 and PVA4), producing various final coating liquids. The various final coating liquids were double spin-coated on the 100-WP/VSC substrates with rotation speed 800 rpm and spinning time 20s. Each coating layer underwent the calcination and subsequently the samples were fired at 1400 °C at for 5h in air. The cooling rate of -1 Kmin^{-1} was adapted to minimize the risk of cracking.

Table 13 shows the observation of microcrack formation after calcination. When the solid concentration of NDCGO increased the microcracks were detected by CLM, but with adopting higher MW of PVA crack-free coating layers could be achieved. Due to the solvent evaporation, the coating layer near surface shrinks faster than internal coating layer near substrate, the tensile stress occurs close to the surface of the coating layer. The constant rate period (CRP) of drying extends with increasing MW of PVA, since PVA with more complicated polymer chains migrates to the surface and thus solvent evaporation becomes harder. [92]. Consequently, it leads to the depression of the internal stress and thus prevents the crack formation during drying. In other words, the critical coating layer thickness can be increased by using higher MW of PVA.

Table 13 Microcrack formation in double coated NDCGO membrane after calcination (500°C/2h/air), depending on the concentration of NDCGO and on the molecular weight (MW) of PVA, observed by confocal laser microscope. 'X' is expected to be crack formation and '-' cannot be judged.

	PVA1 (MW22000)	PVA2 (MW60000)	PVA4 (MW145000)
4.5NDCGO (4.5wt.%)	X	X	Crack
2.5NDCGO (2.5wt.%)	Crack	Crack	No crack
1.5NDCGO (1.5wt.%)	Crack	No crack	No crack
1.0NDCGO (1.0wt.%)	-	No crack	No crack

Figure 47 shows SEM images of sintered CGO coating layers using various solid concentrations of NDCGO when the highest MW of PVA (PVA4 in this work) was added. The PVA4 enabled the CGO coating layer with thickness of approx. 2µm. The cracks did not appear until 2.5NDCGO. Many pinholes were visible in SEM topview when a mixture of 2.5NDCGO and PVA4 was used as a final coating liquid, which are not related to the effect of MW of PVA but to the stability of NDCGO. As discussed in **section 4.2.1** NDCGO became less stable with increasing the solid concentration of NDCGO and shortened the life time of stable dispersion of CGO nanoparticles. Although the 2nd coating layer using 2.5NDCGO was coated right after calcination of the 1st coating layer (i.e. after 24 hours), CGO nanoparticles formed the aggregates and thus created many pinholes.

4. Results and discussion

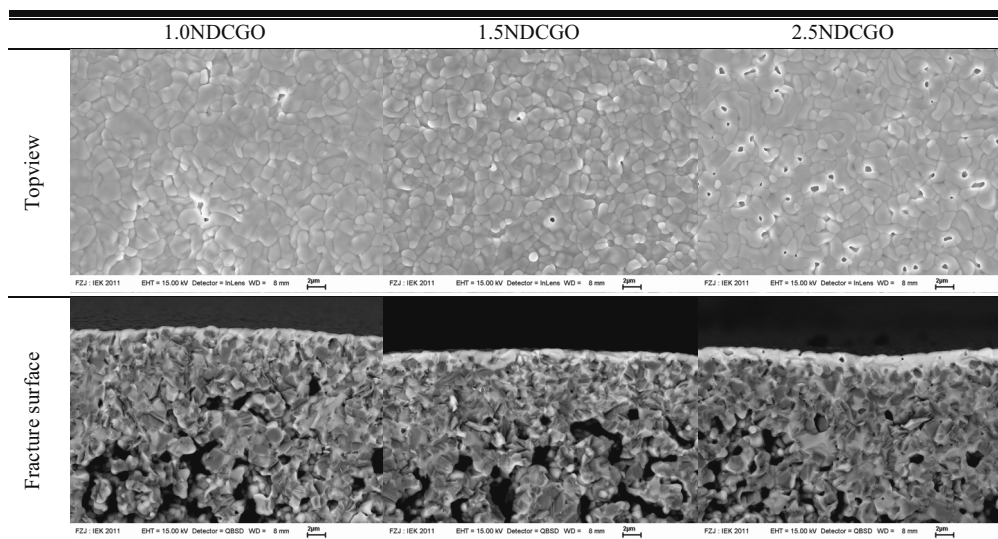


Figure 47 FEG-SEM images of NDCGO membranes using various concentrations of NDCGO and PVA4. Double spin-coated layers were calcined at 500 °C at $\pm 2 \text{ kmin}^{-1}$ for 2h in air and fired at 1400 °C at $+3/-1 \text{ Kmin}^{-1}$ for 5h in air

Figure 48 shows crack behaviour as a function of MW of PVA when 2.5NDCGO was used. As shown in topview images of CLM and SEM, severe cracks were generated with the lowest MW of PVA (PVA1) and crack density was considerably reduced with increasing MW of PVA due to the reduction of internal stress in the coating layer. The cracks observed after calcination obviously propagated further during sintering process and the width of cracks became broader. The decohesion of intra-coating layer occurred, to be accurate between the 1st and 2nd coating layer (see the image of fracture surface). As mentioned above, the shortened life time of the 2.5NDCGO is the responsible for the pinholes observed on the surface of the 2nd coating layer, which can be suppressed with adjusting pH value for NDCGO.

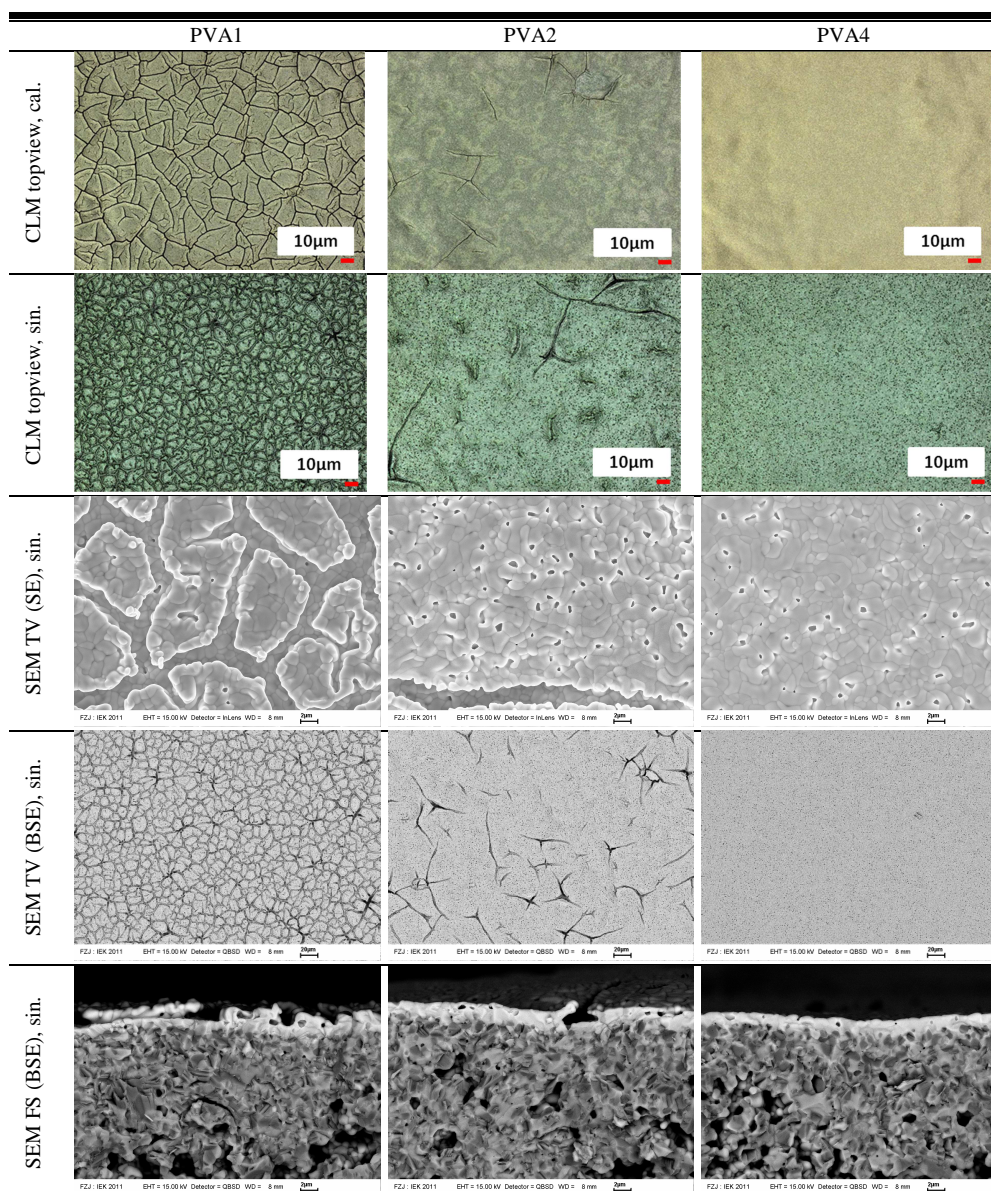


Figure 48 CLM (upper) and FEG-SEM (bottom) images of NDCGO membranes using 2.5NDCGO and various MWs of PVA. Double spin-coated layers were calcined at 500 °C at $\pm 2 \text{ kmin}^{-1}$ for 2h in air and fired at 1400 °C at $\pm 3/-1 \text{ Kmin}^{-1}$ for 5h in air. *cal.: calcined sample, sin.: sintered sample, TV: topview, FS: fracture surface.

Gastightness evaluation by He leak test

The gastightness of double or triple coated NDCGO membranes was evaluated by helium leak test. Available substrates were limited and thus single sample was tested for each condition, except for sintered substrates. The resulting helium leak rates for sintered NDCGO membranes on WP/VSC substrates are displayed in **Figure 49**. With increasing of solid concentration of NDCGO, the gastightness of sintered CGO membranes was noticeably improved, i.e. helium leak rate (mbar.l/cm².sec.) was decreased, for example, from 7.4×10^{-3} of '1.0NDCGO' to 1.5×10^{-3} of '2.5NDCGO' when PVA4 was used for double coatings (black symbols), and from 7.5×10^{-4} of '1.5NDCGO' to 1.1×10^{-4} of '2.5NDCGO' when PVA4 was used for triple coatings (red symbols). The triple-coated CGO membranes exhibit lower helium leak rates than the double-coated CGO membranes. The sintered CGO membrane was prepared by triple coatings using a mixture of 2.5NDCGO and PVA4, and was further heat-treated at 900 °C at $\pm 3/-1 \text{ Kmin}^{-1}$ for 3h under reducing atmosphere Ar/4%H₂. As a result, the helium leak rate was increased to 1.1×10^{-3} mbar.l/cm².sec. It might be concerned with the porous structure formation of the substrate. The WP/VSC interlayer and substrate, both consisting of NiO and 8YSZ, becomes additionally porous during heat-treatment under reducing atmosphere regarding as $\text{NiO} \rightarrow \text{Ni} + 0.5\text{O}_2$. Therefore, the He permeability through substrate is increased and the traveling path way where helium gas escapes is shortened. Consequently, helium gas is delivered more readily from substrate side to membrane side. In addition, the possibility of exposure of through-connected pores might be increased. The porous structures of the WP/VSC substrate after reducing were revealed in **Figure 50**. The pinholes in NDCGO membrane formed during sintering remained after reducing substrate.

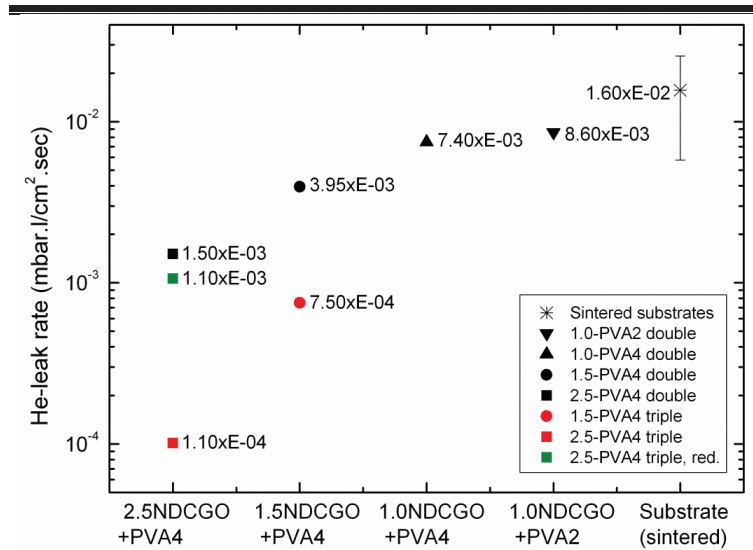


Figure 49 Gastightness evaluation by He leak test. He leak rates were displayed for various concentrations of NDCGO and MWs of PVA. Double or triple spin-coated layers were calcined at 500 °C at $\pm 2 \text{ Kmin}^{-1}$ for 2h in air and fired at 1400 °C at $\pm 3/-1 \text{ Kmin}^{-1}$ for 5h in air. (15789 samples: size 40x40mm, measured diameter of He leak rate: $\phi_{\text{double}} = 20\text{mm}$, $\phi_{\text{triple}} = 10\text{mm}$, $\phi_{\text{support}} = 10\text{mm}$).

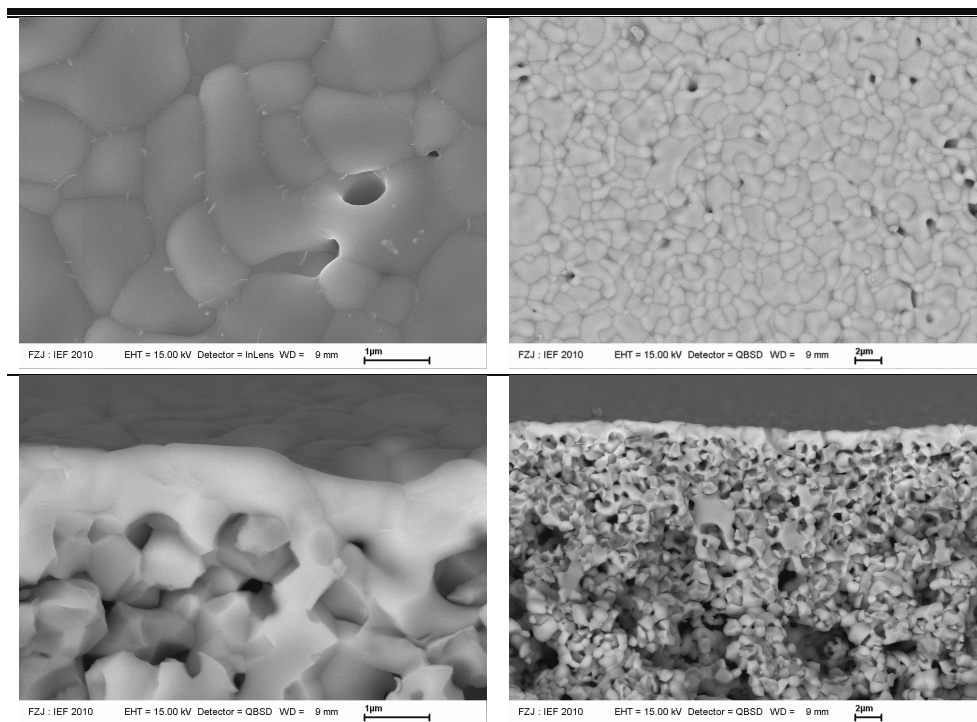


Figure 50 FEG-SEM images of NDCGO deposited on WPVSC (NiO/8YSZ), fired at 1400 °C at $+3/-1\text{Kmin}^{-1}$ for 5h under air and further heat treated at 900 °C at $+3/-1\text{Kmin}^{-1}$ for 3h under Ar/4%H₂. For the NDCGO layers a mixture of 1.0NDCGO and PVA2 was used as final coating liquid.

Micro-defects investigation

To obtain defect-free membrane, most of all, the sources causing defects on the coating layers should be investigated since the primary defects further remain on the finished product. In this section, some crucial defect sources are discussed.

Defect formation due to air bubbles on coating liquid (Figure 51)

The most important task to avoid the defect of coating layer is the purification of the coating liquid and binder to remove the agglomerates or potential dirt. Although the coating liquids and binders were purified using a 0.8 μm-syringe filters and coating process was carried out in the clean room, many defects were observed on the surface of the coating layer, as shown in **Figure 51 (a)**. It is because of many bubbles formed during mixing process or pouring final coating liquids into the petri-dish. These bubbles cause uneven coating surface, or microcracks of coating layer due to air escaping during heat-treatment. Therefore, the floating bubbles should be removed additionally after pouring the final coating liquid into the petri-dish. **Figure 51 (b)** shows a well-defined surface of coating layer when eliminating the bubbles from the surface of coating liquid.

4. Results and discussion

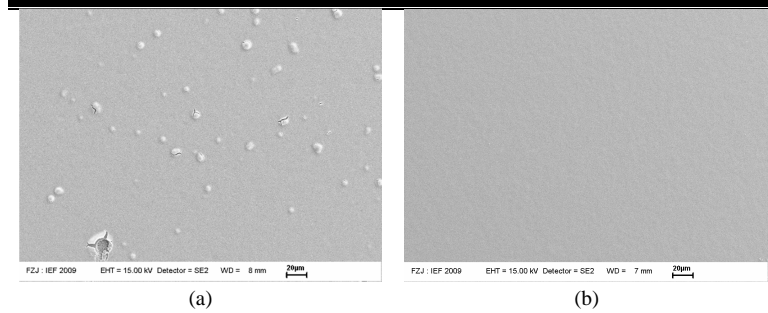


Figure 51 FEG-SEM images of NDCGO topview when the floating bubbles on the sol was not removed (a) and completely cleaned (b). A mixture of 1.0NDCGO + PVA3 was used as final sol and all layers were calcined at 500 °C for 2h in air.

Defect formation due to inhomogeneous binder distribution (Figure 52 a)

As mentioned, the pinholes formed after sintering due to the decrease in stability of nano-dispersion. The binder can also affect defect formation. For instance, inhomogeneous layer can be formed during coating procedure, when the binder is partially not dissolved in the solution during synthesis or is not dispersed homogeneously in nano-dispersion during mixing, or is re-agglomerated. As a result, the coating layer can burst during burn-out of inhomogeneous binder.

Defect formation due to rough surface of substrate (Figure 52 b)

Deep valley of substrate waviness can lead to the failure in the coating layer. If the second coating layer is deposited with loose contact to the first coating layer at the valley of substrate, the second coating can form discrete film after sintering.

Defect formation due to substrate defect (Figure 52 c)

When too large pores or defect holes already exist on the substrate surface, the nano-particles in dispersion is infiltrated into them. Thus, the desired coating layer cannot be obtained. Therefore, the condition of substrate surface is certainly critical factor for film formation.

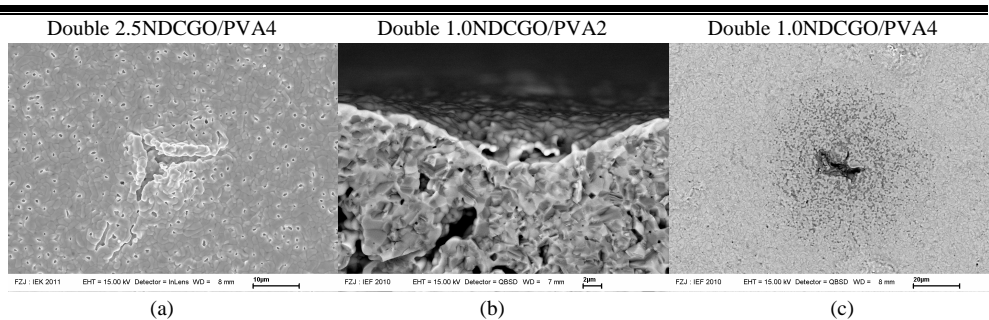


Figure 52 FEG-SEM images of possible failures of sintered CGO film formation, e.g. (a) pinholes due to the sol instability and binder burst, (b) continuous CGO layer due to the substrate valley, and (c) sol infiltration into the very large pore of the substrate.

4.3 Characterization of CGO and LSCF membrane by PVD

4.3.1 Development of interlayer

Applying additional interlayer has a considerable benefit, particularly when the reduction of pore size of substrate is required. Larger pores of substrate require longer sputtering time to be covered and thus the minimum thickness of film deposited is limited. The additional interlayer provided fine porous surface condition and enabled very thin film membrane. As a result, relatively gastight LSCF membrane (approx. 700 nm thick) could be deposited without bias assist in this work. However, the interlayer can occasionally be fatal for membrane deposition. If the interlayers are not mechanically strong enough, they are destroyed from the sputtered atoms. For instance, it was detected that the interlayers were peeled-off or eroded by sputtered CGO atoms, since they could not overcome the kinetic energy of sputtered atoms.

Table 14 shows the prepared interlayers for sputtering process. NDCGO, CSCGO and AIOOH interlayers were produced via dip-coating. PVA2 was mixed with the coating liquids as binder. Each interlayer consists of double coating layer to minimize the defect that might exist in the first coating layer. Every coating layer underwent calcination (500 °C, 2h, ± 2 K/min), followed by final heat treatment.

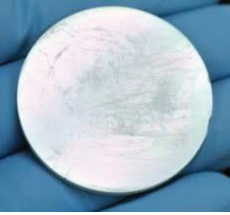
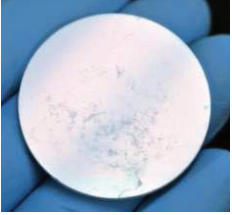
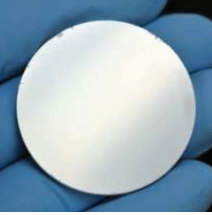
Table 14 Prepared interlayers on zirconia and alumina substrate.

Name	Coating liquid for interlayer	Substrate	Final heat treatment
50-1.0NDCGO-Z	1.0NDCGO	110-8YSZ	500 °C / 2h / ± 2 K/min
80-1.0NDCGO-Z	1.0NDCGO	110-8YSZ	800 °C / 2h / ± 2 K/min
100-1.0NDCGO-Z	1.0NDCGO	110-8YSZ	1000 °C / 2h / ± 2 K/min
110-1.0NDCGO-Z	1.0NDCGO	110-8YSZ	1100 °C / 2h / ± 2 K/min
100-1.5NDCGO-Z	1.5NDCGO	110-8YSZ	1000 °C / 2h / ± 2 K/min
50-CSCGO-CZ	CSCGO/1.0NDCGO	110-8YSZ	500 °C / 2h / ± 2 K/min
110-CSCGO-CZ	CSCGO/1.0NDCGO	110-8YSZ	1100 °C / 2h / ± 2 K/min
110-1.0NDCGO-A	1.0NDCGO	110- α Al ₂ O ₃	1100 °C / 2h / ± 2 K/min
110-A30A	CS_AIOOH	110- α Al ₂ O ₃	1100 °C / 2h / ± 2 K/min

4. Results and discussion

Before introducing samples into the PVD chamber, all samples were ultrasonically cleaned in a container filled with ethanol. This cleaning step is really critical since the defects obtained already in this step leads to defective membrane deposition. In a conventional way, the samples were laid on the bottom of glass beaker and after ultrasonication cleaning the sample surfaces were quickly dried using a cotton fabric. In this case, serious plenty of scratches were found on the sample surface at a glance, as shown in **Table 15**. Although the samples were dried using nitrogen gas instead of wiping them with a cotton fabric, the failure of interlayer was still observable. It seems that the particles escaped from the sample rolled on the sample surface and thus left rolling marks. To avoid this problem, vertical cleaning was carried out with nitrogen gas drying. The samples were kept upright in the glass beaker (non-contact mode), so the particles that affect the surface just sank down on the bottom of the glass beaker. As a result, the samples were successfully cleaned without any defect.

Table 15 Ultrasonication cleaning of substrates having interlayers.

Prepared interlayer	110-1.0NDCGO	110-1.0NDCGO	110-1.0NDCGO
Ultrasonication mode	Contact	Contact	Non-contact
Drying	Cotton fabric	Nitrogen gun	Nitrogen gun
Resulting appearance			

XRD of powder mixtures (CGO, 8YSZ, LSCF)

NDCGO interlayers are essential for LSCF membrane not only due to the reduction in pore size of substrate but also due to the incompatibility between 8YSZ and LSCF when 8YSZ is used as a substrate for LSCF membrane. **Figure 53** shows the XRD patterns of mixtures of CGO + LSCF, 8YSZ + LSCF, and 8YSZ + CGO powders. The powders were mixed at a weight ratio 1:1 and underwent solid state reaction at 1100 °C for 2h in air. 8YSZ and CGO powders were prepared, which were same powders used for substrate and for NDCGO interlayer, respectively. LSCF powder used for XRD investigation was prepared by Pechini Method. The both mixtures of 'CGO + LSCF' and '8YSZ+CGO' exhibit no impurity phase, while the powder of '8YSZ+LSCF' exhibits phase structure change of LSCF from trigonal (rhombohedral) to orthorhombic phase and two other impurities, SrZrO_3 and Fe_3O_4 . Especially SrZrO_3 phase shows relatively intense peak. It seems that the trigonal structure was distorted with decreased Sr content in LSCF due to the SrZrO_3 formation.

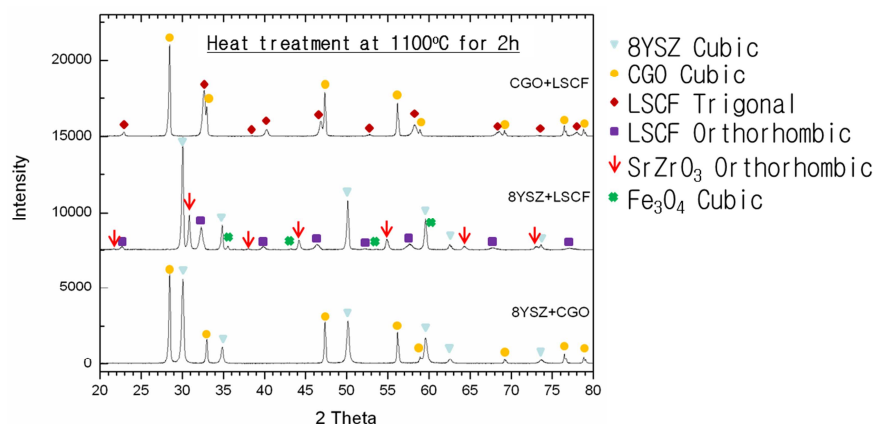


Figure 53 XRD patterns of mixtures, “CGO + LSCF”, “8YSZ + LSCF” and “8YSZ + CGO”, which underwent solid state reaction at 1100 °C for 2h in air.

SEM of NDCGO and CSCGO interlayers

Figure 54 shows SEM images of CGO interlayers. When CSCGO coating layer is deposited on NDCGO, the surface became finer. The NDCGO and CSCGO coating layers, both were double-coated, exhibits the thickness of approx. 2 μm and 0.2 μm , respectively.

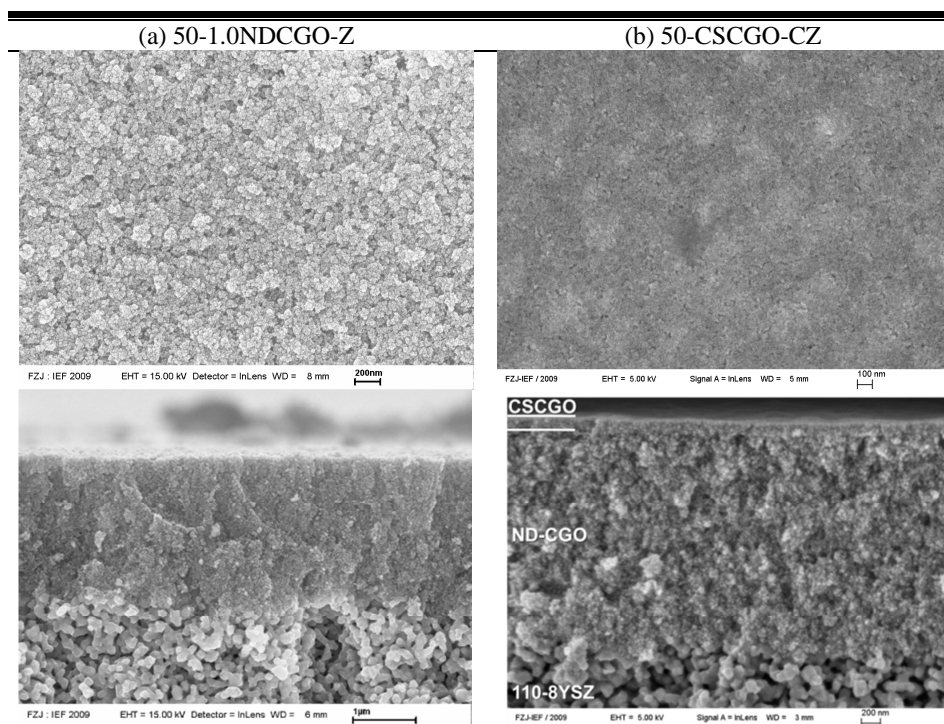


Figure 54 FEG-SEM images of surface morphology of NDCGO and CSCGO (500°C for 2h in air).

XRD of AlOOH

The AlOOH colloidal sol, which was prepared in order to produce the 110-A30A substrates, was dried overnight at 60 °C and fired at two different temperatures that are calcination temperature (500°C 2h) and final heat treating temperature (1100°C 2h). Subsequently, the obtained aluminium oxide powders were examined by XRD. **Figure 55** shows their XRD patterns. After heat-treatment at 500°C 2h in air broad and diffuse peaks were observed, presenting cubic gamma(γ)-Al₂O₃ polycrystalline. At temperature 1100 °C sharp reflections of mainly α -Al₂O₃ and a few θ -Al₂O₃ (20-25 wt.%) phases were observed. γ -Al₂O₃ undergoes phase transition ($\gamma \rightarrow \theta \rightarrow \alpha$) with increasing temperature and longer firing dwell time [93-95]. The main phase α -Al₂O₃ had a domain size of approx. 50 nm, the monoclinic θ -Al₂O₃ approx. 13 nm.

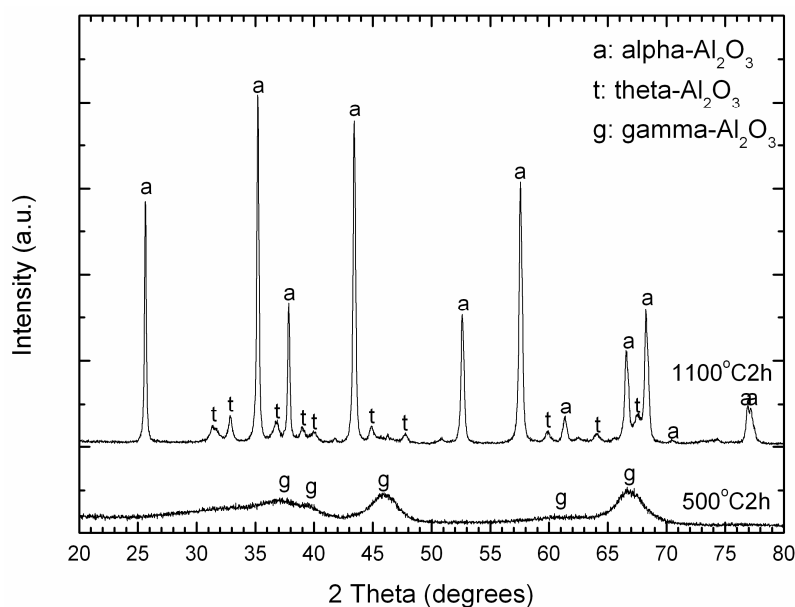


Figure 55 XRD patterns of aluminum oxide powders derived via AlOOH colloidal sol-gel route, sintered at 500°C and 1100°C for 2h in air.

4.3.2 Development of CGO membrane on 8YSZ substrate

8YSZ substrates were fabricated by vacuum-slip-casting as described in **section 3.1**. According to the pre-sintering temperature, the substrates were labelled as listed in **Table 16**. Dwell time and heating/cooling rate of pre-sintering process was kept at 2 h and ± 2 K/min, respectively, for all substrates.

Table 16 Heat-treatment profile of prepared 8YSZ substrates.

Substrate	Pre-sintering temperature	Dwell time	Heating/Cooling rate
110-8YSZ	1100 °C	2 h	± 2 K/min
112-8YSZ	1120 °C	2 h	± 2 K/min
114-8YSZ	1140 °C	2 h	± 2 K/min
118-8YSZ	1180 °C	2 h	± 2 K/min

Figure 56 shows SEM images of fracture surface of the 8YSZ substrates that were pre-sintered at four different temperatures. It is clear to see that the 8YSZ particles were coarsened gradually with increasing pre-sintering temperature, which leads to larger pore formation on the substrate surface. It should be noticed that the gas permeability of these substrates were comparable each other, i.e. there was no significant difference of gas permeability when the 8YSZ substrates were presintered at between 1100 °C and 1180 °C (see **section 4.1**).

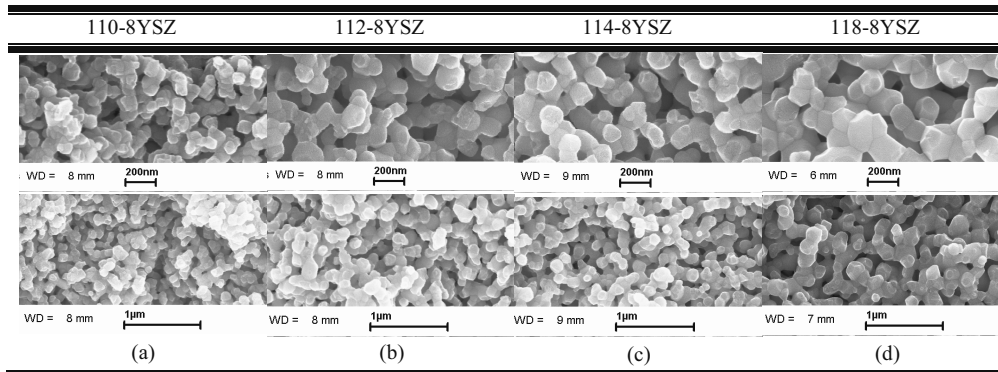


Figure 56 FEG-SEM images of fracture surface of 8YSZ substrates, presintered at 1100 °C (a), 1120 °C (b), 1140 °C (c) and 1180 °C.

4. Results and discussion

Microstructure investigation

Figure 57 shows the photographs of the sputtered membranes on 8YSZ substrates, pre-sintered at various temperatures. Without bias (0W) the CGO membranes exhibits yellowish colour on white 8YSZ substrates. With increasing bias power CGO membranes became more transparent. It should be noticed that the images with same colour box were photographed under same condition. When bias powers were used, initially white colour of the 8YSZ substrates turned out black, which is generally associated to an oxygen loss from the material. It is so-called “blackening (or darkening or coloration) of zirconia” regarding to the colour change caused by electrochemical reduction [96]. Additionally, peeling-off of CGO membrane is observable in the photographs when sputtered onto 110-8YSZ substrate with bias power 100 or 300 W. For 300W-CGO membrane supported by 110-8YSZ substrate, SEM investigation was carried out for unfavourable failure formation at the outside and at the middle of sample, as shown in **Figure 58**. The peeling-off density at the middle of sample was considerably lower than that at the outside but it was still detectable.

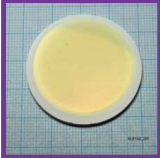
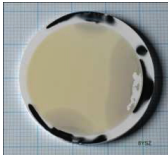

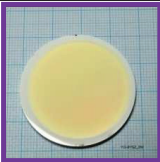








		Bias (W)				
		0 (none)	100	200	300	400
110-8YSZ				Delamination		Not suitable
112-8YSZ			-	-	-	
114-8YSZ	Porous					
118-8YSZ	Porous		Porous			

Figure 57 Photographs of RMS-CGO on 8YSZ substrates with various bias powers. Substrate temperature was kept at 800°C for all RMS runs onto 8YSZ substrates.

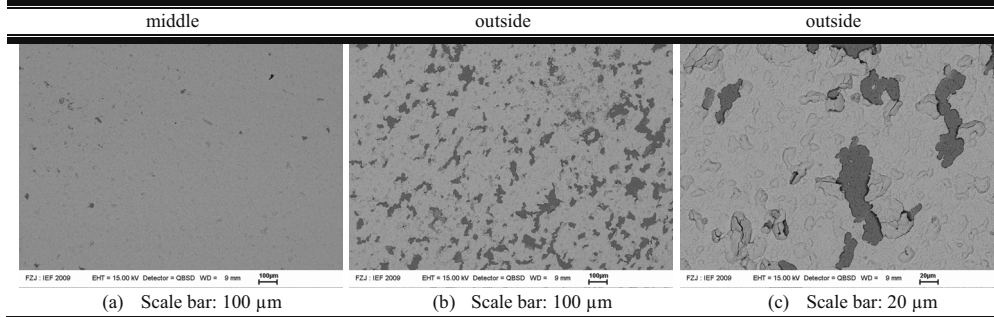


Figure 58 FEG-SEM images of RMS-CGO on 110-8YSZ with 300W bias, at the point of middle (a) and outside (b, c), i.e. blue circle areas of photograph in **Figure 57**.

Figure 59 displays the SEM images of membrane microstructures deposited on 110-8YSZ substrates when bias power 0, 100 and 300 W were applied to the substrates. 0W-CGO membrane exhibits porous and columnar structure without any defect such as delamination or peeling-off. When applying bias powers, the CGO membrane could be deposited compactly. The bias power accelerates Ar^+ -ions toward growing film and ion bombardment leads to a further densification of deposited film. However, severe delaminations were observed for both bias powers. Increasing bias power led to larger delamination curvature of CGO membrane. It is because ion bombardment to the film induces the compressive stress in the membrane. It should be noticed that the fracture of films occurred not at interface CGO membrane/substrate, but within substrate material. It indicates that the mechanical strength of substrate was not as sufficient as overcome the compressive stress. Therefore, elevated presintering temperature of substrate was adopted in order to increase the substrate strength. **Figure 60** shows SEM images of CGO membranes when deposited on 112-8YSZ. The microstructure of 0W-CGO membrane deposited on 112-8YSZ substrate was nearly similar to that on 110-8YSZ substrate, denoting that bias assist is always required to deposit the CGO membrane compactly on porous substrate. In 400W-CGO membrane supported by 112-8YSZ substrate, no severe delamination was found. The increasing presintering temperature to 1120 °C enhanced the mechanical strength of substrate, thus substrate could endure the compressive stress, achieving compact membrane without delamination. Nevertheless, some spalling was detected on the membrane surface as shown in **Figure 60 (e)**, which might be the initial stage of delamination. Therefore, the higher presintering temperatures were adopted for further development of CGO membrane.

4. Results and discussion

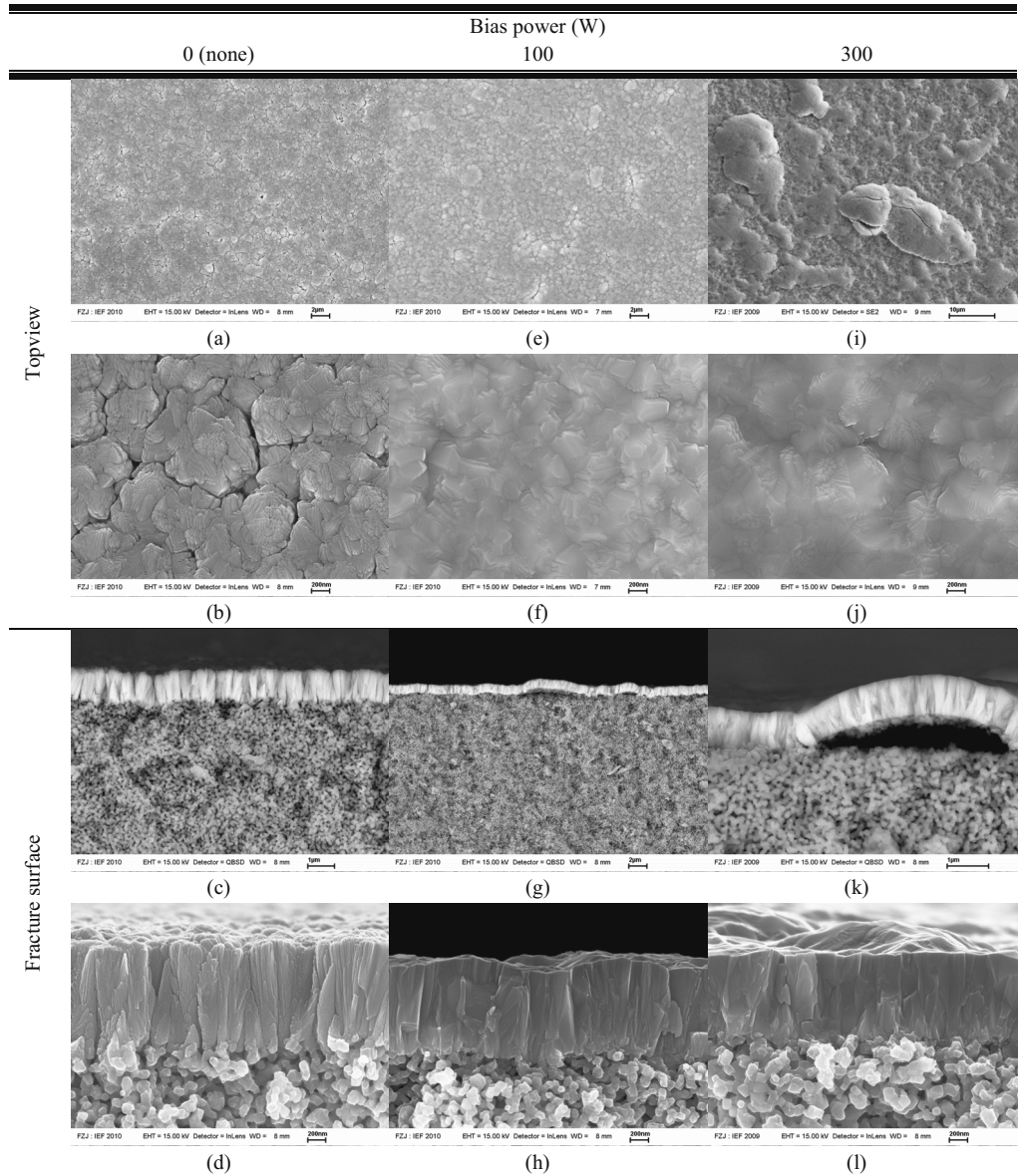


Figure S9 FEG-SEM images of RMS-CGO on 110-8YSZ with bias power 0, 100 and 300 W.
(Substrate temperature 800 °C)

*Scale bar: 200 nm for (b,d,f,h,j,l), 1 μm for (c), 2 μm for (a,e,g), and 10 μm for (i).

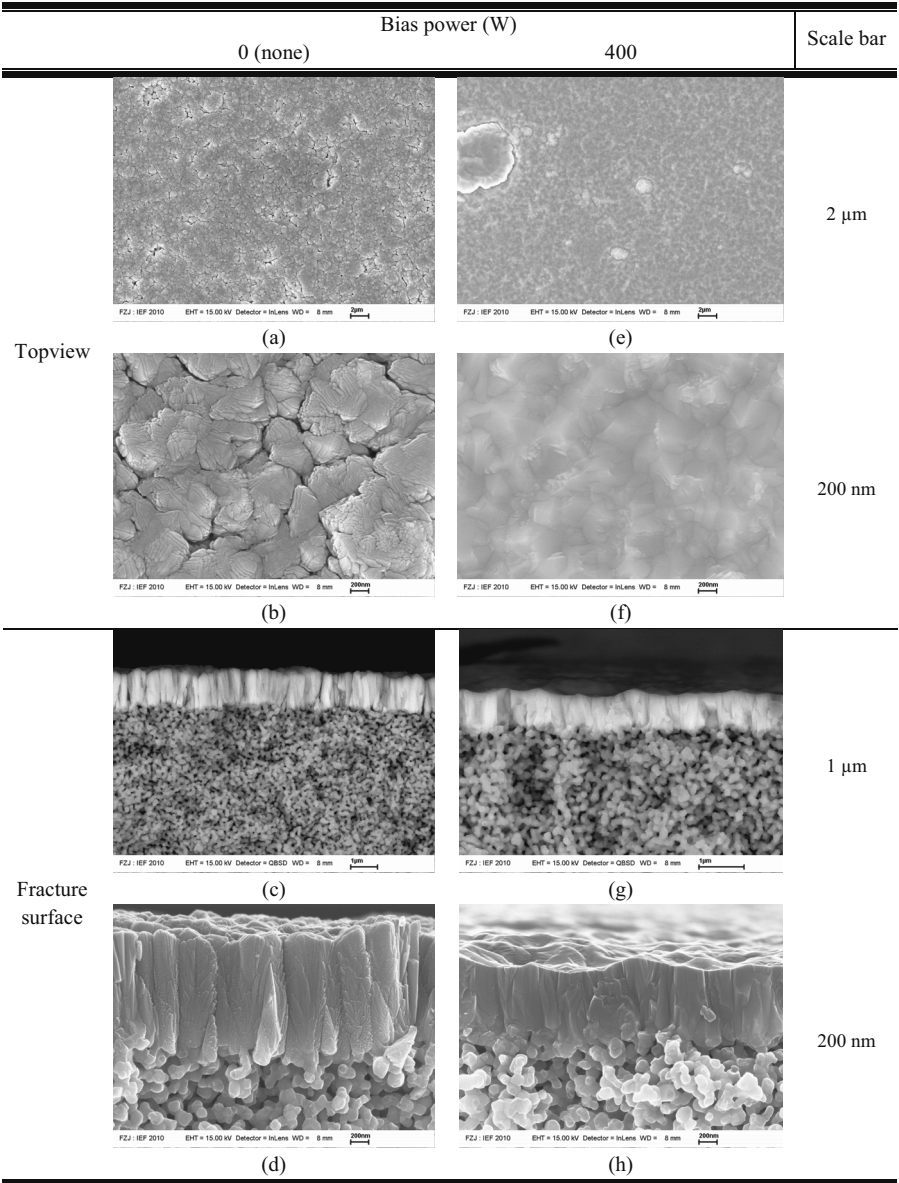


Figure 60 FEG-SEM images of RMS-CGO on 112-8YSZ with bias power 0 and 400 W.
(Substrate temperature 800 °C)

Gastightness evaluation

Figure 61 shows the single gas flow rate as a function of pressure differential [pressure on the feed side (variable) – pressure on the permeate side (1bar)]. It enables the evaluation of gastightness (or permeability) of samples. As expected with porous columnar microstructure of 0W-CGO membranes, their gas flow rates were as high as that of substrates. 400W-membranes, which were deposited on substrates pre-sintered at higher temperatures ($> 1100^{\circ}\text{C}$), exhibit significantly low gas flow rates in comparison with the substrates and 0W-membranes. Among the 400W-membranes, membrane supported by 114-8YSZ shows even lower gas flow rate than by 112-8YSZ. 100W-membrane has also lower gas flow rates than the substrates although it has delamination between CGO membrane and substrate. It was supposed that delaminated thin film was not completely peeled off so that it could have certain cover-ability on the substrate surface. The more precise evaluation of membrane gastightness is given by helium leak test as follows.

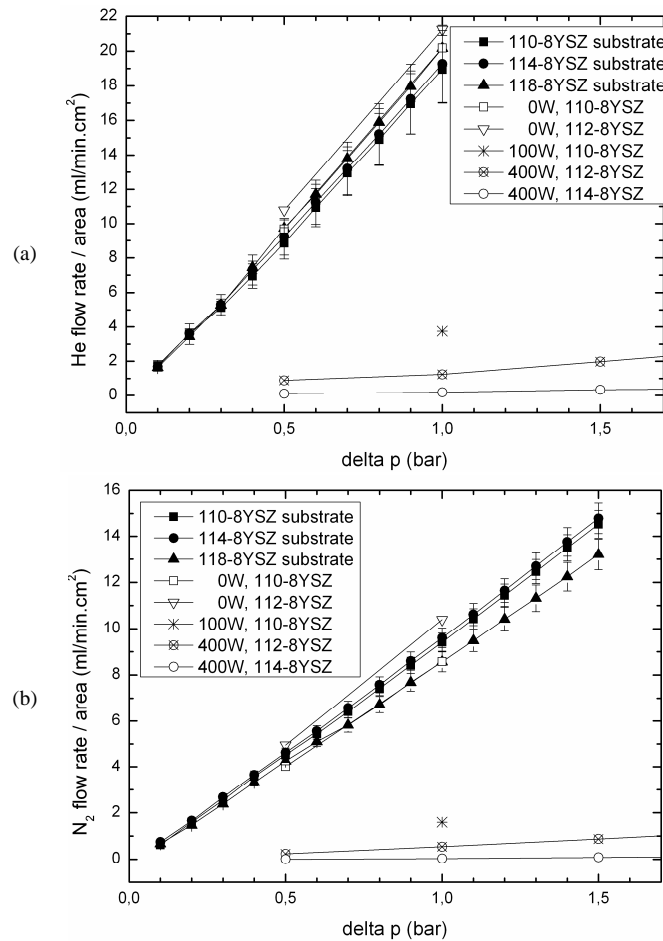


Figure 61 Gastightness evaluation by single gas permeation test using helium (a) and nitrogen (b) gases for RMS-CGO membranes deposited on 8YSZ substrates.

The CGO membranes were deposited on the 114- and 118-8YSZ substrates and various bias powers (100, 200, 300 and 400W) were applied to the substrates. Their gastightness evaluated by helium leak test is shown in **Figure 62**. With increasing bias power the helium leak rate through sputtered membranes was decreased. The lowest helium leak rate was observed in 300W-membranes. At 200 W the membranes sputtered on 118-8YSZ substrates exhibit higher helium leak rate than that on 114-8YSZ substrates.

Figure 63 shows SEM images of the microstructures of CGO membranes supported by 114-8YSZ substrates. The sputtered CGO membranes were deposited compactly on 114-8YSZ substrates when the bias powers were varied from 200 W to 400 W, while substrate bias 100W yielded porous and columnar CGO membrane. It does not correspond to the CGO membrane deposited on 110-8YSZ substrate, since dense and compact CGO membrane was observed when applying 100W bias to 110-8YSZ substrate. The coarsening of substrate particles may have been a contributing factor for this uncompact CGO membrane deposition onto 114-8YSZ substrate, because it accompanied growing pore size of substrate. Hence, the higher the pre-sintering temperature the substrates undergo, the larger minimum bias power should be applied for compact membrane deposition.

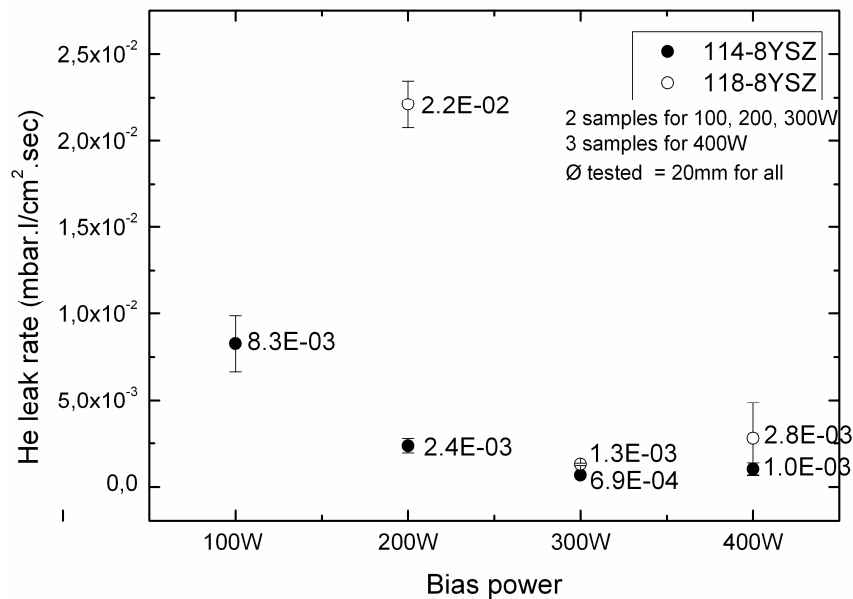


Figure 62 Gastightness evaluation of RMS-CGO membranes on 114- and 118-8YSZ substrate using helium leak test and displayed as a function of bias power applied to the substrates. He leak rates of 100W-membrane on 110-8YSZ (7.9×10^{-2} mbar.l/cm².sec) and 400W-membrane on 112-8YSZ (1.40×10^{-2} mbar.l/cm².sec) were excluded in this figure.

4. Results and discussion

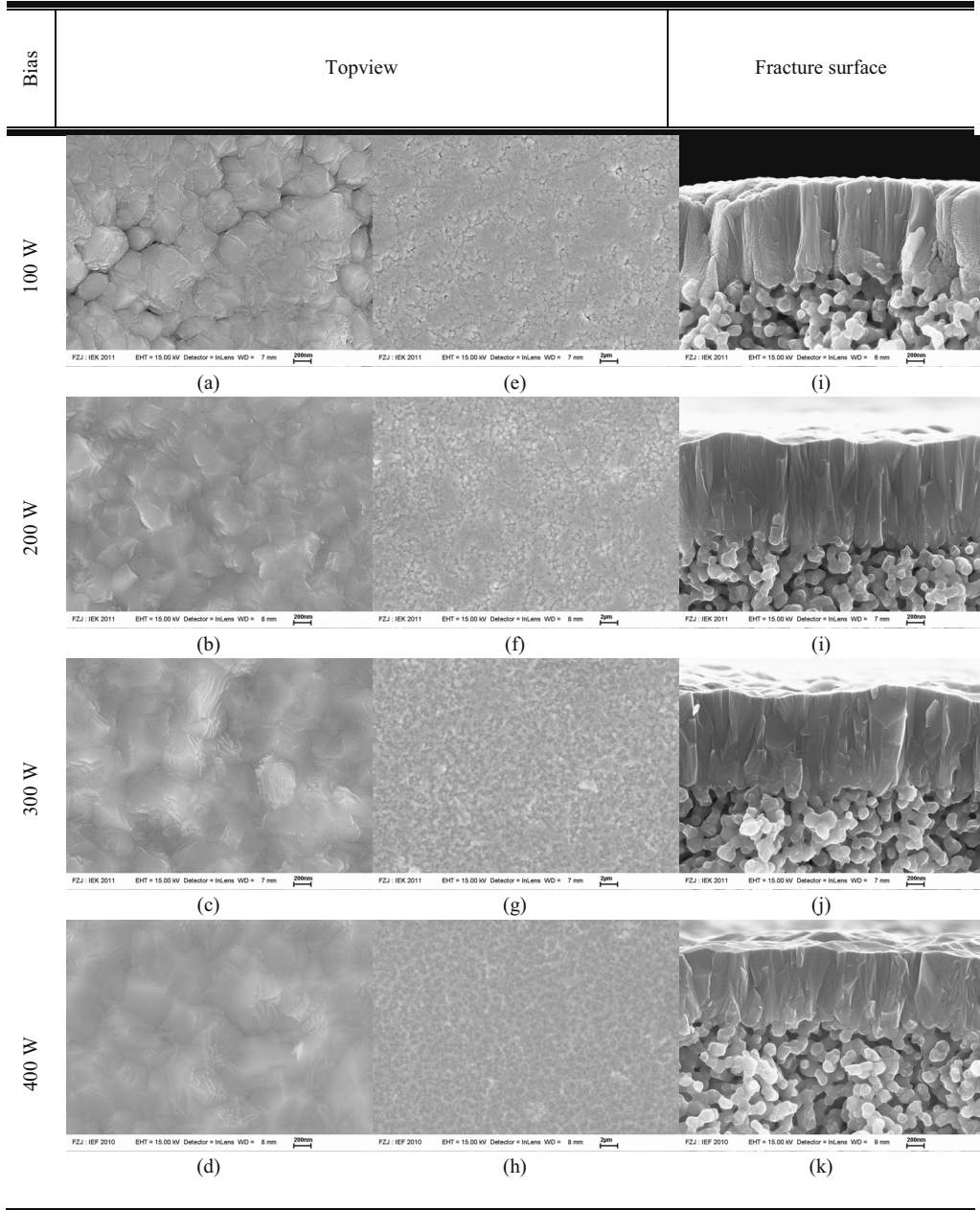


Figure 63 FEG-SEM images of RMS-CGO membranes on 114-8YSZ substrates with various bias powers.

Membrane thickness was measured using the SEM images, particularly with BSE images to distinguish the membrane clearly from the substrate with phase contrast difference. As shown in **Figure 64**, the thickness of deposited membrane was gradually reduced with increasing substrate bias. 400W-membrane reached almost 70% thick of none-biased membrane.

Four-zone-model was derived for membrane microstructure by bias-applied RMS in this work (**Figure 65**). **Zone 1**: when applying no bias or too low bias, porous thin film is deposited on the porous ceramic substrate. **Zone 2**: with increasing substrate bias, deposited thin film becomes more compact on porous ceramic substrate. However, due to the coarsening effect of substrate particle, stronger bias should be applied to obtain compact dense film when the substrate presintered at higher temperatures is used. **Zone 3**: at too higher bias, delamination of thin film occurs due to the insufficient mechanical strength of the ceramic substrate. The substrate strength can be enhanced with adopting higher presintering temperature of substrates. **Zone 4**: if the porous ceramic substrate undergoes presintering process at excessively high temperature, the substrate becomes dense, which is not suitable substrate for gas separation membrane. Therefore, proper presintering temperature is required to keep the gas permeability and, at the same time, to meet the sufficient substrate strength in order to overcome the compressive stress caused by bias assisting compact membrane formation. In this work, the substrates presintered at temperature 1100 ~ 1180 °C exhibited comparable gas permeability (see section 4.1).

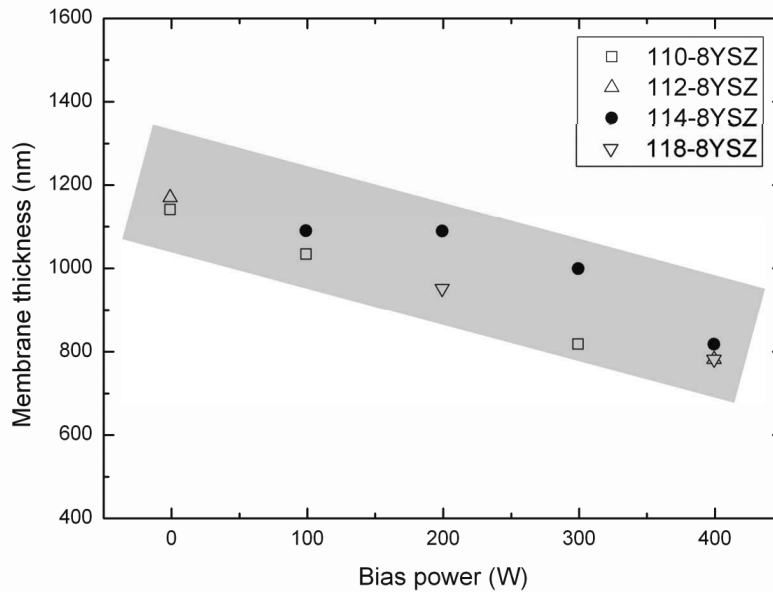


Figure 64 CGO membrane thickness as a function of bias power applied to substrate during RMS.

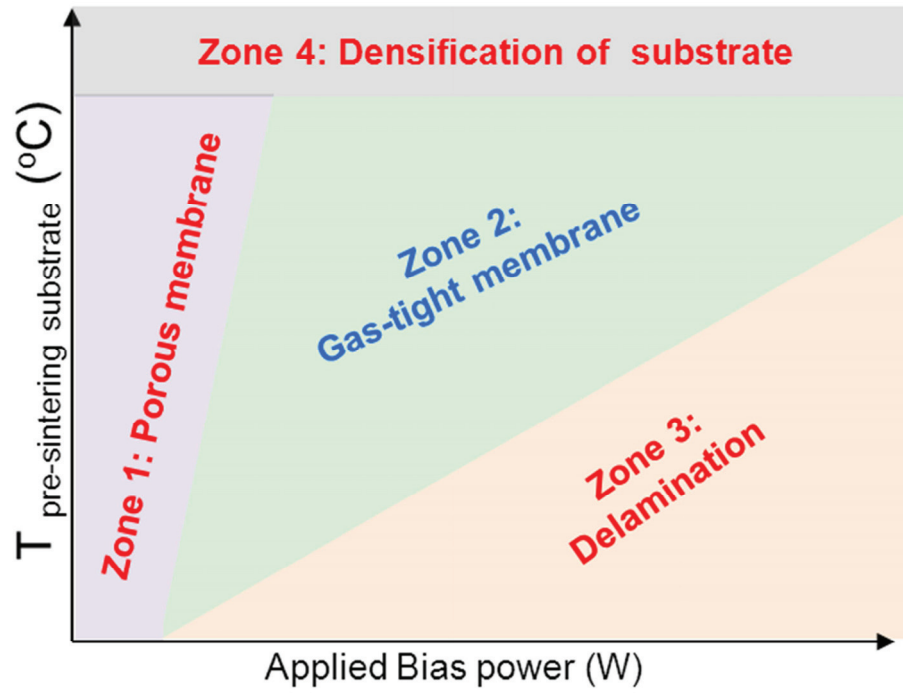


Figure 65 Derived four-zone-model for membranes in bias-applied RMS with substrate temperature 800 °C.

XRD investigation

Figure 66-68 shows XRD patterns of RMS-CGO membranes as a function of substrate bias. The sputtered CGO was deposited on 110-8YSZ, involving delamination failure (**Figure 66**), and on 114-8YSZ, forming porous microstructure at bias 100W and compact dense membrane at bias 200 – 400W (**Figure 67**). 0W-CGO membrane exhibits random orientation like CGO powder prepared using sintered CGO nano-dispersion. The domain sizes of CGO membranes deposited on 114-8YSZ substrates decrease apparently with the increase in substrate bias. It is remarkable that, as the substrate bias increases, the diffraction intensity of (220) peak increases gradually, while the other peaks show decrease of diffraction intensities. Consequently, the (220) peak is dominant at the 400W-CGO membrane. The (111) and (220) orientated peaks on CGO membrane supported by 110-8YSZ has also similar tendency as CGO membrane supported by 114-8YSZ. The (111) and (220) peaks became weaker and more intense, respectively, when the substrate bias increase from 100W to 300W. The CGO diffraction peaks on the membrane supported by 114-8YSZ substrates was shifted slightly toward the lower angle (2θ) when substrate biases were applied (**Figure 68**), indicating the compressive stress exist in the film which spreads apart the planes of atoms parallel to the substrate surface.

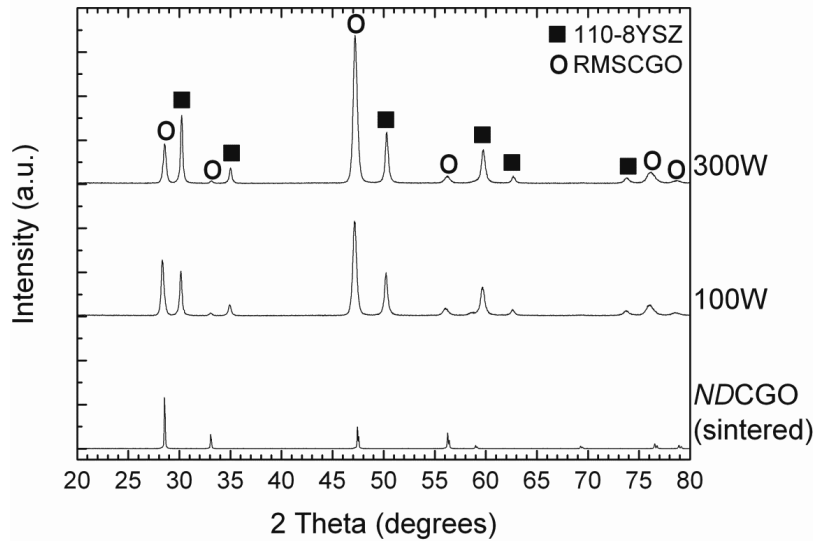


Figure 66 XRD patterns of RMS-CGO membranes as a function of substrate bias, which were deposited on 110-8YSZ substrates at substrate temperature 800 °C. XRD patterns of sintered NDCGO powder was included in for comparison.

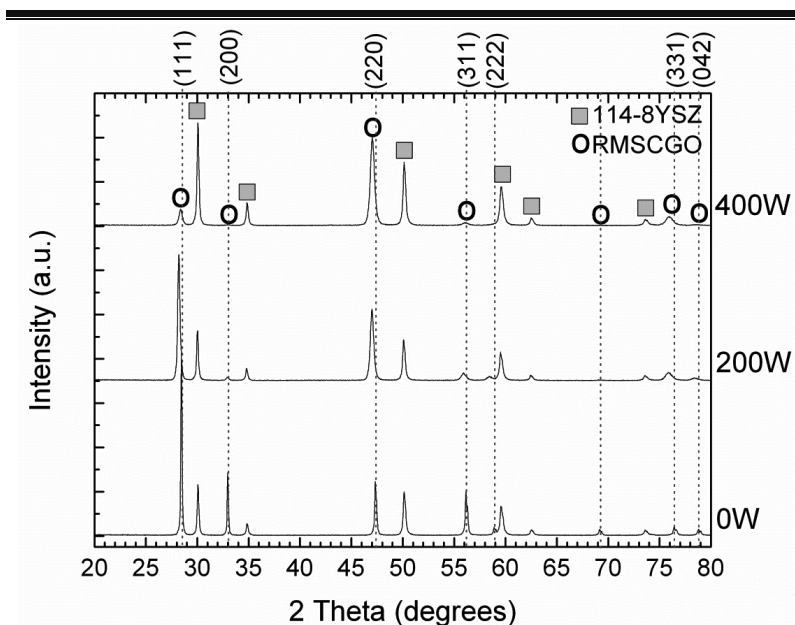


Figure 67 XRD patterns of RMS-CGO membranes as a function of substrate bias, which were deposited on 114-8YSZ substrates at substrate temperature 800 °C.

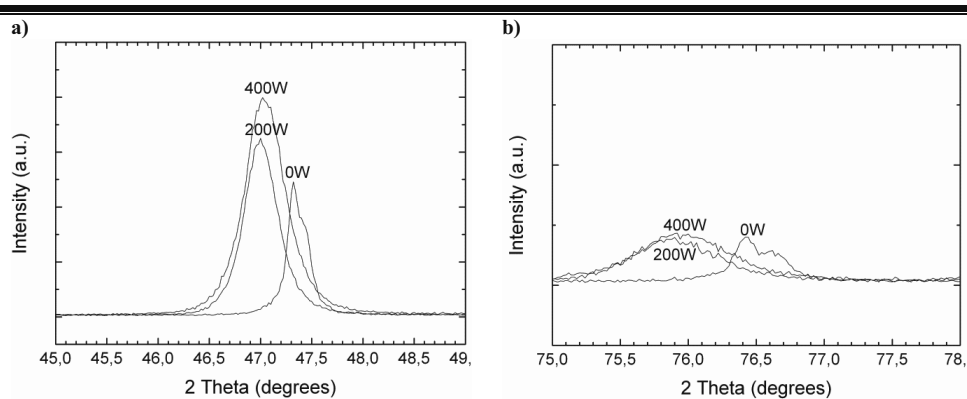


Figure 68 XRD patterns of RMS-CGO membranes as a function of substrate bias, which were deposited on 114-8YSZ substrates at substrate temperature 800 °C. **Figure 67** was magnified for observation of peak shift when substrate bias was applied.

Roughness of RMSCGO on 114-8YSZ depending on bias power

Surface roughness of ‘the substrates prior to RMS’ and ‘the sputtered CGO membranes’ was mapped by a confocal laser microscope. In order to compare the roughness before and after sputtering at the same position, the artificial scratch was made. From the top of the scratch, nine images were detected using assembly function with super high definition and pitch $0.01\ \mu\text{m}$. The assembled “laser+color” images are shown in **Figure 69**. Except for left 3 images involving the artificial scratch, the surface roughness of each image was evaluated and summarized R_a data is depicted graphically in **Figure 70**. The R_a values of the used substrates were in the mean range of 114-8YSZ substrates (R_{a-s} $0.20 - 0.27\ \mu\text{m}$). The deposited CGO membranes show the much lower surface roughness, e.g. $0.11 - 0.13\ \mu\text{m}$ for R_{a-m114} and $0.13 - 0.15\ \mu\text{m}$ for R_{a-m118} , compared to the roughness of substrates supporting membranes.

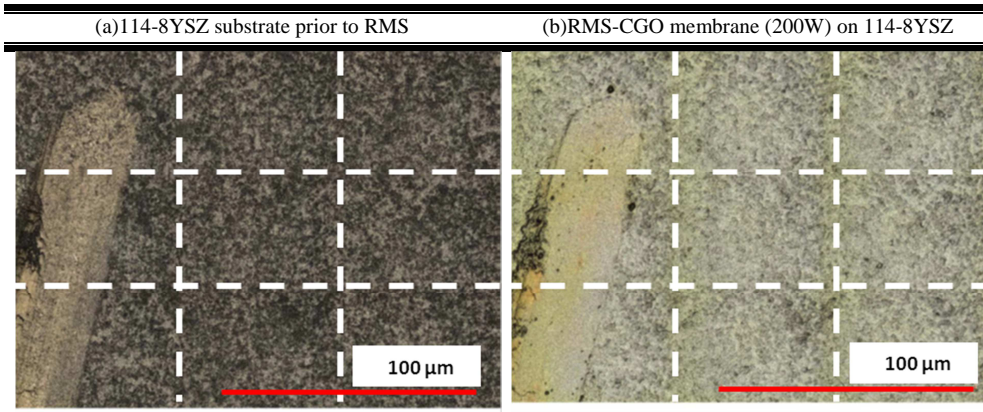


Figure 69 Laser+color image by confocal laser microscope. (a) 114-8YSZ substrate surface prior to RMS, and (b) sputtered CGO membrane with substrate bias 200W.

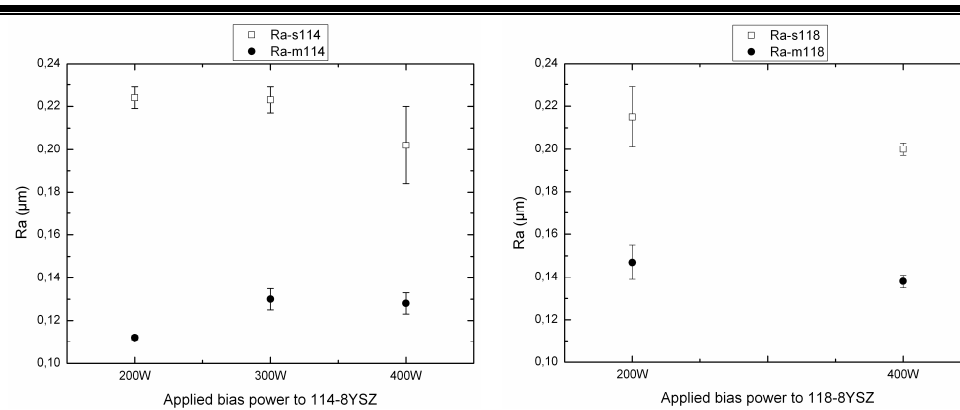


Figure 70 Surface roughness (mean R_a) of the substrate prior to RMS (R_{a-s}) and sputtered CGO membrane (R_{a-m}). The three images of left side involving scratch (in **Figure 69**) were excluded for evaluating the roughness.

4. Results and discussion

The R_a data for all CGO membranes were summarized in **Figure 71**. As expected, the surface roughness of CGO membranes supported by 110-8YSZ substrates (R_{a-m110}) enlarged with increasing substrate bias due to the state of delamination curvature. For R_{a-m110} at 300W bias, only the middle area of sample was measured. The red circle indicates the R_a values involving delamination only for deposited CGO films on 110-8YSZ substrates. The membrane surface deposited without any substrate bias exhibited a rough surface due to the columnar microstructure. Applying substrate bias leads to the smoother membrane surface due to the bombardment of Ar^+ ions and thus the surface roughness decreased. Particularly, 300 and 400W-CGO membranes show the surface roughness $R_{a-m} < 0.14 \mu m$.

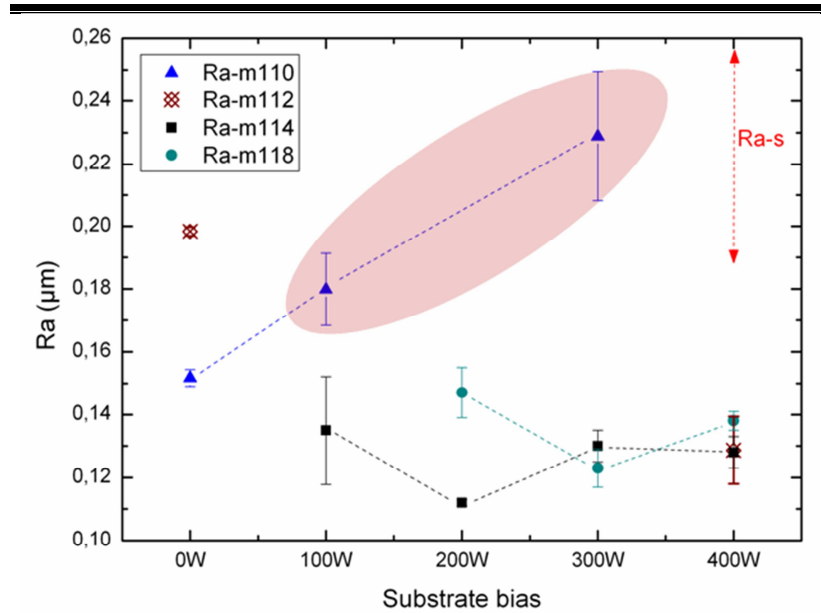


Figure 71 Surface roughness (mean R_a) of CGO membranes deposited on 110-, 112-, 114- and 118-8YSZ substrates as a function of applied bias power. R_{a-m} is the mean R_a of deposited membrane and the numbers correspond to the presintering temperature of the 8YSZ substrates supporting membranes.

4.3.3 Development of CGO membrane on NDCGO-Z substrate

NDCGO substrates were prepared using CGO nano-dispersion by dip-coating as described in **section 4.3.1**. 1.0NDCGO-Z substrate consists of double CGO interlayers supported by 110-8YSZ and underwent various presintering temperatures (500, 800 and 1000 °C for 2h). According to the presintering temperature additional number was written in front of substrate name, for instance, 50-1.0NDCGO-Z, 80-1.0NDCGO-Z and 100-1.0NDCGO-Z for 500, 800 and 1000 °C for 2h, respectively. **Figure 72** shows the photographs of samples after sputtering procedures. When the bias powers were applied to the 1.0NDCGO-Z substrates, the CGO interlayers were easily destroyed by bombardment of accelerated ions. It is associated with mechanical stability of interlayer. The failure of interlayer occurs when the interlayer is not sufficiently strong to overcome the kinetic energy of accelerated ions. All interlayers seem to have the mechanical stability at the border of sufficient and insufficient states. 300W-CGO film was deposited on 80-1.0NDCGO-Z and further investigated by SEM (**Figure 73**). The dense and prous zones were observed on the sputtered 300W-CGO film surface (a and b, SE images of topview). The sputtered CGO film has thickness of approx. 250 nm (c, SE image of fracture surface), which is much thinner than CGO films deposited on 8YSZ and $\alpha\text{Al}_2\text{O}_3$ substrates (approx. 1 μm on both). In addition, BSE image of fracture surface (d) exhibits the weak cohesion between sputtered CGO film and dip-coated NDCGO interlayer. Particularly, the second film of CGO interlayer was eroded and the thickness was half reduced during RMS procedure. 100-1.0NDCGO-Z was not destroyed when no bias was applied, but the 0W-sputtered CGO film turned out to be porous in single gas-permeation test. The blackening of 8YSZ substrate was detected as discussed in **section 4.3.2** when applying bias to 8YSZ substrates.




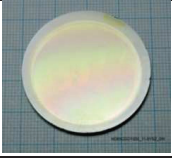

Bias (W)	0	100	300
50-1.0NDCGO-Z	-	-	
80-1.0NDCGO-Z	-		
100-1.0NDCGO-Z			-

Figure 72 Photographs of RMS-CGO on NDCGO (CGO interlayer supported by 110-8YSZ) with bias power 0, 100 and 300 W.

4. Results and discussion

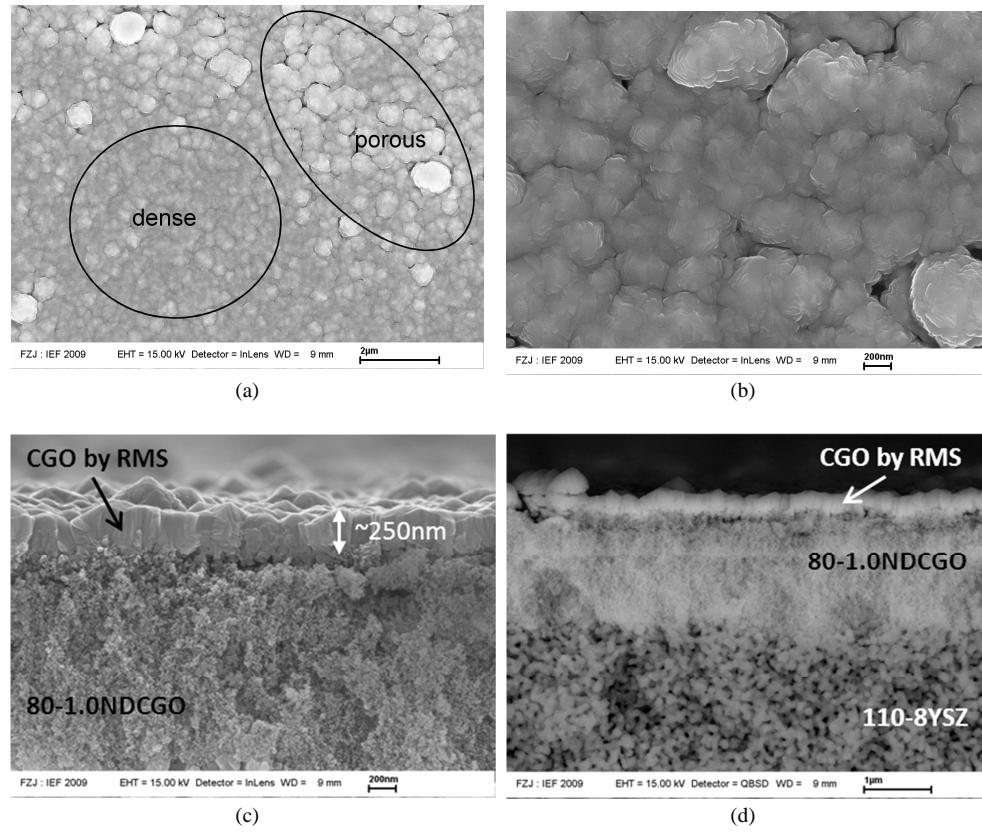


Figure 73 FEG-SEM images of RMS-CGO membrane on 80-1.0NDCGO-Z when bias power 300W was applied. (a and b: SE-topview, c: SE-fracture surface, d: BSE-fracture surface).

4.3.4 Development of CGO membrane on $\alpha\text{Al}_2\text{O}_3$ substrate

$\alpha\text{Al}_2\text{O}_3$ substrates were fabricated by vacuum-slip-casting as described in **section 3.1**. They were all pre-sintered at 1100 °C for 2h in air and called 110- $\alpha\text{Al}_2\text{O}_3$. The heating and cooling rate of pre-sintering procedure was kept at $\pm 2\text{K/min}$ for all substrates. CGO membranes were deposited onto the 110- $\alpha\text{Al}_2\text{O}_3$ substrates by reactive magnetron sputtering with various substrate bias powers in range from 0 to 400 W.

Figure 74 shows the photographs of the sputtered membranes on 110- $\alpha\text{Al}_2\text{O}_3$ substrates. The yellowish CGO membrane was deposited homogeneously when no bias power was applied. However, with increasing bias powers inhomogeneous coating behaviour was observed. Particularly, 400W-CGO membrane exhibits clearly two different colours, e.g. light yellow ring at the outside of the membrane and dark yellow circle in the middle of the membrane. The blackening of substrates and peeling-off of CGO membranes were not detected even at highest bias power (400W), differing from 8YSZ substrates as discussed in **section 4.3.2**.

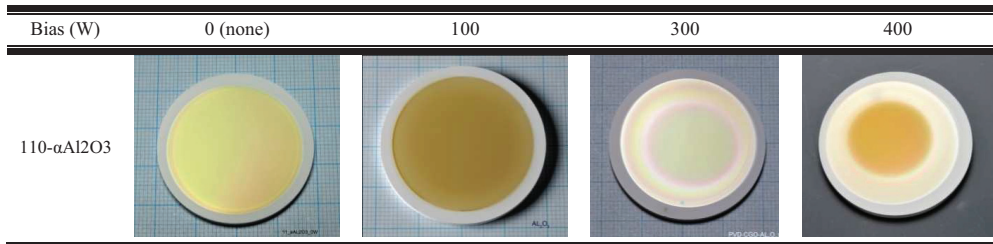


Figure 74 Photographs of RMS-CGO on 110- $\alpha\text{Al}_2\text{O}_3$ substrate when bias power 0, 100, 300 and 400 W were applied.

Microstructure investigation

SEM investigation of these samples is shown in **Figure 75**. No matter how high substrate bias, the CGO membranes remained porous and columnar structures until bias power 300 W. The fracture surface of samples were mounted and carefully polished. With BSE images of the polished fracture surface, it was verified that the CGO columns were separated from each other through whole film thickness (**Figure 76**). Two differently coloured areas in 400W-CGO membrane were separately investigated by SEM. They show different membrane structures. While very dense and compact film formed in LY (light yellow) area, very porous and dendrite-shaped microstructure was observed in DY (dark yellow) area. Moreover, approx.1.4 times thicker membrane was deposited on DY area than that on LY area. No delamination of CGO membrane was detected over whole bias range, indicating that 110- $\alpha\text{Al}_2\text{O}_3$ substrate has as sufficient mechanical strength as bias-induced stress or collision energy of argon ions can be overcome.

4. Results and discussion

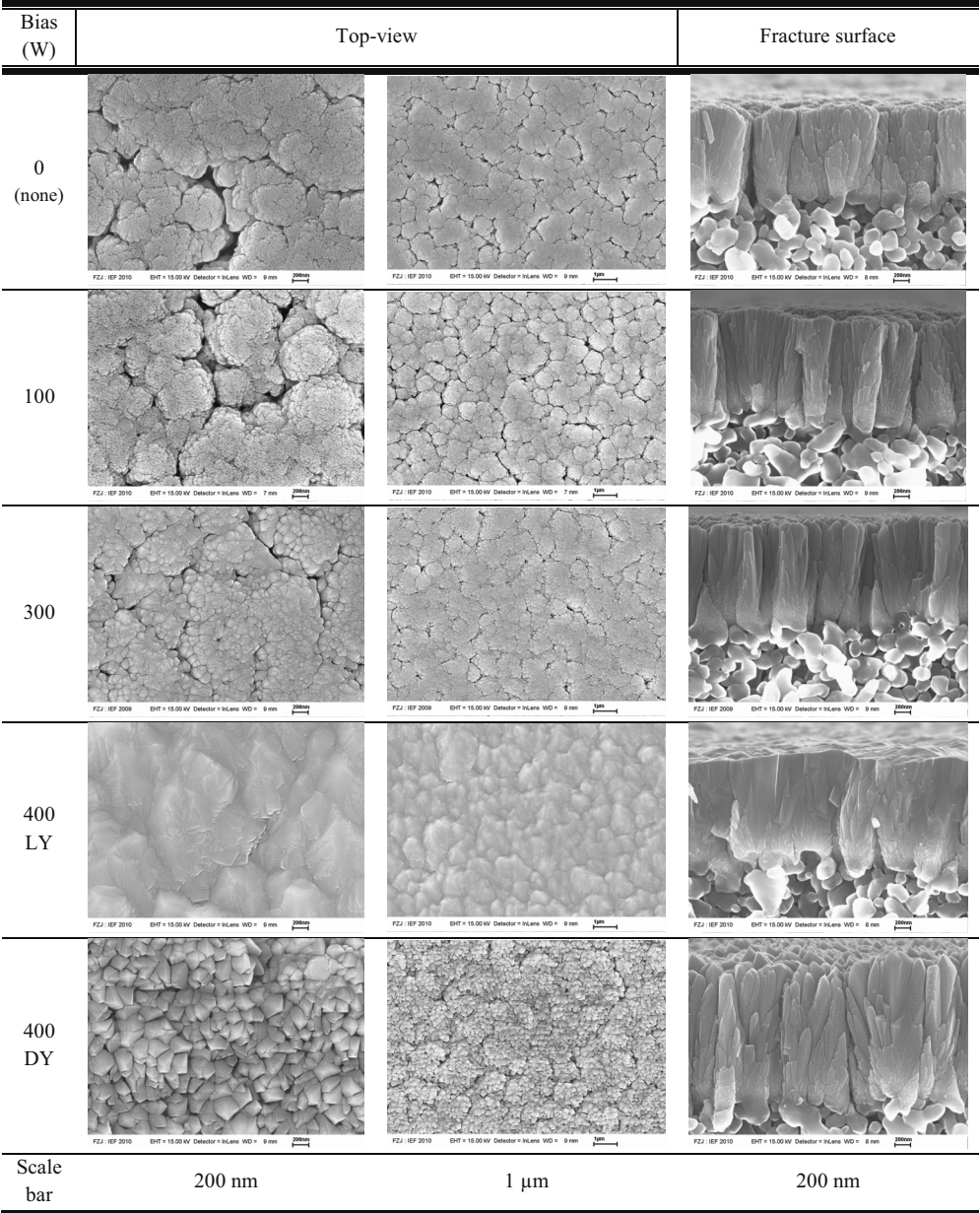


Figure 75 FEG-SEM images of RMS-CGO membranes on 110- α Al₂O₃ substrates. Bias power 0, 100, 300 and 400W were applied to the substrate during sputtering process. (LY: light yellow part (outside) and DY: dark yellow part (middle) of sample in **Figure 74** 400W)

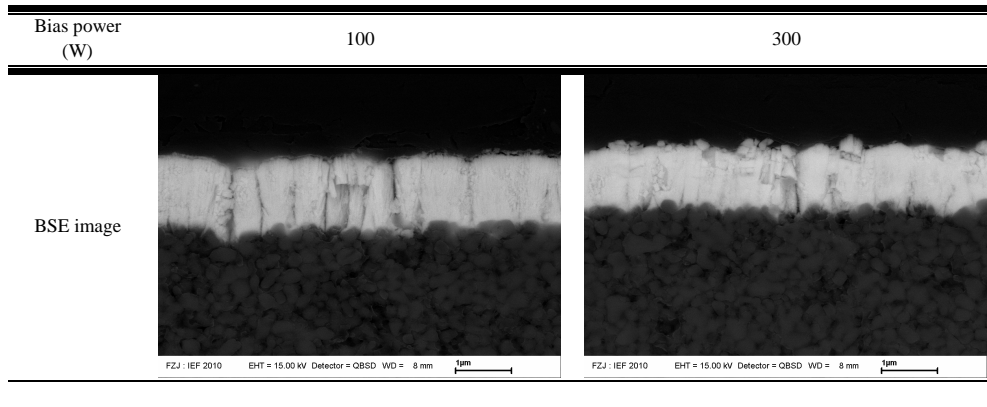


Figure 76 FEG-SEM images of RMS-CGO membranes on 110- α Al₂O₃ substrates with bias assist 100 and 300W. The broken fracture surface was mounted and polished.

For inhomogeneous deposition behaviour of CGO membrane under substrate bias, a hypothesis was suggested in this work that due to poor electrical conductivity of α Al₂O₃ substrates (Al₂O₃: $2 \times 10^{-9} \text{ ohm}^{-1}\text{cm}^{-1}$ at 700 °C [97]) that is much lower than that of 8YSZ (8YSZ: $5.5 \times 10^{-2} \text{ ohm}^{-1}\text{cm}^{-1}$ at 800 °C [98] , stabilized ZrO₂: $4.3 \times 10^{-4} \text{ ohm}^{-1}\text{cm}^{-1}$ at 700 °C [97]), the bias effect was concentrated near metallic substrate holder and thus ion bombardment was enhanced only near edge of CGO membrane. This phenomenon is called “unbalanced bias effect” in this work and it was schematically drawn in **Figure 77**.

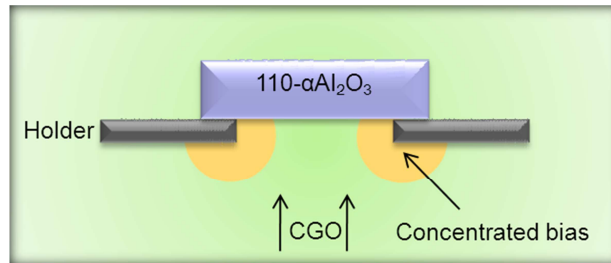


Figure 77 Schematic illustration of suggested hypothesis on inhomogeneous CGO membrane formation.

Gastightness evaluation

Figure 78 shows the single gas flow rate per measured area as a function of pressure differential [pressure on the feed side (variable) – pressure on the permeate side (1bar)]. The gastightness (or permeability) of samples can be evaluated. Except for 100W-CGO membrane, the permeability of CGO membranes exhibit as high as that of 110- α Al₂O₃ substrates, indicating all porous membranes formed. The CGO membrane could not form dense film

4. Results and discussion

without substrate bias like CGO membrane on 8YSZ substrate. Although the 100W-CGO membrane had lower gas permeability than the others, it was not enough dense to function as MIEC membrane for N_2/O_2 separation and its porous microstructure was already revealed in SEM investigation. At higher bias power (300 and 400W) unbalanced bias effect is gradually stronger and thus made more porous membrane in the middle.

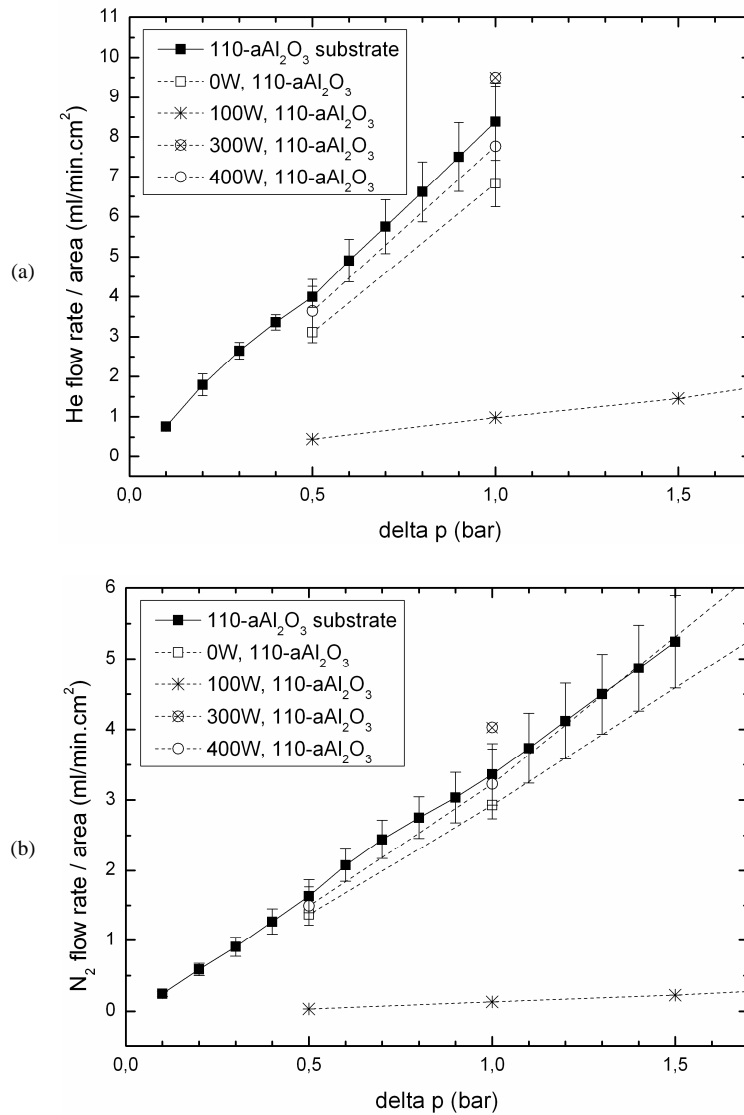


Figure 78 Gastightness evaluation by single gas permeation test using helium (a) and nitrogen (b) gases for RMS-CGO membranes deposited on α -Al₂O₃ substrates.

XRD investigation

Figure 79 shows XRD patterns of RMS-CGO membrane as a function of substrate bias, which was deposited on $\alpha\text{Al}_2\text{O}_3$ substrates exhibiting porous columnar microstructure under 0 and 100 W substrate biases. Unlike (111) or (220) preferential orientations on the CGO membranes supported by 8YSZ substrate, (200) peak was dominant for CGO membranes supported by $\alpha\text{Al}_2\text{O}_3$ substrates when 0 and 100W bias powers were applied to the $\alpha\text{Al}_2\text{O}_3$ substrates. Due to the undesired CGO deposition behaviour at higher substrate bias (300 and 400W), the XRD investigation for 300W- and 400W-CGO membranes was not carried out in this work.

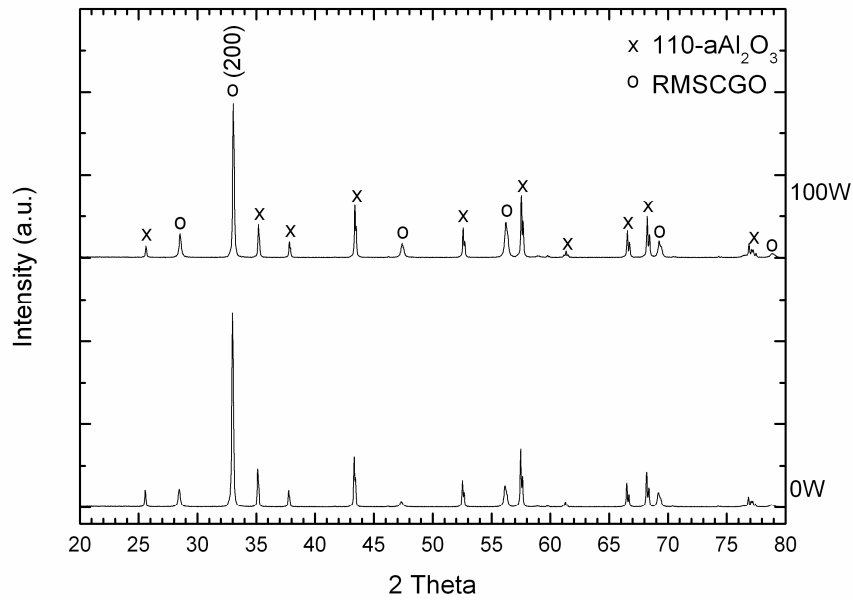


Figure 79 XRD results measured in Bragg-Brentano-Geometry for 100W-CGO membrane on $\alpha\text{Al}_2\text{O}_3$

Further heat treatment

One of the porous CGO membranes was further heat-treated at 1000 and 1200 °C with ± 2 Kmin⁻¹ for 5h in air. As shown in **Figure 80**, the CGO films with columnar microstructure began to be sintered. The CGO bundles hold together and the compacted bundles were even more separated each other at 1000 °C. Red arrow denotes the separation between the compacted bundles. At elevated temperature 1200 °C, CGO film was fully densified but severe cracks were observed over whole surface. Tensile stress causing the cracks might be derived to the CGO membrane either by shrinkage mismatch during sintering step or by thermal mismatch between CGO (TEC: $12.5 \times 10^{-6} \text{ K}^{-1}$ in IEK-1/FZJ [20] and $11.54 \pm 0.06 \times 10^{-6} \text{ K}^{-1}$ in [99]) and Al_2O_3 (TEC: $8.0 \times 10^{-6} \text{ K}^{-1}$ in IEK-1/FZJ) during cooling step.

4. Results and discussion

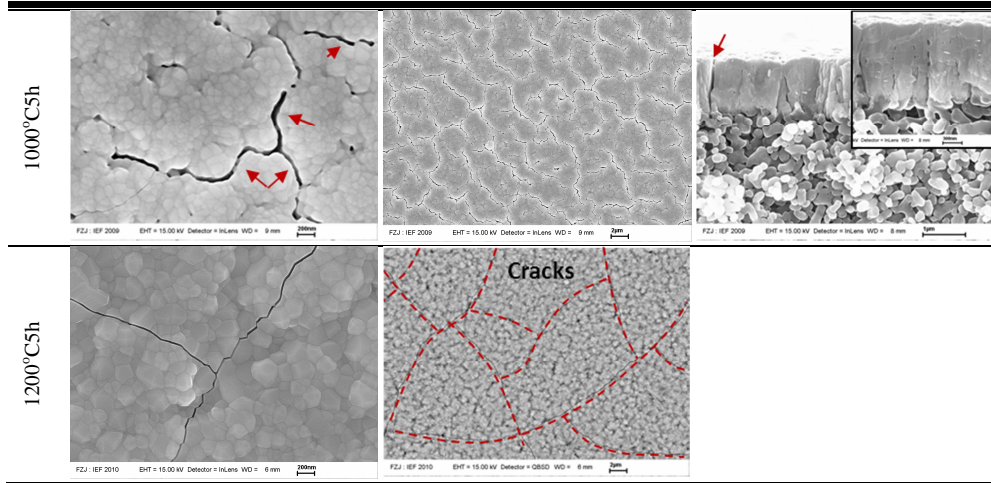


Figure 80 FEG-SEM images of 300W-CGO membrane deposited on 110- $\alpha\text{Al}_2\text{O}_3$ substrate after additional heat-treatment at 1000 °C and 1200 °C $\pm 2\text{Kmin}^{-1}$ for 5h in air.

Applying Pt-coating on alumina surface

Based on the proposed hypothesis (unbalanced bias effect), further investigation was carried out. Platinum with thickness of 4~6 nm was coated on $\alpha\text{Al}_2\text{O}_3$ substrate to increase the electric conductivity of substrate. Both uncoated and platinum-coated alumina substrates were put in the middle of sample holder next to each other. Various substrate bias powers were applied, e.g. 0, 100 and 400W. As shown in **Figure 81**, CGO film was deposited on both substrates homogeneously at 0 and 100 W bias powers, which was confirmed by SEM investigation (see **Figure 82**). At 400W ‘unbalanced bias effect’ was detected on both substrates. It seems that platinum coating did not influence the CGO deposition behaviour significantly. In SEM images of CGO film on platinum-coated alumina substrate at 400W, two different microstructures were observed between middle and outside parts of the sample. It shows the similar deposition behaviour as discussed in **Figure 75**, but slightly weaker.

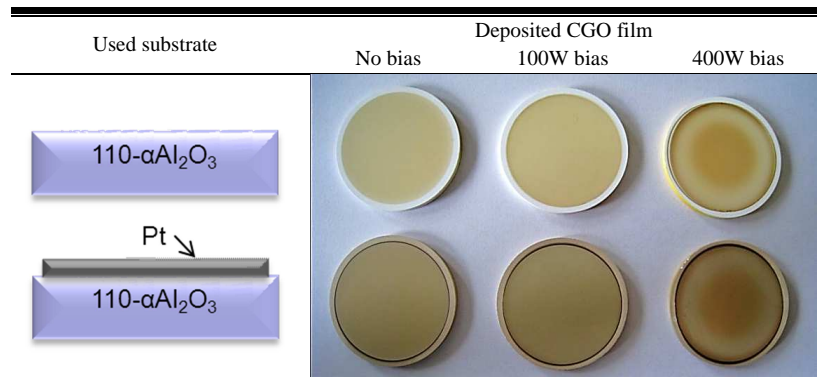


Figure 81 Photographs of deposited CGO film on uncoated and platinum-coated $\alpha\text{Al}_2\text{O}_3$.

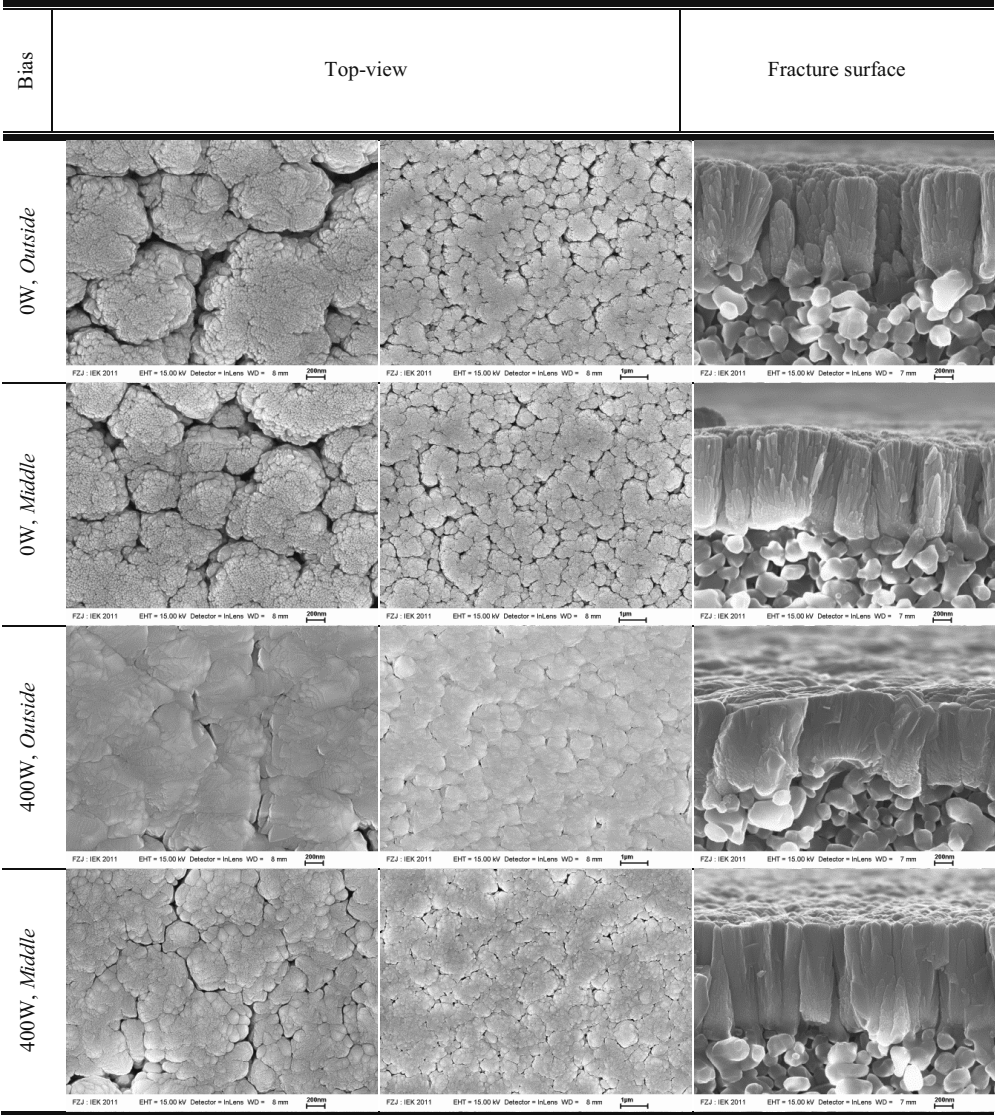


Figure 82 FEG-SEM images of RMS-CGO membranes on platinum-coated $\alpha\text{Al}_2\text{O}_3$ substrates. Bias power 0 and 400W were applied to the substrate during sputtering process. Scale bar: 200nm, 1 μm and 200nm, from left image.

4.3.5 Development of CGO membrane on A30A substrate

A30A substrates were prepared using AlOOH colloidal sol via dip-coating method as described in **section 4.3.1**. Double AlOOH interlayers were coated on 110- $\alpha\text{Al}_2\text{O}_3$ and underwent pre-sintering at 1100 °C for 2h in air, which was called 110-A30A substrate. Employing AlOOH interlayer with $d_{50} \sim 30\text{nm}$ enabled to reduce the surface pore size of 110- $\alpha\text{Al}_2\text{O}_3$ substrate. The AlOOH interlayer turned out to be $\alpha\text{Al}_2\text{O}_3$ after presintering at 1100°C as shown in XRD result of **section 4.3.1**. **Figure 83 a** shows the particle size distribution of prepared AlOOH colloidal sol for interlayer. It can be compared with $\alpha\text{Al}_2\text{O}_3$ suspension for substrate ($d_{50} \sim 700\text{ nm}$) in **section 4.1**. It is clear to see that the prepared AlOOH colloidal sol has much smaller particles with narrow distribution, which was verified once more by visual characterization of SEM images in **Figure 83 b**, displaying sputtered CGO membrane, $\alpha\text{Al}_2\text{O}_3$ interlayer and $\alpha\text{Al}_2\text{O}_3$ substrate. This CGO membrane was deposited without bias assist at substrate temperature of 800 °C and had microcracks that are discussed later in this section. The 110-A30A substrate is shown slightly lower gas permeability than the 110- $\alpha\text{Al}_2\text{O}_3$ substrate (**Figure 84**).

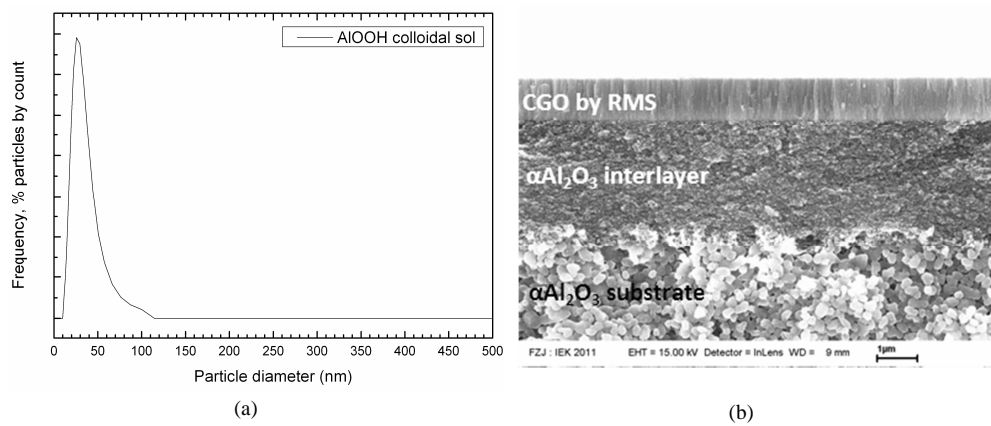


Figure 83 Particle size distribution of AlOOH colloidal sol for interlayer ($d_{50} \sim 30\text{nm}$) (a) and FEG-SEM image of their asymmetric membrane structure consisting of the sputtered CGO membrane, $\alpha\text{Al}_2\text{O}_3$ interlayer derived by CS_AlOOH dip-coating and $\alpha\text{Al}_2\text{O}_3$ support (b).

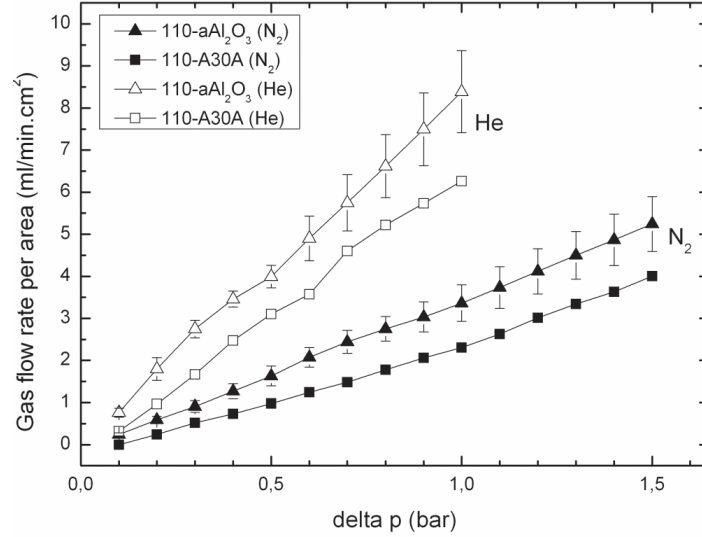


Figure 84 Gas permeability A30A substrates presintered at 1100 °C for 2h in air. Gas flow rate per measuring area is displayed as a function of pressure differential. Gas permeability of 110- α Al₂O₃ shown in **Figure 27** (a) was also displayed for comparison.

Figure 85 shows the photographs of samples appearance after sputtering procedures using bias powers 0, 100 and 400 W at substrate temperature of 800 °C or RT. All CGO membranes deposited onto the 110-A30A substrates were very shiny and homogeneous except for membrane when applying substrate bias 400 W at substrate temperature 800 °C. This 400W-CGO membrane shows well-deposited film in the middle of sample while severe delamination occurred at the outside of sample (see **Figure 86**). It is deemed the phenomenon on unbalanced bias effect caused by bias concentrated near substrate holder, as suggested in **section 4.3.4**. The interlayer could not overwhelm the concentrated high bias power and thus instead of dense and compact membrane formation the film was peeled off. In fact, the failure does occur not only in the 400W-membrane, all membranes had ubiquitous microcracks that could be observable by CLM (confocal laser microscopy) and SEM (scanning electron microscopy).

Bias power (W)	0 (none)	100	400	100
T _{substrate} (°C)	800	800	800	RT (150)
Photograph				

Figure 85 Photographs of RMS-CGO on A30A substrates with bias power 0, 100 and 400 W at 800°C and RT.

4. Results and discussion

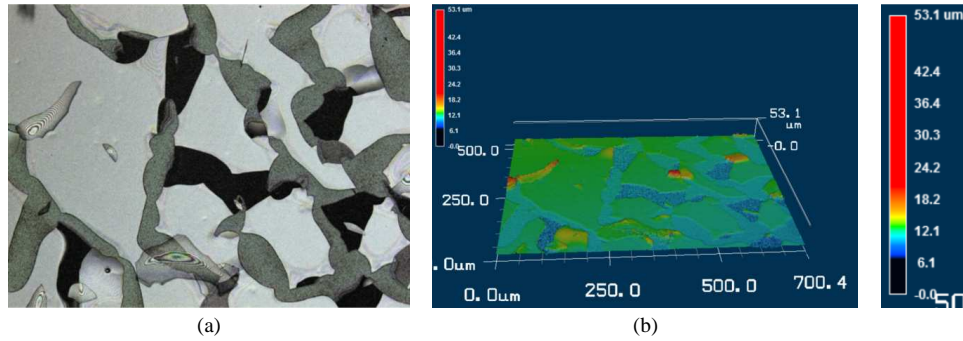


Figure 86 CLM image of outside area on RMS-CGO on A30A when bias power 400W was applied. Laser + color image (a) and height 3d-image (b).

Microstructure investigation

Figure 87 shows representative microcracks aspect. Although CGO membrane was not peeled off from the substrate, the severe microcracks existed everywhere which propagated straight (a). The microcracks were not superficial, penetrating through membrane depth completely (b). Some flower-shaped particles were observed on the membrane surface, which does not hinder the formation of sputtered membrane and just lie on the membrane surface as can be seen in (c). It was assumed that the microcracks occurred at the stage of cooling after RMS due to the larger tensile stress in the CGO membrane cause by the larger thermal mismatch between CGO (TEC: $12.5 \times 10^{-6} \text{ K}^{-1}$ in IEK-1/FZJ and [20], $11.54 \pm 0.06 \times 10^{-6} \text{ K}^{-1}$ in [99]) and Al_2O_3 (TEC: $8.0 \times 10^{-6} \text{ K}^{-1}$ in IEK-1/FZJ). For reference, TEC of 8YSZ is $10.8 \times 10^{-6} \text{ K}^{-1}$ in IEK-1/FZJ.

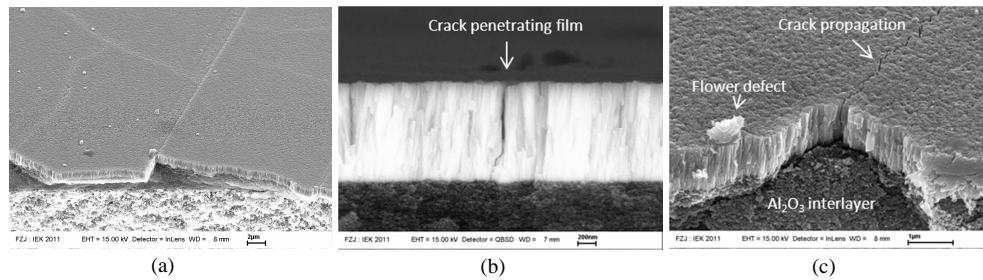


Figure 87 FEG-SEM images of microcracks in RMS-CGO on A30A biased with 100W at substrate temperature of 800 °C (SE images of tilted sample: a, c and BSE image of fracture surface: b).

Figure 88 shows the investigation of microcracks behaviour and their fracture surface by SEM depending on bias power and substrate temperature during RMS. When the substrate bias increased at substrate temperature of 800 °C, the microcrack density in CGO membrane was gradually reduced (a → d → g) but the crack width became larger (b → e → h). In addition, the CGO columns were deposited more compactly (c → f → i). In case of decrease in substrate temperature down to room temperature (RT), it helped further reduction of

4. Results and discussion

microcrack density ($d \rightarrow j$) and the microcracks blurred ($e \rightarrow k$), but the complete remove of the microcracks could not be achieved since the substrate could not sustain RT due to the plasma formation near substrate surface, providing certain temperature of approx. 150 °C. At this substrate temperature, very slender CGO columns were deposited onto A30A substrate with substrate bias 100 W (l).

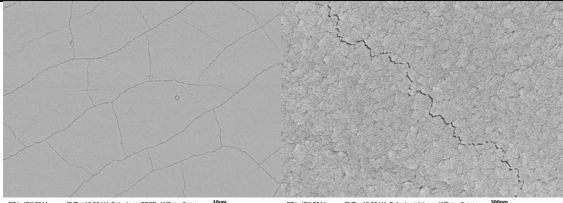
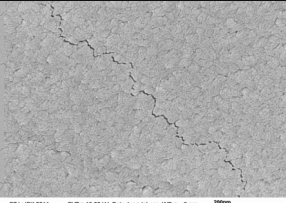
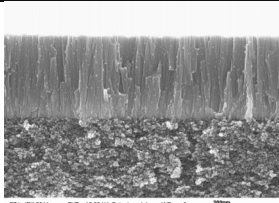
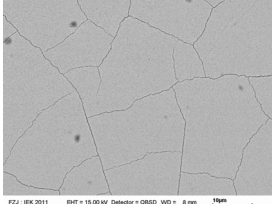
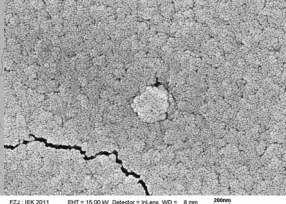
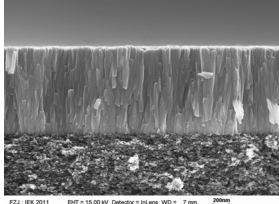
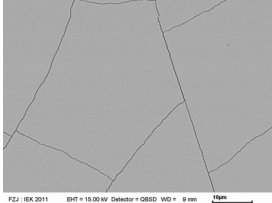
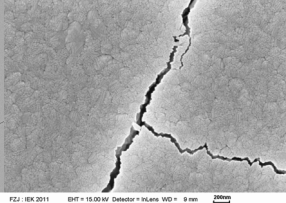
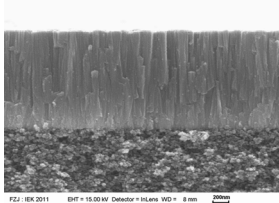
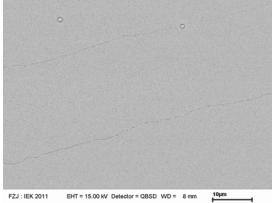
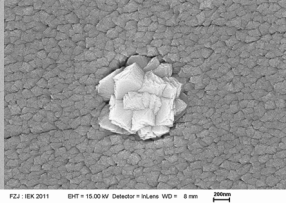
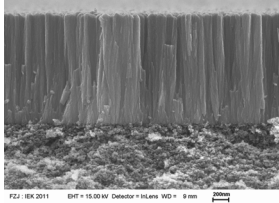
$T_{\text{sub.}}(^{\circ}\text{C})$ / Bias (W)	Top-view		Fracture surface
	Crack density	Crack width	Thickness
800/0 (none)			
	(a)	(b)	(c)
800/100			
	(d)	(e)	(f)
800/400			
	(g)	(h)	(i)
RT (150)/ 100			
	(j)	(k)	(l)
Scale bar	10 μm	200 nm	200 nm

Figure 88 FEG-SEM images of RMS-CGO on A30A. Investigation in microcracks formation depending on bias power and substrate temperature during RMS, and their membrane fracture surface.

4.3.6 Development of CGO membrane on WP/VSC (NiO/8YSZ) substrate

Coatmix substrates were prepared in IEK-1/FZJ. Its fabrication process consists of warm-pressing NiO/8YSZ support and vacuum-slip-casting NiO/8YSZ interlayer onto the support. The details are found in **section 3.1**. According to the final temperature of heat treatment for the substrate, the substrates were labelled as listed in **Table 17**. The Coatmix substrate remained porous at the presintering temperature of 1000 °C (100-WP/VSC), and relatively dense at 1400 °C (140-WP/VSC). CGO membranes were deposited onto both types of substrate without and with bias power 400W. The photographs of deposited CGO membrane onto both substrates are shown in **Figure 89**.

Table 17 Prepared WP-VSC substrates for RMS-CGO.

Substrate	Preparation
100-WP/VSC	Warm-pressed NiO/8YSZ substrate (1230°C/ 3h/ in air) with Vacuum-slip-casted NiO/8YSZ layer (1000°C/1h/ in air).
140-WP/VSC	Warm-pressed NiO/8YSZ substrate (1230°C/ 3h/ in air) with Vacuum-slip-casted NiO/8YSZ layer (1000°C/1h/ in air) was sintered at 1400°C for 5h in air at heating rate +3 K/min and cooling rate -5 K/min.

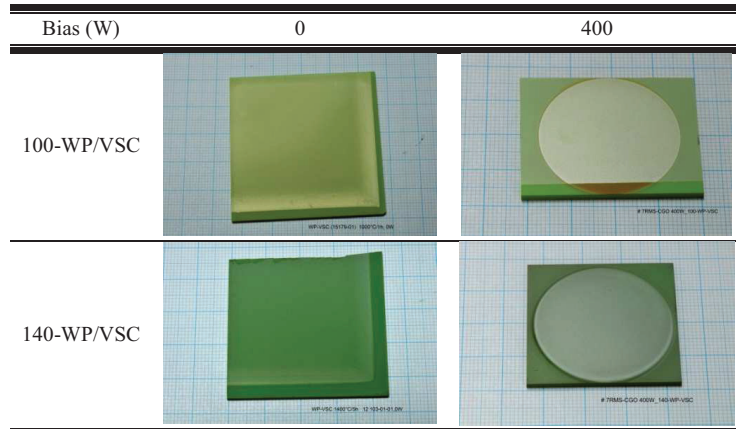


Figure 89 Photographs of RMS-CGO on 100- and 140-WP/VSC substrates without and with bias power 400W.

Microstructure investigation

Figure 90 shows SEM images of CGO microstructures on 100- and 140-WP/VSC without and with bias power 400W. When no bias was applied to the substrates, deposited CGO membrane exhibited porous and columnar microstructure on both substrates. Although the 140-WP/VSC substrate had no pores on the surface, dense CGO membrane could not be

4. Results and discussion

achieved which was, however, slightly compacter, compared with that on 100-WP/VSC substrate. The rough surface of the WP-VSC substrate may be the reason for porous membrane formation. Soro et al. [100] studied the influence of substrate roughness on deposited film structure that turned into more columnar structure with increasing roughness amplitude of substrate. In case of 400W bias power, the CGO membranes were deposited more compactly on both substrates. Some spalling defects were observed on the membrane surfaces, which might be the initial forming of delamination by high compressive stress, as discussed in previous section with CGO membranes on 8YSZ substrate (see **section 4.3.2**).

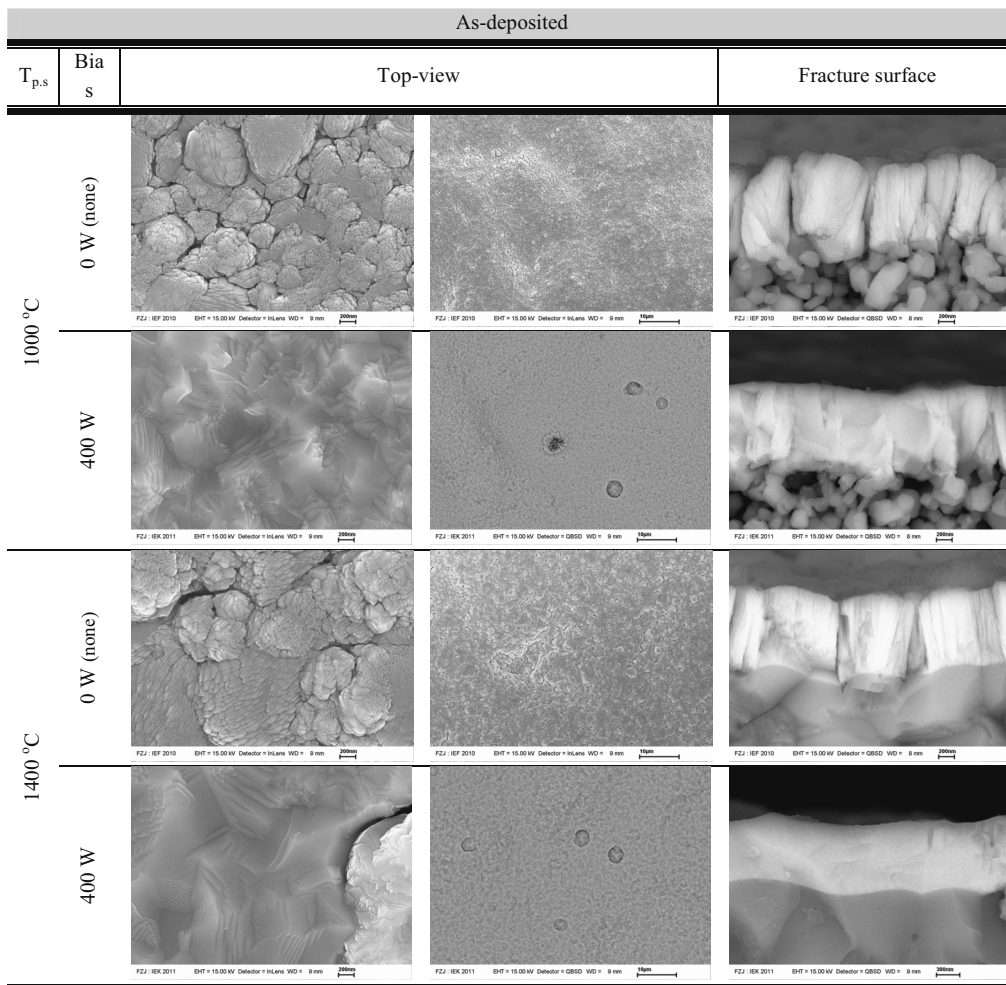


Figure 90 FEG-SEM images of sputtered CGO membrane on 100- and 140-WP-VSC substrates, when bias power 0 and 400 W were applied.

Gastightness evaluation

The gastightness of sputtered CGO membranes on 100-WP/VSC and 140-WP/VSC substrates were measured by helium leak test and evaluated as a function of the bias power, as displayed in **Figure 91**. Single sample was tested for each measurement. The deposited CGO thin films show the He leak rates, below 1.5×10^{-3} mbar·l/sec·cm² and 1.4×10^{-2} mbar·l/sec·cm² when supported by 140-WP/VSC and 100-WP/VSC substrate, respectively. Compared to 140-WP/VSC substrate (1.6×10^{-2} mbar·l/sec·cm², **Figure 49**), the CGO membranes deposited on 140-WP/VSC exhibits more than factor 10 lower He leak rate.

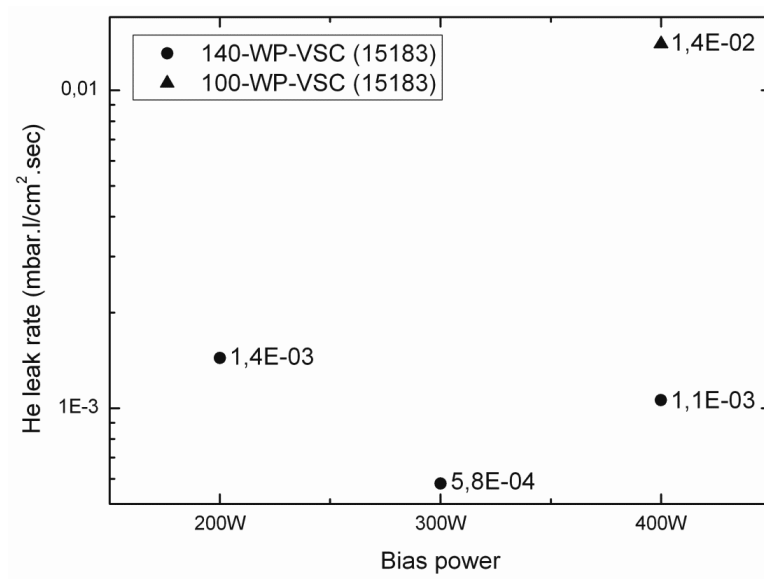


Figure 91 Gas-tightness estimation by He-leak test
(diameter of measuring area $\phi_{\text{Measured, 200\&300W}} = 20\text{mm}$, $\phi_{\text{Measured, 400W}} = 10\text{mm}$)

Microstructural change under atmosphere Ar/4%H₂

The 400W-CGO membranes on both 100- and 140-WP/VSC substrates were fired at 900°C for 3 hours under atmosphere using Ar/4%H₂ to 1) supply sufficient porosity in densified 140-WP/VSC substrate and to 2) pre-investigate phenomena for operating under reducing atmosphere.

Figure 92 shows their images of photograph and SEM. Severe delamination (b, c) and cracks penetrating through whole membrane depth (d, e, f) occurred in CGO membrane on 100- and 140-WP/VSC substrate, respectively. The delamination of CGO membrane on 100-WP/VSC substrate was already recognizable at a glance (a). From the form of membrane deformation it

can be supposed that compressive stress was generated in the CGO membranes on both substrates under reducing atmosphere. Reduction of nickel oxide to nickel metal leads to pore formation (porosity 44 ± 1 Vol.% [3]) and to volume contraction [101]. The CGO expands under reducing atmosphere [102], in contrast to NiO/YSZ, which is attributed to the reduction of CeO_2 in the fluorite structure into $\text{CeO}_{1.5}$ in the hexagonal structure ($\text{CeO}_2 \rightarrow \text{CeO}_{1.5} + \frac{1}{2}\text{O}_2$). Partially reduced CeO_2 ($\text{CeO}_{2-\delta}$) is stable in the cubic structure up to $\delta \sim 0.4$ [103] and exhibits larger lattice parameter, e.g. $\text{CeO}_{1.66}$ and $\text{CeO}_{1.68}$ have a cubic superstructure with the lattice parameter 2 times larger than that of CeO_2 [104]. Consequently, this different behaviour between CGO membrane and WP/VSC (NiO/8YSZ) substrate created the large compressive stress to the CGO membrane, leading to the delamination and cracks. In addition, **Figure 92 (c)** shows that the substrate was separated when delamination occurred, indicating the 100-WP/VSC substrate strength was insufficient.

After reducing the 400W-CGO membrane supported by 140-WP/VSC substrate, nickel was detected on the CGO membrane surface, as shown in **Figure 93**. However, it was not visible in reduced CGO membrane on 100-WP/VSC. The nickel was formed only around the spalling defect (see **Figure 93 a**). It might be concerned with the oxygen path way that was formed regarding as $\text{NiO} \rightarrow \text{Ni} + 0.5\text{O}_2$. The samples were put on the SiC plates during the heat treatment under reducing atmosphere. While 100-WP/VSC has enough path way due to its primary porous structure, the generated oxygen had difficulty to travel through primary dense structure in the dense 140-WP/VSC substrate. Therefore, oxygen was released through interface between ‘spalling defect and CGO membrane’ where was not tolerant to vapor pressure.

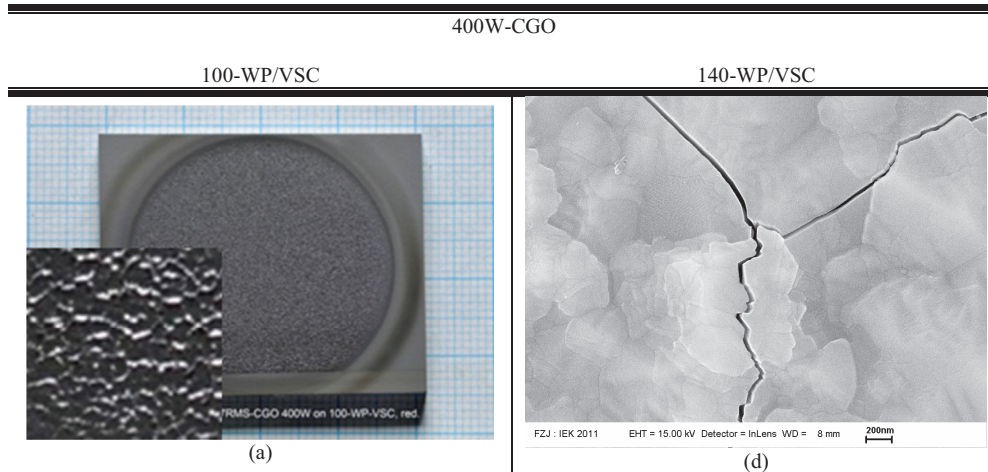


Figure 92 Images of sputtered CGO membrane after heat treatment at 900°C for 3h under reducing atmosphere using $\text{Ar}/4\%\text{H}_2$. (a: photograph, c: image by SEM-HITACHI, and the others by FEG-SEM) – (a, b, d): Top-view, (e, f): fracture surface, (c): polished cross-section.

4. Results and discussion

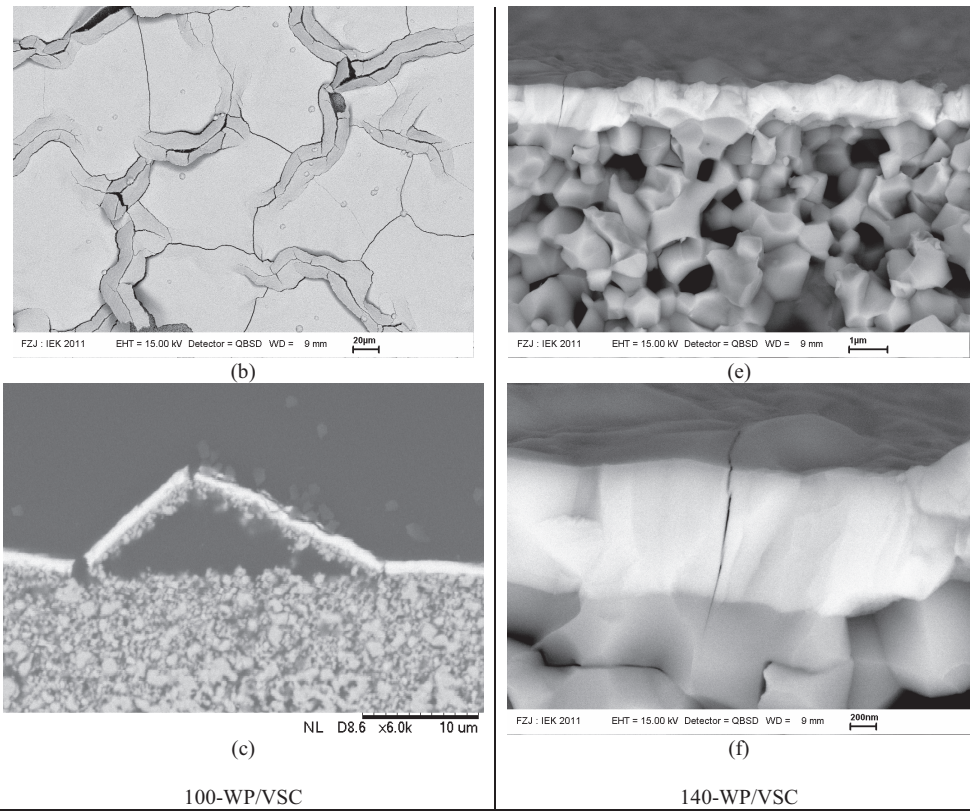


Figure 92 (continued)

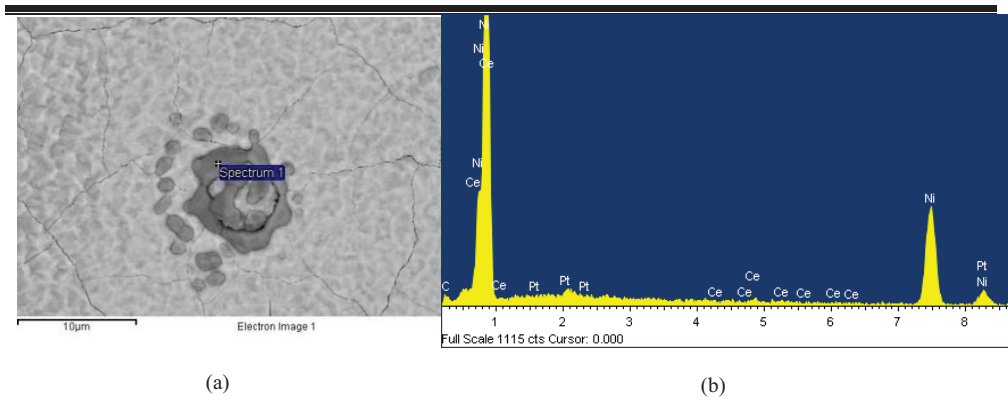


Figure 93 BSE image by FEG-SEM (a) and EDX result (b) at the point of spectrum 1 in BSE image for reduced CGO membrane on 140-WP/VSC substrate.

4.3.7 Development of LSCF membrane on 8YSZ and NDCGO-Z or -A substrates

110-8YSZ substrate (8 mol% Y_2O_3 stabilized ZrO_2 , pre-sintered at 1100°C for 2h in air), *NDCGO-Z or -A substrates* (nano-dispersion route derived CGO supported by 8YSZ or $\alpha\text{Al}_2\text{O}_3$, calcined at 1000°C or 1100°C for 2h in air), were prepared for LSCF membrane. LSCF membrane was deposited by using dc magnetron sputtering (dcMS). For LSCF membrane, BIAS was not applied to the substrates in this work.

Figure 94 shows the photographs of deposited MS-LSCF membrane on (a) 110-8YSZ, (b) 100-1.0NDCGO-Z, (c) 100-CSCGO-CZ, and (d) 100-1.0NDCGO-A. Failure such as delamination or peeling-off of the LSCF layer was visible on substrate type (d) only. All other substrate types resulted in homogeneous coatings. After increasing presintering temperature of substrate (d) up to 1100°C , the failure was not visible any more.

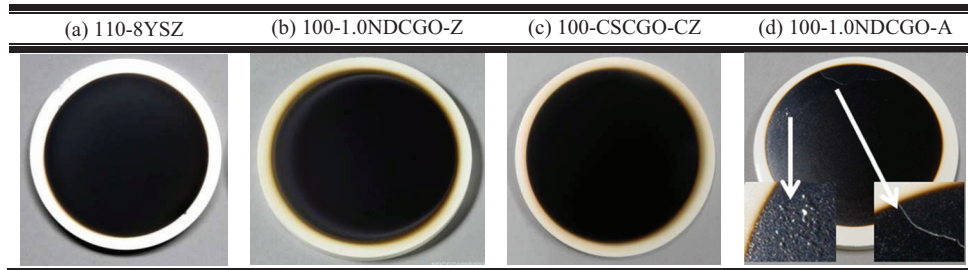


Figure 94 Photographs of dcMS-LSCF membrane deposited on 8YSZ (a), 1.0NDCGO/110-8YSZ $1000^\circ\text{C}2\text{h}$ (b), CSCGO/1.0NDCGO/110-8YSZ $1000^\circ\text{C}2\text{h}$ (c) and 1.0NDCGO/110- $\alpha\text{Al}_2\text{O}_3$ $1000^\circ\text{C}2\text{h}$ (d). MS-LSCF, CGO, 110-8YSZ and 110- $\alpha\text{Al}_2\text{O}_3$ exhibit black, yellowish, white and white color, respectively (diameter of base substrate, 8YSZ, is 39 mm).

Microstructure investigation

Figure 95 shows SEM images of deposited MS-LSCF membrane on 110-8YSZ (left) and 100-1.0NDCGO-Z (right). LSCF grains were observed in topview-SE images of both LSCF membranes (a, b, c, d). The pores were clearly visible in LSCF membrane supported by 110-8YSZ substrate and even with lower magnification large pores were still observable (a, c), while LSCF membrane was deposited tightly on the 100-1.0NDCGO-Z substrate (b, d). Both LSCF membranes have thickness of approx. 700 nm (see the fracture surface images d, f, g, h). In addition, from BSE image (g, h) of LSCF membrane, porous CGO interlayer and porous 8YSZ support could be distinguished obviously.

4. Results and discussion

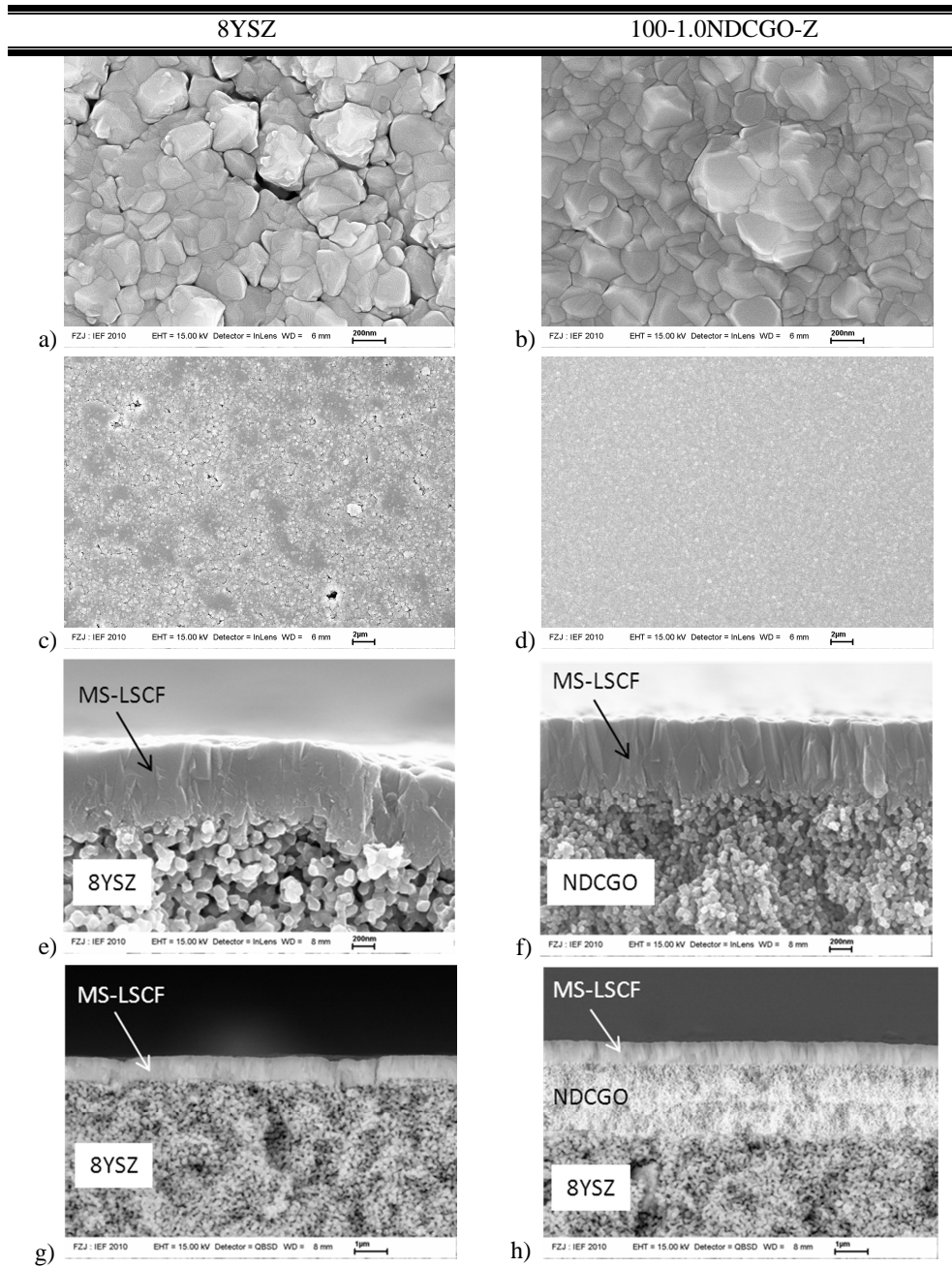


Figure 95 FEG-SEM images of dcMS-LSCF membrane on 110-8YSZ (left) and on 100-1.0NDCGO-Z (right). Topview: a,b,c,d (all SE) and fracture surface: e,f (SE) and g,h(BSE).

XRD investigation

The sputtered LSCF membrane deposited on 110-8YSZ substrate was investigated by XRD in Bragg-Brentano-Geometry, **Figure 96**. The single phase of LSCF film was confirmed with desired cubic perovskite structure with lattice parameter $a=3.910(1)$ Å. Other phases was not detected except for 8YSZ substrate material.

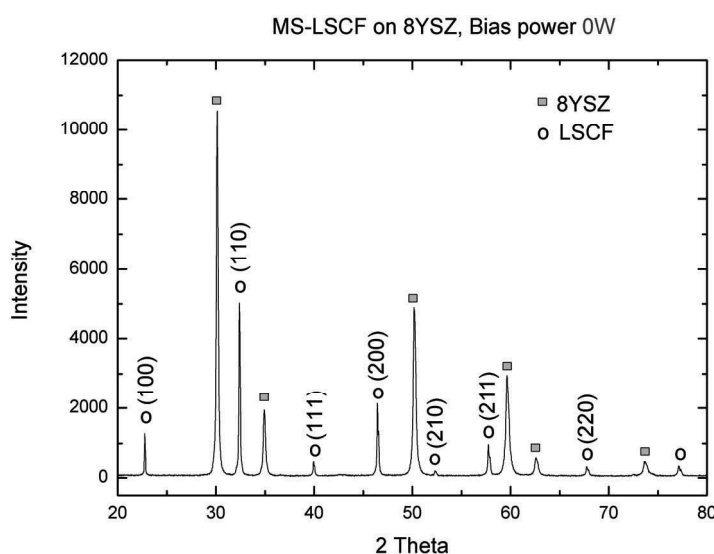


Figure 96 XRD results measured in Bragg-Brentano-Geometry for dcMS-LSCF membrane deposited on 110-8YSZ without bias assist.

Chemical analysis

The chemical analysis was carried out for the LSCF powder and dcMS-LSCF membrane supported by Si-wafer and 110-8YSZ using ICP-OES. The stoichiometry was calculated as shown in **Table 18**. Sample **I** is the LSCF powder prepared by Spray pyrolysis, which was used for the sputtering target. Sample **II** and **III** is the LSCF membranes deposited on Si-wafer and sample **IV** is the LSCF membrane deposited on 110-8YSZ. The dcMS-LSCF membrane (sample IV) show tendencies in La depletion and Fe enrichment leading to cation ratio $A/B = 0.89$ instead of unity. However, second phases could be seen neither in SEM nor in XRD. Samples showed irregularities in the stoichiometry, although the target material had the desired composition. Weiler [105] investigated that the stoichiometry varied with sample position, which may be influenced by magnetic field of the magnetron.

4. Results and discussion

Table 18 Calculated stoichiometry of LSCF powder and dcMS-LSCF films.

Analysed materials	Method	Stoichiometry				
		La	Sr	Co	Fe	O
Desired LSCF membrane	-	0.58	0.40	0.20	0.80	3
I LSCF-oxide powder [106]	ICP-OES	0.59	0.41	0.19	0.79	3
II LSCF-oxide on Si-wafer01 [106]		0.51	0.30	0.22	0.95	3
III LSCF-oxide on Si-wafer02 [106]		0.51	0.33	0.22	0.92	3
IV LSCF-oxide on 8YSZ		0.57	0.36	0.12	0.93	3

Gastightness evaluation

LSCF membrane deposited on 8YSZ substrate without interlayer was not evaluated by helium leak test because it was too porous leading to as high permeability as substrate without any additional coating layer. In case of sputtered LSCF on various interlayers, relatively dense LSCF membrane was formed and thus the gastightness was evaluated by helium leak test, as shown in **Figure 97**. On the NDCGO layer supported by 8YSZ substrate, the pre-sintering temperature of interlayer (1000 or 1100°C) and solid concentration of nano-dispersion (1.0NDCGO or 1.5NDCGO) rarely influenced the gastightness of deposited LSCF. He leak rates showed the range of $1\sim5 \times 10^{-3}$ mbar.l/sec.cm². On CSCGO layer supported by NDCGO/8YSZ substrates, approx. 10 times higher He leak rate were detected. On NDCGO layer supported by $\alpha\text{Al}_2\text{O}_3$ substrate, the He leak rate of deposited membrane was the highest among the LSCF membranes deposited on various interlayers. It seems that the delamination of LSCF membrane could not be completely avoided, although it was improved with higher presintering temperature of interlayer.

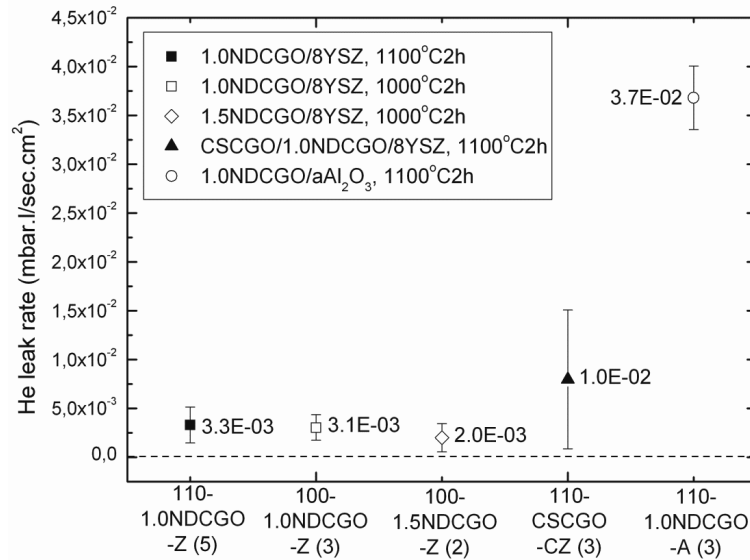


Figure 97 Gas-tightness estimation by He-leak test for MS-LSCF membranes on various substrates (diameter of measuring area $\phi_{\text{Measured}} = 20\text{mm}$, (number) is the number of sample tested)

5 Summary and outlook

In the present work, thin film membrane with approx. 1 μm thickness was developed with fluorite and perovskite materials, which are intended as O_2/N_2 gas separating membrane in fossil power plant. The investigated materials are $\text{Ce}_{0.8}\text{Gd}_{0.2}\text{O}_{2-\delta}$ (CGO) with fluorite crystal structure and $\text{La}_{0.58}\text{Sr}_{0.4}\text{Co}_{0.2}\text{Fe}_{0.8}\text{O}_{3-\delta}$ (LSCF) with perovskite crystal structure. CGO is expected to be more stable than other perovskite membranes in reducing atmospheres and to achieve sufficient oxygen permeation when produced as a film with $<100\mu\text{m}$ thickness. LSCF is expected to be highly permeable with an acceptable chemical stability. In order to increase the oxygen flux at a given temperature, the reduction of the membrane thickness is required. In this work, thin film membranes were developed on various substrate types by wet-chemical deposition (WCD) and physical vapor deposition (PVD).

Preparation and characterization of substrates

8YSZ (8 mol% Y_2O_3 stabilized ZrO_2) and $\alpha\text{Al}_2\text{O}_3$ substrates were prepared by vacuum-slip-casting, and WP/VSC (NiO/8YSZ) substrate, by using Coat-mix ® method. The total porosity of 8YSZ and $\alpha\text{Al}_2\text{O}_3$ substrates, pre-sintered at 1100°C for 2h in air, was 55.6% and 30.1%, respectively. With increasing pre-sintering temperature up to 1220°C , the total porosity of 8YSZ substrate was gradually reduced down to 39.7%. The porosity 44 ± 1 vol.% of reduced WP/VSC substrate was already studied in Ettler's work [81]. When the substrates were pre-sintered at 1100°C the gas permeability of 8YSZ exhibited 2.2 ~ 2.7-fold higher than that of $\alpha\text{Al}_2\text{O}_3$. With increasing pre-sintering temperature up to 1180°C , there was no big difference in gas permeability of 8YSZ substrates, while at 1220°C the sudden decrease in gas permeability was detected. When the thickness of 8YSZ substrate was reduced, their gas permeability was increased inversely proportional to the thickness reduction. The sintered WP/VSC substrate shows very low gas permeability. However, after reducing the substrate (NiO to Ni) the gas permeability was considerably increased, exhibiting approx. 6-fold higher than that of 110-8YSZ substrate. In addition, the surface roughness was measured to examine coating ability. The mean R_a of WP/VSC substrate was in the range of $0.5 \sim 1.1 \mu\text{m}$, being much higher than the mean R_a $0.2\sim 0.27 \mu\text{m}$ of 8YSZ substrates and the mean R_a $0.3\mu\text{m}$ of $\alpha\text{Al}_2\text{O}_3$ substrates.

Preparation and characterization of sols

NDCGO (CGO nano-dispersion), CSCGO (CGO colloidal sol), and CSAIOOH (AlOOH colloidal sol) were prepared for toplayer and/or interlayer. For NDCGO commercially available nano powder was dispersed in various molarity of nitric acid. CSCGO and CSAIOOH were derived via co-precipitation method using nitrate precursors and via sol-gel route using alkoxide precursors, respectively.

The stability of NDCGO was investigated, e.g. by means of zeta-potential, centrifuge behaviour and particle size evolution with time. When CGO nano-powder was dispersed in 0.05M HNO_3 , it showed the best stability among the NDCGOs using various molarity of nitric acid. For CSCGO, the pH 7.5 was adopted to obtain the effective particle size $d_{50} \sim 20$

5. Summary and outlook

nm which is smaller than that of *NDCGO* ($d_{50} \sim 90$ nm). The prepared *NDCGO* and *CSCGO* were identified by XRD and ICP-OES, exhibiting single CGO phase with desired fluorite structure and stoichiometry of $\text{Ce}_{0.76}\text{Gd}_{0.24}\text{O}_2$ for *NDCGO* and $\text{Ce}_{0.79}\text{Gd}_{0.21}\text{O}_2$ for *CSCGO*. Thermal analysis for *NDCGO*/PVA-Xerogel was carried out for the residue-free combustion. The burn-out of organic components was completed at approx. 400°C and thus the temperature of 500°C was adopted as a calcination temperature.

The colloidal sol of AlOOH exhibited the effective particle size $d_{50} \sim 30$ nm. The obtained alumina powder after heat-treatment was identified by XRD. The amorphous phase $\gamma\text{Al}_2\text{O}_3$ at 500°C underwent phase transition with elevating temperature, and finally polycrystalline $\alpha\text{Al}_2\text{O}_3$ was obtained at 1100°C.

Manufacture of CGO membrane by wet-chemical deposition

Spin-coating was used as coating method. With decrease in spinning time, the gastightness of sintered CGO membrane was improved. Reduction in rotation speed produced negative effect on gastightness of CGO membranes. Triple coatings, instead of double coatings, created severe cracks. However, it could be avoided with a decrease of the cooling rate during sintering. The effect of molecular weight (MW) of binder was additionally investigated. Increasing concentration of *NDCGOs* led to the increase in thickness of coating layer. With higher MW of binder the critical layer thickness was increased, thus crack-free layer was achieved by using higher concentration of *NDCGOs*. When the concentration of *NDCGO* (1.0 → 1.5 → 2.5 wt.%) or the number of coatings (double → triple coatings) was increased, the gas-tightness of sintered CGO membranes was improved, i.e. He leak rate was decreased from 7.4×10^{-3} mbar.l/sec.cm² to 1.1×10^{-4} mbar.l/sec.cm². In addition, reducing the sample with sintered membrane under Ar/4%H₂ led to 10 times higher He leak rate than before reducing.

Manufacture of CGO membrane by reactive magnetron sputtering

(A) 8YSZ substrates: A four-zone-model was proposed in this work. Without substrate bias CGO film was deposited with columnar structure, which is not gastight. With bias power (100W) the CGO membrane was deposited more compactly but severe delamination was observed on 110-8YSZ (presintered at 1100°C) due to compressive stresses induced. Obviously, mechanical strength of substrates was not sufficient. As elevating the pre-sintering temperature the mechanical strength of the substrate was improved and thus a delamination-free thin film was obtained. If the substrates were presintered at higher temperatures (1120, 1140 and 1180 °C), a higher bias power (> 100W) was required to achieve the compact membrane deposition because of coarsening of substrate particles. If pre-sintering temperature of substrate is too high (i.e. > 1180 °C), significant sintering occurs, leading to the decrease in gas permeability of substrate. In addition, with increasing the applied bias power, the thickness of membrane was reduced due to compaction of deposited thin film.

XRD pattern showed single CGO phase with desired fluorite crystal structure. The most preferred orientation was transferred from (111) at 0W to (220) at 400W bias power. The CGO peaks were slightly shifted toward lower angles, indicating that a compressive stress

was generated in the CGO membrane. The surface roughness of compactly deposited CGO membrane were much lower than that of substrates, i.e. mean $R_a < 0.14 \mu\text{m}$.

(B) NDCGO-Z: NDCGO was coated on 110-8YSZ substrates and pre-sintered at 500, 800 and 1000 °C for 2h in air. The substrates were called 50-NDCGO-Z, 80-NDCGO-Z and 100-NDCGO-Z according to the presintering temperature of NDCGO layer. When bias was applied to the substrates, the NDCGO layers were destroyed due to the insufficient mechanical strength, except for 80-1.0NDCGO-Z at 300W bias power. All interlayers may have the mechanical stability at the border of sufficient and insufficient states. At 0W bias power, the sputtered CGO could be deposited without destroying the NDCGO, but it was not gastight. In order to achieve the gastight membrane on this substrate, the strength of NDCGO layers should be enhanced, for instance, with increasing pre-sintering temperature of NDCGO layer.

(C) $\alpha\text{Al}_2\text{O}_3$: At 0W bias power, a porous CGO film was deposited. Applying bias produced the inhomogeneous microstructures which became more intensely noticeable with increasing bias power. A hypothesis was derived that the bias effect was concentrated near metallic substrate holder due to the poor electrical conductivity of the $\alpha\text{Al}_2\text{O}_3$ substrate. Consequently, ion bombardment was enhanced only near the holder and produced dense film only in this area (unbalanced bias effect).

XRD pattern showed single CGO membrane with desired fluorite crystal structure. The (200) orientation was most preferred at 0 and 100W bias power.

CGO membrane deposited with 300W bias was further heat-treated. At 1000°C the CGO columns started sintering, however, opening spaces between columns. At 1200°C the CGO membrane could be fully sintered but severe cracks were detected which might be generated e.g. due to the shrinkage mismatch during sintering or thermal mismatch during cooling.

(D) A30A: An alumina interlayer was prepared via sol-gel dip-coating to investigate the influence of substrate pore size on the sputtered film formation. The CGO film was deposited compactly, but severe microcracks were caused in all samples by thermal stress. When bias power was increased, the density cracks became lower but width of cracks became larger. The cracks have faded down at lower substrate temperature (set temperature: RT, actual temperature: approx. 150 °C) but they were still observable with SEM investigation.

(E) WP/VSC: At 0W bias power, although the dense substrate was used, porous film was deposited due to the high surface roughness of the substrate. Applying 400W bias enabled compact thin film deposition of CGO membrane. However, the failures, e.g. delamination or crack, of the deposited CGO membrane were observed after reducing the substrate because of the compressive stress generated.

Manufacture of LSCF membrane by magnetron sputtering (without substrate bias)

(A) 8YSZ: The desired single LSCF phase with cubic perovskite crystal structure was investigated by XRD. The film stoichiometry of $\text{La}_{0.57}\text{Sr}_{0.36}\text{Co}_{0.12}\text{Fe}_{0.93}\text{O}_3$ was analysed by ICP-OES, which can be slightly varied depending on substrate position during sputtering. The deposited thin film showed large pores due to the primary pore size of substrate surface.

5. Summary and outlook

(B)NDCGO-Z: Compact dense membrane with thickness of approx. 700 nm could be deposited. Pre-sintering temperature of NDCGO layer and concentration of NDCGOs rarely influenced the gastightness of deposited LSCF on them.

(C)CSCGO-CZ: CSCGO was additionally coated on NDCGO-Z. This substrate led to higher He leak rate, which are approx. 10 times higher than that of deposited membrane on NDCGO-Z. CSCGO layer might be mechanically weaker and damaged by atom bombardment.

(D)NDCGO-A: NDCGO was coated on 110- $\alpha\text{Al}_2\text{O}_3$ substrates and pre-sintered at 1000 and 1100 °C. The substrates were called 100-NDCGO-A and 110-NDCGO-A according to the presintering temperature of NDCGO layer. The NDCGO layer was not sufficiently adhesive to $\alpha\text{Al}_2\text{O}_3$ substrate, thus the delamination and peel-off of layer occurred when LSCF was deposited on the 100-NDCGO-A. With increasing pre-sintering temperature to 1100°C, failure-free LSCF membrane could be obtained. However, the membrane deposited on 110-NDCGO-A exhibited the highest He leak rate among the membranes deposited on various interlayers.

The gastightness of all prepared membrane in this work was summarized in **Table 19** with noticeable remarks.

As investigated in this work, depending on the coating method and the type of substrate material, the deposited thin films shows diverse coating behaviours. The most promising gastight CGO and LSCF membranes are the biased RMS-thin film supported by 8YSZ and the unbiased MS-thin film supported by NDCGO/8YSZ, respectively. The performance of these membranes has to be investigated comprehensively with respect to different transport limitations possible, i.e. surface exchange kinetics or concentration polarization in the substrate. This was not possible in this work due to time constraints. A few specific aspects have to be considered, which are mainly related to the sealing procedure. Commonly, gold (ring or paste) is used for sealing in the permeation test set-up. This requires temperature around 1000 °C close to the melting point of gold, i.e. 1064 °C. However, during sputtering the layers were exposed to 800 °C only. Therefore, sintering occurs at higher temperatures leading e.g. to warped samples after heat treatment to 1000 °C for 5 hours. In case of mechanical constraints in the permeation test set-up the additional stress become too high resulting in severe chipping off. Therefore, either sealing procedure has to be adapted to these specific membranes or appropriate pre-treatment of the membrane has to be found in order to use gold seals.

Further membrane development should focus on the following aspects. *For CGO coatings by RMS*, interlayers have to be developed which are mechanically stable enough to withstand the compressive stresses induced during biased-sputtering. Furthermore, increasing the substrate temperature for RMS should improve compactness of coatings. *In case of LSCF*, sputtering is not yet fully developed. Applying bias as well as the development of reactive magnetron sputtering are promising research directions. *For CGO coatings by WCD*, the stability of CGO nano-dispersions should be optimized e.g. by using dispersants in order to increase the zeta potential. Furthermore, proper colloidal or polymeric sols could be applied in order to increase sintering activity.

Table 19 Summary of all prepared membranes with gastightness and noticeable remarks.

Membrane	Substrate	Method	Gastightness (He leak rate, mbar.l/sec.cm ²)	Remarks
CGO	WP/VSC	Spin-coating	$1.1 \times 10^{-4} \sim 7.5 \times 10^{-4}$ (triple coating as sintered)	Dense membrane formation Pinholes when stability of NDCGO ↓
			1.1×10^{-3} (triple coating as reduced)	No failure when reducing substrate.
	WP/VSC	RMS	$5.8 \times 10^{-4} \sim 1.4 \times 10^{-3}$ (as deposited on final-sintered substrate)	Compact membrane formation with bias Cracks under reducing substrate.
			1.4×10^{-2} (as deposited on pre-sintered substrate)	Compact membrane formation with bias Delamination under red. substrate.
	8YSZ	RMS	$6.9 \times 10^{-4} \sim 2.8 \times 10^{-3}$ (as deposited on pre-sintered substrate)	Compact membrane formation with bias and higher T _{pre-sintering} of substrate. (Four-Zone-Model)
	NDCGO-Z	RMS	Peeling-off (as deposited on pre-sintered substrate)	Higher mechanical strength of NDCGO is required, i.e. T _{presintering} at > 1000 °C.
	αAl ₂ O ₃	RMS	Inhomogeneous film (as deposited on pre-sintered substrate)	Unbalanced bias effect due to low el. conductivity of substrate.
LSCF	A30A	RMS	Microcracks (as deposited on pre-sintered substrate)	Cracks due to thermal mismatch.
	8YSZ	MS	Pores (as deposited on pre-sintered substrate)	Porous film deposition due to primary pores of substrate
	NDCGO-Z	MS	$2.0 \times 10^{-3} \sim 2.5 \times 10^{-3}$ (as deposited on pre-sintered substrate)	Compact membrane formation on fine pores of interlayer
	CSCGO-CZ	MS	$2.7 \times 10^{-3} \sim 1.7 \times 10^{-2}$ (as deposited on pre-sintered substrate)	Negative effect of additional CSCGO layer due to lower mechanical strength.
	NDCGO-A	MS	$3.4 \times 10^{-2} \sim 4.1 \times 10^{-2}$ (as deposited on pre-sintered substrate)	higher He leak rate due to lower adhesion of NDCGO to αAl ₂ O ₃

References

- [1] "World Energy Outlook 2010: <http://www.worldenergyoutlook.org/2010.asp>," ed: International Energy Agency.
- [2] R. Carapellucci and A. Milazzo, "Membrane systems for CO₂ capture and their integration with gas turbine plants," *Proceedings of the Institution of Mechanical Engineer, Part A: Journal of Power and Energy*, vol. 217, p. 505, 2003.
- [3] IPCC, "Special report on carbon dioxide capture and storage," Cambridge University Press 2005.
- [4] R. Pruschek, G. Oeljeklaus, V. Brand, G. Haupt, G. Zimmermann, and J. S. Ribberink, "Combined cycle power plant with integrated coal gasification, CO shift and CO₂ washing," *Energy Conversion and Management*, vol. 36, pp. 797-800, 1995.
- [5] P. H. M. Feron and C. A. Hendriks, "CO₂ Capture Process Principles and Costs," *Oil & Gas Science and Technology*, vol. 60, pp. 451-459, 2005.
- [6] J. D. Figueroa, T. Fout, S. Plasynski, H. McIlvried, and R. D. Srivastava, "Advances in CO₂ capture technology-The U.S. Department of Energy's Carbon Sequestration Program," *International journal of greenhouse gas control*, vol. 2, pp. 9-20, 2008.
- [7] S. I. Plasynski, J. T. Litynski, H. G. McIlvried, and R. D. Srivastava, "Progress and New Developments in Carbon Capture and storage," *Critical Reviews in Plant Science*, vol. 28, pp. 123-138, 2009.
- [8] S. Donner and D. Lübbert, "Kohlendioxid-arme kraftwerke," Deutscher Bundestag-Wissenschaftliche Dienste 2006.
- [9] M. Czaperek, P. Zapp, H. J. M. Bouwmeester, M. Modigell, K.-V. Peinemann, I. Voigt, W. A. Meulenber, L. Singheiser, and D. Stöver, "MEM-BRAIN gas separation membranes for zero-emission fossil power plants," *Energy Procedia*, vol. 1, 2009.
- [10] J. Sunarso, S. Baumann, J. M. Serra, W. A. Meulenber, S. Liu, Y. S. Lin, and J. C. D. Costa, "Mixed ionic-electronic conducting (MIEC) ceramic-based membranes for oxygen separation," *Journal of Membrane Science*, vol. 320, pp. 13-41, 2008.
- [11] C. Wagner, "Equation for transport in solid oxide and sulfides of transition metals," *Solid State Chemistry*, vol. 10, pp. 3-16, 1975.
- [12] H. J. M. Bouwmeester and A. J. Burggraaf, "Dense ceramic membranes for oxygen separation," in *Fundamentals of Inorganic Membrane Science and Technology*, A. J. Burggraaf and L. Cot, Eds., ed Amsterdam: Elsevier Science B. V., 1996.
- [13] K. Wiik, A. Aasland, H. L. Hansen, I. L. Tangen, and R. Ødegård, "Oxygen permeation in the system SrFeO_{3-x} - SrCoO_{3-y}," *Solid State Ionics*, vol. 152-153, pp. 165-680, 2002.

References

- [14] V. V. Kharton, F. M. B. Marques, and A. Atkinson, "Transport properties of solid oxide electrolyte ceramics: a brief review," *Solid State Ionics*, vol. 174, pp. 135-149, 2004.
- [15] L. Malavasi, C. A. J. Fischer, and M. S. Islam, "Oxide-ion and proton conducting electrolyte materials for clean energy applications: structural and mechanistic features," *Chemical Society Reviews*, vol. 39, pp. 4370-4387, 2010.
- [16] R. Gerhardt-Anderson and A. S. Nowick, "Ionic conductivity of CeO_2 with trivalent dopants of different ionic radii," *Solid State Ionics*, vol. 5, pp. 547-550, 1981.
- [17] J. A. Kilner, "Fast anion transport in solids," *Solid State Ionics*, vol. 8, pp. 201-207, 1983.
- [18] K. Eguchi, T. Setoguchi, T. Inoue, and H. Arai, "Electrical properties of ceria-based oxides and their application to solid oxide fuel cells," *Solid State Ionics*, vol. 52, pp. 165-172, 1992.
- [19] S. Zha, C. Xia, and G. Meng, "Effect of Gd (Sm) doping on properties of ceria electrolyte for solid oxide fuel cells," *Journal of Power Sources*, vol. 115, pp. 44-48, 2003.
- [20] M. Mogensen, T. Lindegaard, and U. R. Hansen, "Physical Properties of Mixed Conductor Solid Oxide Fuel Cell Anodes of Doped CeO_2 ," *Journal of the Electrochemical Society*, vol. 141, pp. 2122-2128, 1994.
- [21] F. A. Kröger and H. J. Vink, "Relations between the Concentrations of Imperfections in Crystalline Solids," *Solid State Physics*, vol. 3, pp. 307-435, 1956.
- [22] R. Karoum, V. Roche, C. Pirovano, R.-N. Vannier, A. Billard, and P. Vernoux, "CGO-based electrochemical catalysts for low temperature combustion of propene," *Journal of Applied Electrochemistry*, vol. 40, pp. 1867-1873, 2010.
- [23] S. Wang, H. Inaba, H. Tagawa, M. Dokiya, and T. Hashimoto, "Nonstoichiometry of $\text{Ce}_{0.9}\text{Gd}_{0.1}\text{O}_{1.95-x}$," *Solid State Ionics*, vol. 107, pp. 73-79, 1998.
- [24] B. C. H. Steele, "Appraisal of $\text{Ce}_{1-y}\text{Gd}_y\text{O}_{2-y/2}$ electrolytes for IT-SOFC operation at 500°C ," *Solid State Ionics*, vol. 129, pp. 95-110, 2000.
- [25] O. Muller and R. Roy, *The Major Ternary Structural Families*. Berlin: Springer-Verlag, 1974.
- [26] V. M. Goldschmidt, *Geochemische Verteilungsgesetze der Elemente - Die Gesetze der Krystallochemie Bd. 7*. Oslo: Norske Videnskaps-Akademi, 1926.
- [27] M. A. Pena and J. L. G. Fierro, "Chemical structures and performance of perovskite oxides," *Chemical Reviews*, vol. 101, pp. 1981-2017, Jul 2001.

-
- [28] A. S. Bhalla, R. Gua, and R. Roy, "The perovskite structure - a review of its role in ceramic science and technology," *Mat Res Innovat*, vol. 4, pp. 3-26, 2000.
- [29] H. U. Anderson, "Review of p-type doped perovskite materials for SOFC and other applications," *Solid State Ionics*, vol. 52, pp. 33-41, 1992.
- [30] C. Zener, "Interaction between the d-Shells in the Transition Metals. II. Ferromagnetic Compounds of Manganese with Perovskite Strcuture," *Physical Review*, vol. 82, pp. 403-405, 1951.
- [31] Z. Shao, W. Yang, Y. Cong, H. Dong, J. Tong, and G. Xiong, "Investigation of the permeation behavior and stability of a $\text{Ba}_{0.5}\text{Sr}_{0.5}\text{Co}_{0.8}\text{Fe}_{0.2}\text{O}_{3-\delta}$ oxygen membrane," *Journal of Membrane Science*, vol. 172, pp. 177-188, 2000.
- [32] Y. Teraoka, H. M. Zhang, S. Furukawa, and N. Yamazoe, "Oxygen Permeation through Perovskite-Type Oxides," *Chemistry Letters*, pp. 1743-1746, 1985.
- [33] Y. Teraoka, T. Nobunaga, and N. Yamazoe, "Effect of Cation Substitution on the Oxygen Semipermeability of Perovskite-Type Oxides," *Chemistry Letters*, pp. 503-506, Mar 1988.
- [34] Y. Teraoka, H. M. Zhang, K. Okamoto, and N. Yamazoe, "Mixed ionic-electronic conductivity of $\text{La}_{1-x}\text{Sr}_x\text{Co}_{1-y}\text{Fe}_y\text{O}_{3-\delta}$ perovskite-type oxides," *Materials Research Bulletin*, vol. 23, pp. 51-58, 1988.
- [35] Y. Teraoka, T. Nobunaga, K. Okamoto, N. Miura, and N. Yamazoe, "Influence of Constituent Metal-Cations in Substituted LaCoO_3 on Mixed Conductivity and Oxygen Permeability," *Solid State Ionics*, vol. 48, pp. 207-212, Nov 1991.
- [36] J. W. Stevenson, T. R. Armstrong, R. D. Carneim, L. R. Pederson, and W. J. Weber, "Electrochemical properties of mixed conducting perovskites $\text{La}_{1-x}\text{M}_x\text{Co}_{1-y}\text{Fe}_y\text{O}_{3-\delta}$ (M=Sr,Ba,Ca)," *Journal of the Electrochemical Society*, vol. 143, pp. 2722-2729, Sep 1996.
- [37] Y. S. Chou, J. W. Stevenson, T. R. Armstrong, and L. R. Pederson, "Mechanical properties of $\text{La}_{1-x}\text{Sr}_x\text{Co}_{0.2}\text{Fe}_{0.8}\text{O}_3$ mixed-conducting perovskites made by the combustion synthesis technique," *Journal of the American Ceramic Society*, vol. 83, pp. 1457-1464, Jun 2000.
- [38] C. Y. Tsai, A. G. Dixon, Y. H. Ma, W. R. Moser, and M. R. Pascucci, "Dense perovskite, $\text{La}_{1-x}\text{A}'_x\text{Fe}_{1-y}\text{Co}_y\text{O}_{3-\delta}$ ($\text{A}'=\text{Ba, Sr, Ca}$), membrane synthesis, applications, and characterization," *Journal of the American Ceramic Society*, vol. 81, pp. 1437-1444, Jun 1998.
- [39] J. A. Lane, S. J. Benson, D. Waller, and J. A. Kilner, "Oxygen transport in $\text{La}_{0.6}\text{Sr}_{0.4}\text{Co}_{0.2}\text{Fe}_{0.8}\text{O}_{3-\delta}$," *Solid State Ionics*, vol. 121, pp. 201-208, Jun 1999.
- [40] S. J. Benson, D. Waller, and J. A. Kilner, "Degradation of $\text{La}_{0.6}\text{Sr}_{0.4}\text{Fe}_{0.8}\text{Co}_{0.2}\text{O}_{3-\delta}$ in Carbon Dioxide and Water Atmospheres," *Journal of The Electrochemical Society*, vol. 146, pp. 1305-1309, 1999.
-

References

- [41] D. Schlehuber, E. Wessel, L. Singheiser, and T. Markus, "Long-term operation of a $\text{La}_{0.58}\text{Sr}_{0.4}\text{Co}_{0.2}\text{Fe}_{0.8}\text{O}_{3-\delta}$ -membrane for oxygen separation," *Journal of Membrane Science*, vol. 351, pp. 16-20, 2010.
- [42] K. S. W. Sing, D. H. Everett, R. A. W. Haul, L. Moscou, R. A. Pierotti, J. Rouquérol, and T. Siemieniowska, "Reporting physisorption data for gas/solid systems with Special Reference to the Determination of Surface Area and Porosity," *Pure and Applied Chemistry*, vol. 57, pp. 603-619, 1985.
- [43] A. Larbot, "Ceramic processing techniques of support systems for membrane synthesis," in *Fundamentals of inorganic membrane science and technology*, A. J. Burggraaf and L. Cot, Eds., ed Amsterdam: Elsevier Science B. V., 1996.
- [44] B. C. Bonekamp, "Preparation of asymmetric ceramic membrane supports by dip-coating," in *Fundamentals of Inorganic Membrane Science and Technology*, A. J. Burggraaf and L. Cot, Eds., ed: Elsevier Science B. V., 1996.
- [45] Forschungszentrum Jülich GmbH, IEK-1: Materials Synthesis and Processing http://www.fz-juelich.de/iek/iek-1/DE/Home/home_node.html [Online].
- [46] K. S. Brinkman, H. Takamura, H. L. Tuller, and T. Iijima, "The Oxygen Permeation Properties of Nanocrystalline CeO_2 Thin Films," *Journal of the Electrochemical Society*, vol. 157, pp. B1852-B1857, 2010.
- [47] N. Rane, H. Zou, G. Buelna, and J. Y. S. Lin, "Sol-gel synthesis and properties of unsupported and supported mesoporous ceria membranes," *Journal of Membrane Science*, vol. 256, pp. 89-97, Jul 1 2005.
- [48] Q. Fang and J. Y. Zhang, "Preparation of $\text{Ce}_{1-x}\text{Gd}_x\text{O}_{2-0.5x}$ thin films by UV assisted sol-gel method," *Surface & Coatings Technology*, vol. 151, pp. 100-104, Mar 1 2002.
- [49] J. B. Huang, C. L. Chang, C. S. Hsu, and B. H. Hwang, "Electrostatic Spray Deposition of Doped Ceria Films," *Fuel Cells*, vol. 10, pp. 1095-1099, Dec 2010.
- [50] M. P. Lobera, J. M. Serra, S. P. Foghmoes, M. SØgaard, and A. Kaiser, "On the use of supported ceria membranes for oxyfuel process/syngas production," *Journal of Membrane Science*, 2011.
- [51] A. Abrutis, A. Teiserskis, G. Garcia, K. V. Z. Saltyte, Z. Salciunas, F. V. A. Figueras, and S. Rushworth, "Preparation of dense, ultra-thin MIEC ceramic membranes by atmospheric spray-pyrolysis technique," *Journal of Membrane Science*, vol. 240, pp. 113-122, Sep 1 2004.
- [52] O. Buchler, J. M. Serra, W. A. Meulenber, D. Sebold, and H. P. Buchkremer, "Preparation and properties of thin $\text{La}_{1-x}\text{Sr}_x\text{Co}_{1-y}\text{Fe}_y\text{O}_{3-\delta}$ perovskitic membranes supported on tailored ceramic substrates," *Solid State Ionics*, vol. 178, pp. 91-99, Jan 31 2007.

-
- [53] J. Gurauskis, Ø. F. Lohne, H. L. Lein, and K. Wiik, "Processing of thin film ceramic membranes for oxygen separation," *Journal of the European Ceramic Society*, vol. 32, pp. 649-655, 2012.
- [54] A. Julian, E. Juste, P. M. Geffroy, V. Coudert, S. Degot, P. Del Gallo, N. Richet, and T. Chartier, "Elaboration of $\text{La}_{0.8}\text{Sr}_{0.2}\text{Fe}_{0.7}\text{Ga}_{0.3}\text{O}_{3-\delta}$ / $\text{La}_{0.8}\text{M}_{0.2}\text{FeO}_{3-\delta}$ (M = Ca, Sr and Ba) asymmetric membranes by tape-casting and co-firing," *Journal of Membrane Science*, vol. 333, pp. 132-140, May 1 2009.
- [55] S. Baumann, J. M. Serra, M. P. Lobera, S. Escolastico, F. Schulze-Kuppers, and W. A. Meulenbergh, "Ultrahigh oxygen permeation flux through supported $\text{Ba}_{0.5}\text{Sr}_{0.5}\text{Co}_{0.8}\text{Fe}_{0.2}\text{O}_{3-\delta}$ membranes," *Journal of Membrane Science*, vol. 377, pp. 198-205, Jul 15 2011.
- [56] B. V. Derjaguin and L. D. Landau, "Theory of stability of highly charged lyophobic sols and adhesion of highly charged particles in solutions of electrolytes," *Acta Physicochimica URSS*, vol. 14, p. 633, 1941.
- [57] E. J. W. Verwey and J. T. G. Overbeek, "Theory of stability of Lyophobic Colloids," ed. Amsterdam: Elsevier, 1948.
- [58] O. Stern, "The theory of the electrolytic double layer," *Zeitschrift für Elektrochemie und angewandte physikalische Chemie*, vol. 30, p. 508, 1924.
- [59] W. Sigmund, G. Pyrgiotakis, and A. Daga, "II Powder Processing at the Nanoscale "Theory and Application of Colloidal processing"," in *Chemical Processing of Ceramics*, B. I. Lee and S. Komarneni, Eds., ed: CRC Press, 2005.
- [60] T. Sato and R. Ruch, *Stabilization of Colloidal Dispersions by Polymer Adsorption*. New York: Marcel Dekker, Inc., 1980.
- [61] J. Böhnlein-Mauß, W. Sigmund, G. Wegner, W. H. Meyer, F. Heßel, K. Seitz, and A. Roosen, "The Function of Polymers in the Tape Casting of Alumina," *Advanced Materials*, vol. 4, pp. 73-81, 2004.
- [62] A. G. Emslie, F. T. Bonner, and C. G. Peck, "Flow of a viscous liquid on a rotating disk," *Journal of Applied Physics*, vol. 29, p. 858, 1958.
- [63] D. Meyerhofer, "Characteristics of resist films produced by spinning," *Journal of Applied Physics*, vol. 49, p. 3993, 1978.
- [64] L. Landau and B. Levich, "Dragging of a liquid by a moving plate," *Acta Physicochimica URSS*, vol. 17, p. 42, 1942.
- [65] A. F. M. Leenaars and A. J. Burggraaf, "The preparation and Characterization of Alumina Membranes with Ultrafine Pores 2. The Formation of Supported Membranes," *Journal of Colloid and Interface Science*, vol. 105, pp. 27-40, 1985.
-

References

- [66] R. J. R. Uhlhorn, M. H. B. J. H. I. t. Veld, K. Keizer, and A. J. Burggraaf, "Synthesis of ceramic membranes Part I Synthesis of non-supported and supported γ -alumina membranes without defects," *Journal of Materials science*, vol. 27, pp. 527-537, 1992.
- [67] G. W. Scherer, "Recent progress in drying of gels," *Journal of Non-Crystalline Solids*, vol. 147-148, pp. 363-374, 1992.
- [68] S. G. Croll, "The Origin of Residual Internal Stress in Solvent-Cast Thermoplastic Coatings," *Journal of Applied Polymer Science*, vol. 23, 1979.
- [69] A. J. Evans, M. D. Dory, and M. S. Hu, "The Cracking and Decohesion of Thin Films," *Journal of materials research*, vol. 3, pp. 1043-1054, 1988.
- [70] D. L. Johnson and I. B. Cutler, "Diffusion sintering, I: initial stage models and their applications to shrinkage of powder compacts, II: initial sintering kinetics of alumina.," *Journal of the American Ceramic Society*, vol. 46, p. 541, 1963.
- [71] A. L. Stuijts, "Synthesis of Materials from Powders by Sintering," *Annual Review of Materials Science*, vol. 3, pp. 363-395, 1973.
- [72] S.-J. L. Kang, *Sintering: Densification, Grain Growth and Microstructure*: Butterworth-Heinemann, 2005.
- [73] R. W. Balluffi, S. M. Allen, W. C. Carter, and R. A. Kemper, *Kinetics of Materials*: Wiley-Interscience, 2005.
- [74] J. E. Mahan, *Physical vapor deposition of thin films*: John Wiley & Sons, Inc., 2000.
- [75] D. M. Mattox, *Handbook of physical vapor deposition (PVD) processing*. USA: Noyes Publications, 1998.
- [76] S. Schiller, U. Heisig, C. Korndörfer, G. Beister, J. Reschke, K. Steinfeld, and J. Strümpfel, "Reactive D.C. High-rate sputtering as production technology," *Surface and Coating Technology*, vol. 33, pp. 405-423, 1987.
- [77] J. A. Thornton, "Influence of apparatus geometry and deposition conditions on the structure and topography of thick sputtered coatings," *Journal of Vacuum Science and Technology*, vol. 11, p. 666, 1973.
- [78] B. A. Movchan and A. V. Demchishin, "Study of the structure and properties of thick vacuum condensates of nickel, titanium, tungsten, aluminium oxide and zirconium dioxide.," *The physics of metals and metallography*, vol. 28, pp. 83-90, 1969.
- [79] D. Simwonis, A. Naoumidis, F. J. Dias, J. Linke, and A. Moropoulou, "Material characterization in support of the development of an anode substrate for solid oxide fuel cells," *Journal of materials research*, vol. 12, pp. 1508-1518, 1997.
- [80] F. Tietz, H.-P. Buchkremer, and D. Stöver, "Components manufacturing for solid oxide fuel cells," *Solid State Ionics*, vol. 152-153, pp. 373-381, 2002.

-
- [81] M. Ettler, "Einfluss von Reoxidationszyklen auf die Betriebsfestigkeit von anodengestützten Festoxid-Brennstoffzellen, p. 63," *Dissertation*, Forschungszentrum Jülich GmbH, Institute of Energy and Climate Research (IEK-1), Ruhr Universität Bochum, 2008.
- [82] A. F. M. Leenaars, K. Keizer, and A. J. Burggraaf, "The Preparation and Characterization of Alumina Membranes with Ultra-Fine Pores," *Journal of Materials science*, vol. 19, pp. 1077-1088, 1984.
- [83] N. Benes, A. Nijmeijer, and H. Verweij, Eds., *Microporous Silica Membranes (p. 335-372)* (Recent Advances in Gas Separation by Microporous Ceramic Membranes. ELSEVIER, 2000
- [84] A. J. Burggraaf, "Fundamentals of membrane top-layer synthesis and processing," in *Fundamental of Inorganic Membrane Science and Technology*, A. J. Burggraaf and L. Cot, Eds., ed: Elsevier Science B.V., 1996.
- [85] N. J. Escalona, "Herstellung von Hochtemperatur-Brennstoffzellen über physikalische Gasphasenabscheidung," *Dissertation*, Forschungszentrum Jülich GmbH, Ruhr-Universität Bochum, 2008.
- [86] E. W. Washburn, "The dynamics of capillary flow.," *Physical Review*, vol. 17, pp. 273-283, Mar 1921.
- [87] H. G. Merkus, "Chapter 12 Dynamic Light Scattering," in *Particle Size Measurements: Fundamentals, Practice, Quality*, ed: Springer, 2009.
- [88] "Color 3D Laser Microscope VK-9700K User's Manual," ed: KEYENCE Corporation.
- [89] L. Reimer, *Scanning Electron Microscopy- Physics of Image Formation and Microanalysis*. Berlin: Springer, 1998.
- [90] S. J. B. Reed, *Electron Microprobe Analysis and Scanning Electron Microscopy in Geology*. New York: Cambridge University Press, 2005.
- [91] M. J. Godinho, R. F. Goncalves, L. P. S. Santos, J. A. Varela, E. Longo, and E. R. Leite, "Room temperature co-precipitation of nanocrystalline CeO_2 and $\text{Ce}_{0.8}\text{Gd}_{0.2}\text{O}_{1.9-\delta}$ powder," *Materials Letters*, vol. 61, pp. 1904-1907, Apr 2007.
- [92] M. M. Mandanas and G. L. Messing, "Thermogravimetric analysis of organic binder segregation during drying of particulate suspensions," *Thermochimica Acta*, vol. 363, pp. 37-45, Nov 27 2000.
- [93] D. S. Tucker, "Gamma-to-Alpha Transformation in Spherical Aluminum-Oxide Powders," *Journal of the American Ceramic Society*, vol. 68, pp. C163-C164, 1985.
- [94] B. K. Gan, I. C. Madsen, and J. G. Hockridge, "In situ X-ray diffraction of the transformation of gibbsite to alpha-alumina through calcination: effect of particle size and heating rate," *Journal of Applied Crystallography*, vol. 42, pp. 697-705, Aug 2009.
-

References

- [95] S. J. Wilson and J. D. C. McConnell, "A Kinetic-Study of the System Alpha-Al₂O₃," *Journal of Solid State Chemistry*, vol. 34, pp. 315-322, 1980.
- [96] J. Janek and C. Korte, "Electrochemical blackening of yttria-stabilized zirconia - morphological instability of the moving reaction front," *Solid State Ionics*, vol. 116, pp. 181-195, Jan 1999.
- [97] "Electrical Properties of Materials," in *CRC Materials Science and Engineering Handbook (Third Edition)*, J. F. Shackelford and W. Alexander, Eds., ed: CRC Press, 2001.
- [98] F. T. Ciacchi, K. M. Crane, and S. P. S. Badwal, "Evaluation of Commercial Zirconia Powders for Solid Oxide Fuel-Cells," *Solid State Ionics*, vol. 73, pp. 49-61, Oct 1994.
- [99] V. V. Kharton, A. P. Viskup, F. M. Figueiredo, E. N. Naumovich, A. A. Yaremchenko, and F. M. B. Marques, "Electron-hole conduction in Pr-doped Ce(Gd)O_{2-δ} by faradaic efficiency and emf measurements," *Electrochimica Acta*, vol. 46, pp. 2879-2889, 2001.
- [100] J. M. Soro, L. Lelait, J. C. van Duysen, G. Zacharie, and J. von Stebut, "Influence of substrate roughness and lateral spacing on morphology and brittleness of different Cr-C PVD coatings," *Surface & Coatings Technology*, vol. 98, pp. 1490-1496, Jan 1998.
- [101] A. Faes, A. Nakajo, A. Hessler-Wyser, D. Dubois, A. Brisse, S. Modena, and J. Van Herle, "RedOx study of anode-supported solid oxide fuel cell," *Journal of Power Sources*, vol. 193, pp. 55-64, Aug 1 2009.
- [102] V. Perrichon, A. Laachir, G. Bergeret, R. Frety, L. Tournayan, and O. Touret, "Reduction of Cerias with Different Textures by Hydrogen and Their Reoxidation by Oxygen," *Journal of the Chemical Society-Faraday Transactions*, vol. 90, pp. 773-781, Mar 7 1994.
- [103] A. Trovarelli, "Catalytic properties of ceria and CeO₂-containing materials," *Catalysis Reviews-Science and Engineering*, vol. 38, pp. 439-520, 1996.
- [104] E. A. Kummerle and G. Heger, "The structures of C-Ce₂O_{3+δ}, Ce₇O₁₂, and Ce₁₁O₂₀," *Journal of Solid State Chemistry*, vol. 147, pp. 485-500, Nov 1 1999.
- [105] C. Weiler, "Herstellung von Elektrodenstrukturen für Hochtemperatur-Brennstoffzellen mittels physikalischer Gasphasenabscheidung," Diploma thesis, Institute for Energy und Climate Research, IEK-1: Materials Synthesis and Processing, RWTH Aachen, 2011.
- [106] F. Vondahlen and S. Uhlenbruck, "Internal report: chemical analysis of LSCF-oxide.," Forschungszentrum Jülich GmbH, IEK-1: Materials Synthesis and Processing 2010.

Acknowledgements

The present work was written during my activity as PhD student at the institute of energy and climate research (IEK-1) of research center Jülich (Forschungszentrum Jülich GmbH). I convey a hearty thanks to all my colleagues for the good time, the great cooperation and the pleasant working atmosphere at the institute.

I would like to express my sincere appreciation to Prof. Dr. Detlev Stöver for the challenging task and great support of my work as “Doktorvater”. I also want to thank Prof. Dr. Robert Vaßen for the kind attention to my work and for the takeover of co-referee, and Prof. Dr. Michael Abramovici for the gentle chairmanship of the examination committee.

I would like to convey a special thanks to Dr. Hans Peter Buchkremer for his kindness with “Papa-smile” and the diverse support during my time at the research center, and to Dr. Wilhelm Albert Meulenberg for taking care of me as a membrane family with the excellent supervisions and for giving me a fantastic nickname ‘Honey Moon!’. I am most grateful to Dr. Stefan Baumann for the best supervision with plentiful discussions and suggestions, and for endless encouragement with great sense of humor. To Dr. Sven Uhlenbruck I really thank for valuable supervision in sputtering and professional advises with ‘Baby-smile’, and to Dr. Tim van Gestel for guidance of wet-coating and for instructive correction of my thesis.

I thank sincerely Dr. Feng Han and Dr. Felix Hauler not only for their lots of helps and discussions in wet-coating but also for their warm friendship during my PhD time, and I would like to express my huge appreciation to Mr. Frank Vondahlen and Dr. Ronan Nédélec for their lots of help in sputtering and also important tips for the work. To Mr. Marian Kampel, Mr. Jörn Faul and Mr. Stefan Heinz I am very grateful for kind help with permeation measurement as well as all kinds of technical assistance. I am also grateful to Mr. Volker Bader for the kind assistance in heat-treatment orders and help with the questions related to the heat-treatment, to Mr. Werner Herzhof for supplying the warm-pressed substrates for wet-coating and help with the questions related to the chemical order, to Mr. Mark Kappertz for kind instruction and further skillful help with various lab-works in metallography laboratory, to Dr. Qianli Ma for instruction of Pechini-method and for lots of kind help with various areas at the institute, and to Ms. Hiltrud Moitru for professional photographs of samples and facility (especially, your photograph of permeation test equipment with me was really popular in FZJ 2011!). I want to particularly thank and give a big hug to Ms. Boouk Hur who was a great help to me during her internship time.

For material characterization, my many thanks go to Dr. Werner Fischer and Mr. Mirko Ziegner for XRD investigation and the detailed explanations of the results, to Dr. Doris Sebold for numerous SEM investigations with impressive imaging skill, to Ms. Sigrid Schwartz-Lückge for the help with mercury porosimetry investigations, to Dr. Robert Mücke for the help with characterization using He-leak test and confocal laser microscopy, to Ms. Marie-Theres Gerhards and Dr. Frank Tietz for implementing and evaluating the thermal analysis, and to Mr. Joon-Yong Choi for kind instruction of Hitachi-SEM and for warm support like real brother!

For the workshop team, I would like to thank very much to Mr. Gert Mattonette and Mr. Fried Oellers for reliable and fast processing of manufacturing orders and for your kindness. As Mr. Oellers said, “Es gab immer etwas zum Lachen!” with you. For all administrative assistance I thank Ms. Vicky Rostin, Ms. Hannelore Rüter, Mr. Stefan Weitz, Ms. Marlene Pionke and Ms. Marianne Meyer. Particular, I would like to convey my lots of thanks to Ms. Rüter for

Acknowledgements

her warm care of me sometimes like a friend and sometimes like a mother. Furthermore, I really thank Mr. Björn Lambertz and Mr. Rainer Kriescher for the help with computer related issues.

To Cosy-family Dr. Ye Xing, Dr. Mariya Ivanova, Dr. Falk Schulze-Küppers, Mr. Stephen Gibson, Ms. Vinti Agrawal, Ms. Yilin Zhao, Mr. Jan Philippen, Ms. Marissa Rosenbauer, Mr. Andreas Franke, Mr. Tobias Wegener and also who I maybe forget to write, I really want to say “huge thanks to you”. The beginning of my PhD time was really pleasant with you and I could be quick to adapt to the new surroundings.

A very big thank to my former office mates, Dr. Vadym Kochubey, Mr. Sascha Dobrowolny and Ms. Boouk Hur, and to my current office mates, Dr. Feng Han, Mr. Stefan Resanka and Dr. Janika Boltz, for the great time together and amusing and pleasant atmosphere during the time with you in the office (no. 113).

For the help with the preparation of doctoral examination, I thank Dr. Wilhelm Albert Meulenberg, Dr. Stefan Baumann, Dr. Falk Schulze-Küppers, Dr. Feng Han, Dr. Janika Boltz, Dr. Ophelia Jarligo, Mr. Sungjune Park, Mr. Chanwoo Park, and I thank Mr. Alexandre Guignard for the protocol writing during my examination.

For additional support in many other cases during my PhD time I also thank my former and current PhD colleagues, Dr. Manuel Köhl, Dr. Wolfgang Schafbauer, Dr. Oskar Hassan, Dr. Karim Kamran, Dr. Michael Betz, Dr. Li meng, Dr. Katharina, Dr. Felix Hauler, Dr. Feng Han, Dr. Raphael Berhane, Dr. Anita Neumann, Dr. Ye Xing, Dr. Ana Paula Cysne Barbosa, Mr. Alexandre Guignard, Mr. Andreas Hospach, Ms. Janka Seeger, Mr. Jan Hoffmann, Ms. Svenja Ebert, Ms. Linnan Du, Mr. Stefan Resanka, Jan Eiberger, Mr. Martin Bitzer, Mr. Sebastian Vieweger, Ms. Desiree van Holt...

I thank Korea society in research center Jülich during my PhD time, to Dr. Kyongok Kang, Dr. Shang Yik Reigh, Mr. Joon Yong Choi, Dr. Songhak Yoon, Dr. Seung Keun Kim, Dr. Jeong Hwan Kim, Dr. Han Min Woo, Mr. Chang Hoon Heo, Dr. Seong Dae Yun with Ms. Yunhee Jang, Mr. Chanwoo Park, Ms. Eunji Park, Mr. Young Ha Kim, Mr. Hyunjung Kim, Ms. Hyunji Kim, Ms. Jiyeon Kim, Ms. Boouk Hur. In addition, I would like to express many thanks to the Aachen-Korean-Church and to VEKNI (Association of Korean Scientists and Engineer Association in the FRG). I could forget homesickness but not forget Korean with you!

I thank my “Mitfahrer/in”, Mr. Chanwoo Park, Mr. Robert Weng and Ms. Sacha van Albada, for being my friend and spreading ‘Happy virus!’ on the way to research center and back home.

Furthermore, I would like to take this opportunity to express my thanks to my boyfriend Sungjune Park for wonderful time with him and the best support to strengthen me. It was really great lucky that I could meet you in Aachen!

The most important in my life, I would like to convey my appreciation and love to my Moon’s family for their endless love and warm encouragement. Thank you so much for giving your patience and waiting for me!

I heartily appreciate once again!

1. **Einsatz von multispektralen Satellitenbilddaten in der Wasserhaushalts- und Stoffstrommodellierung – dargestellt am Beispiel des Rureinzugsgebietes**
von C. Montzka (2008), XX, 238 Seiten
ISBN: 978-3-89336-508-1
2. **Ozone Production in the Atmosphere Simulation Chamber SAPHIR**
by C. A. Richter (2008), XIV, 147 pages
ISBN: 978-3-89336-513-5
3. **Entwicklung neuer Schutz- und Kontaktierungsschichten für Hochtemperatur-Brennstoffzellen**
von T. Kiefer (2008), 138 Seiten
ISBN: 978-3-89336-514-2
4. **Optimierung der Reflektivität keramischer Wärmedämmschichten aus Yttrium-teilstabilisiertem Zirkoniumdioxid für den Einsatz auf metallischen Komponenten in Gasturbinen**
von A. Stuke (2008), X, 201 Seiten
ISBN: 978-3-89336-515-9
5. **Lichtstreuende Oberflächen, Schichten und Schichtsysteme zur Verbesserung der Lichteinkopplung in Silizium-Dünnschichtsolarzellen**
von M. Berginski (2008), XV, 171 Seiten
ISBN: 978-3-89336-516-6
6. **Politikszzenarien für den Klimaschutz IV – Szenarien bis 2030**
hrsg. von P. Markewitz, F. Chr. Matthes (2008), 376 Seiten
ISBN 978-3-89336-518-0
7. **Untersuchungen zum Verschmutzungsverhalten rheinischer Braunkohlen in Kohledampferzeugern**
von A. Schlüter (2008), 164 Seiten
ISBN 978-3-89336-524-1
8. **Inorganic Microporous Membranes for Gas Separation in Fossil Fuel Power Plants**
by G. van der Donk (2008), VI, 120 pages
ISBN: 978-3-89336-525-8
9. **Sinterung von Zirkoniumdioxid-Elektrolyten im Mehrlagenverbund der oxidkeramischen Brennstoffzelle (SOFC)**
von R. Mücke (2008), VI, 165 Seiten
ISBN: 978-3-89336-529-6
10. **Safety Considerations on Liquid Hydrogen**
by K. Verfondern (2008), VIII, 167 pages
ISBN: 978-3-89336-530-2

11. **Kerosinreformierung für Luftfahrtanwendungen**
von R. C. Samsun (2008), VII, 218 Seiten
ISBN: 978-3-89336-531-9
12. **Der 4. Deutsche Wasserstoff Congress 2008 – Tagungsband**
hrsg. von D. Stolten, B. Emonts, Th. Grube (2008), 269 Seiten
ISBN: 978-3-89336-533-3
13. **Organic matter in Late Devonian sediments as an indicator for environmental changes**
by M. Klopisch (2008), XII, 188 pages
ISBN: 978-3-89336-534-0
14. **Entschwefelung von Mitteldestillaten für die Anwendung in mobilen Brennstoffzellen-Systemen**
von J. Latz (2008), XII, 215 Seiten
ISBN: 978-3-89336-535-7
15. **RED-IMPACT**
Impact of Partitioning, Transmutation and Waste Reduction Technologies on the Final Nuclear Waste Disposal
SYNTHESIS REPORT
ed. by W. von Lensa, R. Nabbi, M. Rossbach (2008), 178 pages
ISBN 978-3-89336-538-8
16. **Ferritic Steel Interconnectors and their Interactions with Ni Base Anodes in Solid Oxide Fuel Cells (SOFC)**
by J. H. Froitzheim (2008), 169 pages
ISBN: 978-3-89336-540-1
17. **Integrated Modelling of Nutrients in Selected River Basins of Turkey**
Results of a bilateral German-Turkish Research Project
project coord. M. Karpuzcu, F. Wendland (2008), XVI, 183 pages
ISBN: 978-3-89336-541-8
18. **Isotopengeochemische Studien zur klimatischen Ausprägung der Jünger Dryas in terrestrischen Archiven Eurasiens**
von J. Parplies (2008), XI, 155 Seiten, Anh.
ISBN: 978-3-89336-542-5
19. **Untersuchungen zur Klimavariabilität auf dem Tibetischen Plateau - Ein Beitrag auf der Basis stabiler Kohlenstoff- und Sauerstoffisotope in Jahrringen von Bäumen waldgrenznaher Standorte**
von J. Griessinger (2008), XIII, 172 Seiten
ISBN: 978-3-89336-544-9

20. **Neutron-Irradiation + Helium Hardening & Embrittlement Modeling of 9%Cr-Steels in an Engineering Perspective (HELENA)**
by R. Chaouadi (2008), VIII, 139 pages
ISBN: 978-3-89336-545-6
21. **in Bearbeitung**
22. **Verbundvorhaben APAWAGS (AOEV und Wassergenerierung) – Teilprojekt: Brennstoffreformierung – Schlussbericht**
von R. Peters, R. C. Samsun, J. Pasel, Z. Porš, D. Stolten (2008), VI, 106 Seiten
ISBN: 978-3-89336-547-0
23. **FREEVAL**
Evaluation of a Fire Radiative Power Product derived from Meteosat 8/9 and Identification of Operational User Needs
Final Report
project coord. M. Schultz, M. Wooster (2008), 139 pages
ISBN: 978-3-89336-549-4
24. **Untersuchungen zum Alkaliverhalten unter Oxycoal-Bedingungen**
von C. Weber (2008), VII, 143, XII Seiten
ISBN: 978-3-89336-551-7
25. **Grundlegende Untersuchungen zur Freisetzung von Spurstoffen, Heißgaschemie, Korrosionsbeständigkeit keramischer Werkstoffe und Alkalirückhaltung in der Druckkohlenstaubfeuerung**
von M. Müller (2008), 207 Seiten
ISBN: 978-3-89336-552-4
26. **Analytik von ozoninduzierten phenolischen Sekundärmetaboliten in *Nicotiana tabacum* L. cv Bel W3 mittels LC-MS**
von I. Koch (2008), III, V, 153 Seiten
ISBN 978-3-89336-553-1
27. **IEF-3 Report 2009. Grundlagenforschung für die Anwendung**
(2009), ca. 230 Seiten
ISBN: 978-3-89336-554-8
28. **Influence of Composition and Processing in the Oxidation Behavior of MCrAlY-Coatings for TBC Applications**
by J. Toscano (2009), 168 pages
ISBN: 978-3-89336-556-2
29. **Modellgestützte Analyse signifikanter Phosphorbelastungen in hessischen Oberflächengewässern aus diffusen und punktuellen Quellen**
von B. Tetzlaff (2009), 149 Seiten
ISBN: 978-3-89336-557-9

30. **Nickelreaktivlot / Oxidkeramik – Fügungen als elektrisch isolierende Dichtungskonzepte für Hochtemperatur-Brennstoffzellen-Stacks**
von S. Zügner (2009), 136 Seiten
ISBN: 978-3-89336-558-6
31. **Langzeitbeobachtung der Dosisbelastung der Bevölkerung in radioaktiv kontaminierten Gebieten Weißrusslands – Korma-Studie**
von H. Dederichs, J. Pillath, B. Heuel-Fabianek, P. Hill, R. Lennartz (2009),
Getr. Pag.
ISBN: 978-3-89336-532-3
32. **Herstellung von Hochtemperatur-Brennstoffzellen über physikalische Gasphasenabscheidung**
von N. Jordán Escalona (2009), 148 Seiten
ISBN: 978-3-89336-532-3
33. **Real-time Digital Control of Plasma Position and Shape on the TEXTOR Tokamak**
by M. Mitri (2009), IV, 128 pages
ISBN: 978-3-89336-567-8
34. **Freisetzung und Einbindung von Alkalimetallverbindungen in kohlebefeuchten Kombikraftwerken**
von M. Müller (2009), 155 Seiten
ISBN: 978-3-89336-568-5
35. **Kosten von Brennstoffzellensystemen auf Massenbasis in Abhängigkeit von der Absatzmenge**
von J. Werhahn (2009), 242 Seiten
ISBN: 978-3-89336-569-2
36. **Einfluss von Reoxidationszyklen auf die Betriebsfestigkeit von anodengestützten Festoxid-Brennstoffzellen**
von M. Ettler (2009), 138 Seiten
ISBN: 978-3-89336-570-8
37. **Großflächige Plasmaabscheidung von mikrokristallinem Silizium für mikromorphe Dünnschichtsolarmodule**
von T. Kilper (2009), XVII, 154 Seiten
ISBN: 978-3-89336-572-2
38. **Generalized detailed balance theory of solar cells**
by T. Kirchartz (2009), IV, 198 pages
ISBN: 978-3-89336-573-9
39. **The Influence of the Dynamic Ergodic Divertor on the Radial Electric Field at the Tokamak TEXTOR**
von J. W. Coenen (2009), xii, 122, XXVI pages
ISBN: 978-3-89336-574-6

40. **Sicherheitstechnik im Wandel Nuklearer Systeme**
von K. Nünighoff (2009), viii, 215 Seiten
ISBN: 978-3-89336-578-4
41. **Pulvermetallurgie hochporöser NiTi-Legierungen für Implantat- und Dämpfungsanwendungen**
von M. Köhl (2009), XVII, 199 Seiten
ISBN: 978-3-89336-580-7
42. **Einfluss der Bondcoatzusammensetzung und Herstellungsparameter auf die Lebensdauer von Wärmedämmschichten bei zyklischer Temperaturbelastung**
von M. Subanovic (2009), 188, VI Seiten
ISBN: 978-3-89336-582-1
43. **Oxygen Permeation and Thermo-Chemical Stability of Oxygen Permeation Membrane Materials for the Oxyfuel Process**
by A. J. Ellett (2009), 176 pages
ISBN: 978-3-89336-581-4
44. **Korrosion von polykristallinem Aluminiumoxid (PCA) durch Metalljodidschmelzen sowie deren Benetzungseigenschaften**
von S. C. Fischer (2009), 148 Seiten
ISBN: 978-3-89336-584-5
45. **IEF-3 Report 2009. Basic Research for Applications**
(2009), 217 Seiten
ISBN: 978-3-89336-585-2
46. **Verbundvorhaben ELBASYS (Elektrische Basissysteme in einem CFK-Rumpf) - Teilprojekt: Brennstoffzellenabgase zur Tankinertisierung - Schlussbericht**
von R. Peters, J. Latz, J. Pasel, R. C. Samsun, D. Stolten
(2009), xi, 202 Seiten
ISBN: 978-3-89336-587-6
47. **Aging of ¹⁴C-labeled Atrazine Residues in Soil: Location, Characterization and Biological Accessibility**
by N. D. Jablonowski (2009), IX, 104 pages
ISBN: 978-3-89336-588-3
48. **Entwicklung eines energetischen Sanierungsmodells für den europäischen Wohngebäudesektor unter dem Aspekt der Erstellung von Szenarien für Energie- und CO₂ - Einsparpotenziale bis 2030**
von P. Hansen (2009), XXII, 281 Seiten
ISBN: 978-3-89336-590-6

49. **Reduktion der Chromfreisetzung aus metallischen Interkonnektoren für Hochtemperaturbrennstoffzellen durch Schutzschichtsysteme**
von R. Trebbels (2009), iii, 135 Seiten
ISBN: 978-3-89336-591-3
50. **Bruchmechanische Untersuchung von Metall / Keramik-Verbundsystemen für die Anwendung in der Hochtemperaturbrennstoffzelle**
von B. Kuhn (2009), 118 Seiten
ISBN: 978-3-89336-592-0
51. **Wasserstoff-Emissionen und ihre Auswirkungen auf den arktischen Ozonverlust**
Risikoanalyse einer globalen Wasserstoffwirtschaft
von T. Feck (2009), 180 Seiten
ISBN: 978-3-89336-593-7
52. **Development of a new Online Method for Compound Specific Measurements of Organic Aerosols**
by T. Hohaus (2009), 156 pages
ISBN: 978-3-89336-596-8
53. **Entwicklung einer FPGA basierten Ansteuerungselektronik für Justageeinheiten im Michelson Interferometer**
von H. Nöldgen (2009), 121 Seiten
ISBN: 978-3-89336-599-9
54. **Observation – and model – based study of the extratropical UT/LS**
by A. Kunz (2010), xii, 120, xii pages
ISBN: 978-3-89336-603-3
55. **Herstellung polykristalliner Szintillatoren für die Positronen-Emissions-Tomographie (PET)**
von S. K. Karim (2010), VIII, 154 Seiten
ISBN: 978-3-89336-610-1
56. **Kombination eines Gebäudekondensators mit H₂-Rekombinatorelementen in Leichtwasserreaktoren**
von S. Kelm (2010), vii, 119 Seiten
ISBN: 978-3-89336-611-8
57. **Plant Leaf Motion Estimation Using A 5D Affine Optical Flow Model**
by T. Schuchert (2010), X, 143 pages
ISBN: 978-3-89336-613-2
58. **Tracer-tracer relations as a tool for research on polar ozone loss**
by R. Müller (2010), 116 pages
ISBN: 978-3-89336-614-9

59. **Sorption of polycyclic aromatic hydrocarbon (PAH) to Yangtze River sediments and their components**
by J. Zhang (2010), X, 109 pages
ISBN: 978-3-89336-616-3
60. **Weltweite Innovationen bei der Entwicklung von CCS-Technologien und Möglichkeiten der Nutzung und des Recyclings von CO₂**
Studie im Auftrag des BMWi
von W. Kuckshinrichs et al. (2010), X, 139 Seiten
ISBN: 978-3-89336-617-0
61. **Herstellung und Charakterisierung von sauerstoffionenleitenden Dünnschichtmembranstrukturen**
von M. Betz (2010), XII, 112 Seiten
ISBN: 978-3-89336-618-7
62. **Politiksznarien für den Klimaschutz V – auf dem Weg zum Strukturwandel, Treibhausgas-Emissionsszenarien bis zum Jahr 2030**
hrsg. von P. Hansen, F. Chr. Matthes (2010), 276 Seiten
ISBN: 978-3-89336-619-4
63. **Charakterisierung Biogener Sekundärer Organischer Aerosole mit Statistischen Methoden**
von C. Spindler (2010), iv, 163 Seiten
ISBN: 978-3-89336-622-4
64. **Stabile Algorithmen für die Magnetotomographie an Brennstoffzellen**
von M. Wannert (2010), ix, 119 Seiten
ISBN: 978-3-89336-623-1
65. **Sauerstofftransport und Degradationsverhalten von Hochtemperaturmembranen für CO₂-freie Kraftwerke**
von D. Schlehüser (2010), VII, 139 Seiten
ISBN: 978-3-89336-630-9
66. **Entwicklung und Herstellung von foliengegossenen, anodengestützten Festoxidbrennstoffzellen**
von W. Schafbauer (2010), VI, 164 Seiten
ISBN: 978-3-89336-631-6
67. **Disposal strategy of proton irradiated mercury from high power spallation sources**
by S. Chiriki (2010), xiv, 124 pages
ISBN: 978-3-89336-632-3
68. **Oxides with polyatomic anions considered as new electrolyte materials for solid oxide fuel cells (SOFCs)**
by O. H. Bin Hassan (2010), vii, 121 pages
ISBN: 978-3-89336-633-0

69. **Von der Komponente zum Stack: Entwicklung und Auslegung von HT-PEFC-Stacks der 5 kW-Klasse**
von A. Bendzulla (2010), IX, 203 Seiten
ISBN: 978-3-89336-634-7
70. **Satellitengestützte Schwerewellenmessungen in der Atmosphäre und Perspektiven einer zukünftigen ESA Mission (PREMIER)**
von S. Höfer (2010), 81 Seiten
ISBN: 978-3-89336-637-8
71. **Untersuchungen der Verhältnisse stabiler Kohlenstoffisotope in atmosphärisch relevanten VOC in Simulations- und Feldexperimenten**
von H. Spahn (2010), IV, 210 Seiten
ISBN: 978-3-89336-638-5
72. **Entwicklung und Charakterisierung eines metallischen Substrats für nanostrukturierte keramische Gastrennmembranen**
von K. Brands (2010), vii, 137 Seiten
ISBN: 978-3-89336-640-8
73. **Hybridisierung und Regelung eines mobilen Direktmethanol-Brennstoffzellen-Systems**
von J. Chr. Wilhelm (2010), 220 Seiten
ISBN: 978-3-89336-642-2
74. **Charakterisierung perowskitischer Hochtemperaturmembranen zur Sauerstoffbereitstellung für fossil gefeuerte Kraftwerksprozesse**
von S.A. Möbius (2010) III, 208 Seiten
ISBN: 978-3-89336-643-9
75. **Characterization of natural porous media by NMR and MRI techniques: High and low magnetic field studies for estimation of hydraulic properties**
by L.-R. Stingaciu (2010), 96 pages
ISBN: 978-3-89336-645-3
76. **Hydrological Characterization of a Forest Soil Using Electrical Resistivity Tomography**
by Chr. Oberdörster (2010), XXI, 151 pages
ISBN: 978-3-89336-647-7
77. **Ableitung von atomarem Sauerstoff und Wasserstoff aus Satellitendaten und deren Abhängigkeit vom solaren Zyklus**
von C. Lehmann (2010), 127 Seiten
ISBN: 978-3-89336-649-1

78. **18th World Hydrogen Energy Conference 2010 – WHEC2010**
Proceedings
Speeches and Plenary Talks
ed. by D. Stolten, B. Emonts (2012)
ISBN: 978-3-89336-658-3
- 78-1. **18th World Hydrogen Energy Conference 2010 – WHEC2010**
Proceedings
Parallel Sessions Book 1:
Fuel Cell Basics / Fuel Infrastructures
ed. by D. Stolten, T. Grube (2010), ca. 460 pages
ISBN: 978-3-89336-651-4
- 78-2. **18th World Hydrogen Energy Conference 2010 – WHEC2010**
Proceedings
Parallel Sessions Book 2:
Hydrogen Production Technologies – Part 1
ed. by D. Stolten, T. Grube (2010), ca. 400 pages
ISBN: 978-3-89336-652-1
- 78-3. **18th World Hydrogen Energy Conference 2010 – WHEC2010**
Proceedings
Parallel Sessions Book 3:
Hydrogen Production Technologies – Part 2
ed. by D. Stolten, T. Grube (2010), ca. 640 pages
ISBN: 978-3-89336-653-8
- 78-4. **18th World Hydrogen Energy Conference 2010 – WHEC2010**
Proceedings
Parallel Sessions Book 4:
Storage Systems / Policy Perspectives, Initiatives and Cooperations
ed. by D. Stolten, T. Grube (2010), ca. 500 pages
ISBN: 978-3-89336-654-5
- 78-5. **18th World Hydrogen Energy Conference 2010 – WHEC2010**
Proceedings
Parallel Sessions Book 5:
Strategic Analysis / Safety Issues / Existing and Emerging Markets
ed. by D. Stolten, T. Grube (2010), ca. 530 pages
ISBN: 978-3-89336-655-2
- 78-6. **18th World Hydrogen Energy Conference 2010 – WHEC2010**
Proceedings
Parallel Sessions Book 6:
Stationary Applications / Transportation Applications
ed. by D. Stolten, T. Grube (2010), ca. 330 pages
ISBN: 978-3-89336-656-9

78 Set (complete book series)

**18th World Hydrogen Energy Conference 2010 – WHEC2010
Proceedings**

ed. by D. Stolten, T. Grube, B. Emonts (2010)

ISBN: 978-3-89336-657-6

79. Ultrafast voltex core dynamics investigated by finite-element micromagnetic simulations

by S. Gliga (2010), vi, 144 pages

ISBN: 978-3-89336-660-6

80. Herstellung und Charakterisierung von keramik- und metallgestützten Membranschichten für die CO₂-Abtrennung in fossilen Kraftwerken

von F. Hauler (2010), XVIII, 178 Seiten

ISBN: 978-3-89336-662-0

81. Experiments and numerical studies on transport of sulfadiazine in soil columns

by M. Unold (2010), xvi, 115 pages

ISBN: 978-3-89336-663-7

82. Prompt-Gamma-Neutronen-Aktivierungs-Analyse zur zerstörungsfreien Charakterisierung radioaktiver Abfälle

von J.P.H. Kettler (2010), iv, 205 Seiten

ISBN: 978-3-89336-665-1

83. Transportparameter dünner geträgerter Kathodenschichten der oxidkeramischen Brennstoffzelle

von C. Wedershoven (2010), vi, 137 Seiten

ISBN: 978-3-89336-666-8

84. Charakterisierung der Quellverteilung von Feinstaub und Stickoxiden in ländlichem und städtischem Gebiet

von S. Urban (2010), vi, 211 Seiten

ISBN: 978-3-89336-669-9

85. Optics of Nanostructured Thin-Film Silicon Solar Cells

by C. Haase (2010), 150 pages

ISBN: 978-3-89336-671-2

86. Entwicklung einer Isolationsschicht für einen Leichtbau-SOFC-Stack

von R. Berhane (2010), X, 162 Seiten

ISBN: 978-3-89336-672-9

87. Hydrogen recycling and transport in the helical divertor of TEXTOR

by M. Clever (2010), x, 172 pages

ISBN: 978-3-89336-673-6

88. **Räumlich differenzierte Quantifizierung der N- und P-Einträge in Grundwasser und Oberflächengewässer in Nordrhein-Westfalen unter besonderer Berücksichtigung diffuser landwirtschaftlicher Quellen**
von F. Wendland et. al. (2010), xii, 216 Seiten
ISBN: 978-3-89336-674-3
89. **Oxidationskinetik innovativer Kohlenstoffmaterialien hinsichtlich schwerer Luftfeinbruchstörfälle in HTR's und Graphitentsorgung oder Aufarbeitung**
von B. Schlögl (2010), ix, 117 Seiten
ISBN: 978-3-89336-676-7
90. **Chemische Heißgasreinigung bei Biomassenvergasungsprozessen**
von M. Stemmler (2010), xv, 196 Seiten
ISBN: 978-3-89336-678-1
91. **Untersuchung und Optimierung der Serienverschaltung von Silizium-Dünnschicht-Solarmodulen**
von S. Haas (2010), ii, 202 Seiten
ISBN: 978-3-89336-680-4
92. **Non-invasive monitoring of water and solute fluxes in a cropped soil**
by S. Garré (2010), xxiv, 133 pages
ISBN: 978-3-89336-681-1
93. **Improved hydrogen sorption kinetics in wet ball milled Mg hydrides**
by L. Meng (2011), II, 119 pages
ISBN: 978-3-89336-687-3
94. **Materials for Advanced Power Engineering 2010**
ed. by J. Lecomte-Beckers, Q. Contrepolis, T. Beck and B. Kuhn
(2010), 1327 pages
ISBN: 978-3-89336-685-9
95. **2D cross-hole MMR – Survey design and sensitivity analysis for cross-hole applications of the magnetometric resistivity**
by D. Fielitz (2011), xvi, 123 pages
ISBN: 978-3-89336-689-7
96. **Untersuchungen zur Oberflächenspannung von Kohleschlacken unter Vergasungsbedingungen**
von T. Melchior (2011), xvii, 270 Seiten
ISBN: 978-3-89336-690-3
97. **Secondary Organic Aerosols: Chemical Aging, Hygroscopicity, and Cloud Droplet Activation**
by A. Buchholz (2011), xiv, 134 pages
ISBN: 978-3-89336-691-0

98. **Chrom-bezogene Degradation von Festoxid-Brennstoffzellen**
von A. Neumann (2011), xvi, 218 Seiten
ISBN: 978-3-89336-692-7
99. **Amorphous and microcrystalline silicon applied in very thin tandem solar cells**
by S. Schicho (2011), XII, 190 pages
ISBN: 978-3-89336-693-4
100. **Sol-gel and nano-suspension electrolyte layers for high performance solid oxide fuel cells**
by F. Han (2011), iv, 131 pages
ISBN: 978-3-89336-694-1
101. **Impact of different vertical transport representations on simulating processes in the tropical tropopause layer (TTL)**
by F. Plöger (2011), vi, 104 pages
ISBN: 978-3-89336-695-8
102. **Untersuchung optischer Nanostrukturen für die Photovoltaik mit Nahfeldmikroskopie**
von T. Beckers (2011), xiii, 128 Seiten
ISBN: 978-3-89336-696-5
103. **Impact of contamination on hydrogenated amorphous silicon thin films & solar cells**
by J. Wördenweber (2011), XIV, 138 pages
ISBN: 978-3-89336-697-2
104. **Water and Organic Nitrate Detection in an AMS: Laboratory Characterization and Application to Ambient Measurements**
by A. Mensah (2011), XI, 111 pages
ISBN: 978-3-89336-698-9
105. **Entwicklung eines neuen Konzepts zur Steuerung der thermischen Ausdehnung von glaskeramischen Verbundwerkstoffen mit angepasster Fließfähigkeit am Beispiel der Hochtemperatur-Brennstoffzelle**
von E. Wanko (2011), xi, 134 Seiten
ISBN: 978-3-89336-705-4
106. **Tomographic reconstruction of atmospheric volumes from infrared limb-imager measurements**
by J. Ungermann (2011), xiv, 153 pages
ISBN: 978-3-89336-708-5
107. **Synthese und Identifizierung von substituierten Mg-Al-Cl Doppelhydroxidverbindungen mit Schwerpunkt IR-Spektroskopie**
von B. Hansen (2011), XII, 121 Seiten
ISBN: 978-3-89336-709-2

108. **Analysis of spatial soil moisture dynamics using wireless sensor networks**
by U. Rosenbaum (2011), xxii, 120 pages
ISBN: 978-3-89336-710-8
109. **Optimierung von APS-ZrO₂-Wärmedämmschichten durch Variation der Kriechfestigkeit und der Grenzflächenrauigkeit**
von M. E. Schweda (2011), 168 Seiten
ISBN: 978-3-89336-711-5
110. **Sorption of a branched nonylphenol isomer and perfluorooctanoic acid on geosorbents and carbon nanotubes**
by C. Li (2011), X, 102 pages
ISBN: 978-3-89336-716-0
111. **Electron Transport in the Plasma Edge with Rotating Resonant Magnetic Perturbations at the TEXTOR Tokamak**
by H. Stoschus (2011), iv, 113 pages
ISBN: 978-3-89336-718-4
112. **Diffusion and Flow Investigations in Natural Porous Media by Nuclear Magnetic Resonance**
by N. Spindler (2011), viii, 144 pages
ISBN: 978-3-89336-719-1
113. **Entwicklung und Erprobung des Hygrometer for Atmospheric Investigations**
von T. Klostermann (2011), IV, 118 Seiten
ISBN: 978-3-89336-723-8
114. **Application of functional gene arrays for monitoring influences of plant/seasons on bacterial functions and community structures in constructed wetlands (Bitterfeld, Germany)**
by J. Ning (2011), xiv, 157 pages
ISBN: 978-3-89336-724-5
115. **Wasseraustrag aus den Kathodenkanälen von Direkt-Methanol-Brennstoffzellen**
von A. Schröder (2011), VII, 228 Seiten
ISBN: 978-3-89336-727-6
116. **CITYZEN Climate Impact Studies**
ed. by M. Schultz (2011), 45 pages
ISBN: 978-3-89336-729-0
117. **Software Tools zum interoperablen Austausch und zur Visualisierung von Geodatenätzen über das Internet**
von M. Schultz, M. Decker, S. Lührs (2011), iv, 156 Seiten
ISBN: 978-3-89336-730-6

118. **Optimierung eines Leichtbaudesigns für ein SOFC-Brennstoffzellenstack**
von T. Nguyen-Xuan (2011), III, 154 Seiten
ISBN: 978-3-89336-732-0
119. **Institute of Energy and Climate Research IEK-6:
Nuclear Waste Management & Reactor Safety Report 2009/2010
Material Science for Nuclear Waste Management**
ed. by M. Klinkenberg, S. Neumeier, D. Bosbach (2011), 242 pages
ISBN: 978-3-89336-735-1
120. **Fate of the Antibiotic Sulfadiazine in Yangtze River Sediments: Transformation, Sorption and Transport**
by N. Meng (2011), XII, 111 pages
ISBN: 978-3-89336-736-8
121. **Thermodynamische Eigenschaften gasförmiger und kondensierter Verbindungen für Hochtemperaturanwendungen**
von T. Markus (2011), II, 131 Seiten
ISBN: 978-3-89336-728-3
122. **Ein neues LIF-Instrument für flugzeug- und bodengebundene Messungen von OH- und HO₂-Radikalen in der Troposphäre**
von S. Broch (2011), IV, 160 Seiten
ISBN: 978-3-89336-742-9
123. **Processes in the Yangtze River System - Experiences and Perspectives**
Workshop-Proceedings
ed. by S. Küpper, G. Subklew, R.-D. Wilken (2011), 83 pages
ISBN: 978-3-89336-744-3
124. **Thermo-Mechanical Properties of Mixed Ion-Electron Conducting Membrane Materials**
by B. Huang (2011), 130 pages
ISBN: 978-3-89336-746-7
125. **Growth, Etching, and Stability of Sputtered ZnO:Al for Thin-Film Silicon Solar Cells**
by J. I. Owen (2011), xv, 192 pages
ISBN: 978-3-89336-749-8
126. **Entwicklung geträgerter Ba_{0,5}Sr_{0,5}Co_{0,8}Fe_{0,2}O_{3-δ} Sauerstoff-Permeationsmembranen**
von F. Schulze-Küppers (2011), ii, 119 Seiten
ISBN: 978-3-89336-752-8
127. **Development of the 2-Component-Injection Moulding for Metal Powders**
by A. P. Cysne Barbosa (2011), XIV, 150 pages
ISBN: 978-3-89336-753-5

128. **Performance of Tungsten-Based Materials and Components under ITER and DEMO Relevant Steady-State Thermal Loads**
by G. H. Ritz (2011), X, 128 pages
ISBN: 978-3-89336-755-9
129. **Experimentelle Bestimmung und numerische Simulation von Viskositäten in Schlackesystemen unter Vergasungsbedingungen**
von T. Nentwig (2011), 156 Seiten
ISBN: 978-3-89336-756-6
130. **Development of Thin Film Oxygen Transport Membranes on Metallic Supports**
by Y. Xing (2012), iv, 117 pages
ISBN: 978-3-89336-765-8
131. **Release of Inorganic Trace Elements from High-Temperature Gasification of Coal**
by M. Bläsing (2012), XVIII, 145 pages
ISBN: 978-3-89336-772-6
132. **Rauchgasseitige Korrosion von Nickelbasislegierungen für zukünftige 700°C-Dampfkraftwerke**
von F. Lüttschwager (2012), 145 Seiten
ISBN: 978-3-89336-773-3
133. **In-Situ Raman Spectroscopy: A Method to Study and Control the Growth of Microcrystalline Silicon for Thin-Film Solar Cells**
by S. Muthmann (2012), x, 134 pages
ISBN: 978-3-89336-774-0
134. **Remote sensing of sun-induced fluorescence for improved modeling of gross primary productivity in a heterogeneous agricultural area**
by A. Schickling (2012), xvi, 135 pages
ISBN: 978-3-89336-775-7
135. **Untersuchung der Ladungsträgerkonzentration und -beweglichkeit in mikrokristallinen Siliziumlegierungen mit Hall-Effekt und Thermokraft**
von C. Sellmer (2012), 159 Seiten
ISBN: 978-3-89336-778-8
136. **Development of thin film inorganic membranes for oxygen separation**
by H. J. Moon (2012), XII, 118 pages
ISBN: 978-3-89336-781-8

Energie & Umwelt / Energy & Environment
Band / Volume 136
ISBN 978-3-89336-781-8

